

Optical properties and reaction kinetics
of shock-heated gas-phase tracers
for quantitative laser-induced fluorescence

Von der Fakultät für Ingenieurwissenschaften, Abteilung Maschinenbau und Verfahrenstechnik

der

Universität Duisburg-Essen

zur Erlangung des akademischen Grades

eines

Doktors der Ingenieurwissenschaften

Dr.-Ing.

genehmigte Dissertation

von

Siavash Zabeti Jahromi

aus

Teheran

Gutachter: Prof. Dr. Christof Schulz
Prof. Dr. Sebastian Kaiser

Tag der mündlichen Prüfung: 24. Mai 2019

DuEPublico

Duisburg-Essen Publications online

UNIVERSITÄT
DUISBURG
ESSEN

Offen im Denken

ub | universitäts
bibliothek

Diese Dissertation wird über DuEPublico, dem Dokumenten- und Publikationsserver der Universität Duisburg-Essen, zur Verfügung gestellt und liegt auch als Print-Version vor.

DOI: 10.17185/duepublico/70308

URN: urn:nbn:de:hbz:464-20190807-075847-8

Alle Rechte vorbehalten.

*Von allen Menschen, die ich je gekannt,
Ich nur zwei Menschen glücklich fand.
Den, der der Welt Geheimnis tief erforscht,
Und den, der nicht ein Wort davon verstand.
Omar Khayyâm (1048 – 1131 AD)*

Table of Contents

1. Introduction and Motivation.....	1
2. Theoretical Background	5
2.1. Basic concepts of photophysics of organic molecules	5
2.1.1. Light absorption (Beer-Lambert law).....	5
2.1.2. Electronic states and transitions in polyatomic molecules.....	6
2.1.3. Monomolecular deactivation processes – Jablonski diagram	9
2.1.4. Laser-induced fluorescence (LIF)	11
2.1.5. Effects of temperature on absorption and emission spectra.....	13
2.2. Shock-tube theory.....	16
2.3. Reaction kinetic in the gas phase.....	20
2.3.1. Temperature dependence of reaction rates: Arrhenius equation	21
3. Tracer-based laser-induced fluorescence	23
3.1. Single-ring aromatics tracers	25
3.2. Acetylene	30
3.3. Bath gas selection	32
4. Experiment	33
4.1. Shock-tube facility.....	33
4.1.1. Multi-window test section	34
4.2. Excitation source and detection systems	35
4.2.1. Nd:YAG laser.....	35
4.2.2. Spectrometer.....	36
4.2.3. ICCD camera.....	37
4.2.4. EMCCD camera	38
4.3. Experimental procedure.....	40
4.3.1. Time-resolved absorption measurements.....	40
4.3.2. LIF measurements	42
4.3.3. Mass spectrometry.....	43
5. Results and Discussion: Characterization of Selected Tracers	48
5.1. Toluene	48
5.1.1. Absorption measurements	48
5.1.2. LIF measurements	54
5.1.3. Conclusions	58
5.2. Anisole.....	60
5.2.1. Absorption measurements	60

5.2.2.	HRR-TOF-MS measurements	62
5.2.3.	LIF measurements	66
5.2.4.	Conclusions	68
5.3.	p-xylene and 1,2,4-trimethylbenzene	70
5.3.1.	Absorption measurements	70
5.3.2.	LIF measurements	77
5.3.3.	Conclusions	79
5.4.	Acetylene	80
5.4.1.	Absorption measurements	80
5.4.2.	LIF measurements	83
5.4.3.	Conclusions	85
6.	A novel methodology for reaction-time-resolved LIF (RTR-LIF) measurements in shock tubes	86
6.1.	Motivation: Collecting more LIF data from each single shock-tube experiment.....	86
6.2.	New design to realize RTR-LIF	87
6.3.	Problems to be solved: Laser and signal attenuation.....	92
6.4.	Results of RTR-LIF	95
6.5.	Conclusions	97
7.	Outlook.....	98
8.	Conclusions	99
9.	List of own publications	102
10.	References	103

Abstract

Reliable and quantitative application of tracer-based laser-induced fluorescence (LIF) for imaging measurements of fuel concentration, equivalence ratio, and temperature in combustion processes requires knowledge about photophysical properties and thermal stability of the respective tracers at high temperature. In this work, ultraviolet absorption and LIF emission spectra of toluene, anisole, p-xylene (p-XL), 1,2,4-trimethylbenzene (1,2,4-TMB), and acetylene were studied at high temperatures and different reaction times behind reflected shock waves. Relative fluorescence quantum yields of these tracers were determined to extend existing data to higher temperatures. After the onset of pyrolysis of these tracers, effective absorption cross-sections and the corresponding absorption and LIF spectra are reported. Pyrolysis products were found to be the major contributors to the absorption and LIF signals at higher temperatures. The temporal behavior of the absorption at 266 nm during the pyrolysis of tracers was compared to simulations based on literature kinetics models and available high-temperature absorption cross-sections. To aid the interpretation of absorption and LIF experiments of anisole at high temperatures, the products of anisole pyrolysis were investigated using a shock tube coupled to a high-repetition-rate time-of-flight mass spectrometer (HRR-TOF-MS) for time-resolved multispecies measurements. Concentration-time profiles for anisole and products such as benzene, C_2H_4 , and CO were measured and compared to simulations using two kinetics models from literature.

Moreover, a novel experimental concept is presented that allows reaction-time-resolved LIF (RTR-LIF) measurements with one single laser pulse using a new shock-tube test section that has several optical ports. After the passage of the shock wave, the reactive mixture is excited along the center of the tube with a 266-nm laser beam directed through a window in the end-wall of the shock tube. The emitted LIF signal is collected through elongated sidewall windows and focused onto the entrance slit of an imaging spectrometer coupled to an intensified charge-coupled device (ICCD) camera. The one-dimensional spatial resolution of the measurement translates into a reaction-time-resolved measurement according to the characteristics of the shock wave, while species information can be gained from the spectral axis of the detected two-dimensional image.

Kurzfassung

Die zuverlässige und quantitative Anwendung der Tracer-basierten laserinduzierten Fluoreszenz (LIF) für abbildgebende Messungen von Kraftstoffkonzentration, Äquivalenzverhältnis und Temperatur in Verbrennungsprozessen erfordert Kenntnisse über photophysikalische Eigenschaften und thermische Stabilität von Tracern bei hohen Temperaturen. In der vorliegenden Arbeit wurden Ultraviolettabsorption und LIF-Emissionsspektren von Toluol, Anisol, p-Xylol (p-XL), 1,2,4-Trimethylbenzol (1,2,4-TMB) und Ethin bei hohen Temperaturen und unterschiedlichen Reaktionszeiten hinter reflektierten Stoßwellen untersucht. Relative Fluoreszenzquantenausbeuten dieser Tracer wurden bestimmt und dadurch der Temperaturbereich bisheriger Daten deutlich erweitert. Untersucht wurden auch die effektiven Absorptionsquerschnitte und die LIF-Emissionssignale nach Beginn der Pyrolyse. Pyrolyseprodukte erwiesen sich als die Hauptbeitragenden zu den Absorptions- und LIF-Signalen unter Bedingungen der Pyrolyse. Das gemessene zeitliche Verhalten der Absorption bei 266 nm während der Pyrolyse der Tracer wurde mit Simulationen auf Basis von Kinetik-Modellen aus der Literatur und verfügbaren Hochtemperaturabsorptionsquerschnitten der Reaktionsprodukte verglichen. Um die Interpretation der Absorptions- und LIF-Experimente von Anisol bei hohen Temperaturen zu unterstützen, wurde die Zerfallsprozesse von Anisol unter pyrolytischen Bedingungen durch zeitaufgelöste Multispeziesmessungen mithilfe eines hochrepetitiven Flugzeitmassenspektrometers (HRR-TOF-MS) gekoppelt an das Stoßwellenrohr untersucht. Die Konzentrations-Zeit-Profile von Anisol und den Reaktionsprodukten Benzol, C_2H_4 und CO wurden gemessen und ebenfalls mit Simulationen auf Basis von Kinetik-Modellen aus der Literatur verglichen.

Darüber hinaus wird ein neuartiges experimentelles Konzept vorgestellt, das reaktionszeitaufgelöste LIF (RTR-LIF)-Messungen mit einem einzigen Laserpuls unter Verwendung einer neuen Messstrecke, die mit mehreren optischen Zugängen ausgestattet ist, ermöglicht. Bei diesem Konzept wird nach der reflektierten Stoßwelle das reaktive Gasgemisch in Längsrichtung des Stoßwellenrohres durch ein Fenster in der Endplatte mit einem 266 nm Laserstrahl angeregt. Das emittierte LIF-Signal wird durch neukonzipierte längliche Seitenwandfenster beobachtet und auf den Eingangspalt eines abbildenden Spektrometers abgebildet. Die eindimensionale räumliche Auflösung der Messung führt zu einer reaktionszeitaufgelösten Messung, während die Speziesinformationen aus der Spektralachse der detektierten zweidimensionalen Bilder gewonnen werden kann.

Symbols and abbreviations

Symbols

A	Absorbance
A	Pre-exponential factor
A_{21}	Rate constant of spontaneous emission
B_{12}	Einstein coefficient for stimulated absorption
B_{21}	Einstein coefficient for stimulated emission
b_{12}	Rate constants of stimulated absorption
b_{21}	Rate constants of stimulated emission
c	Concentration
c	Speed of light
c_p	Heat capacity at constant pressure
e	Electronic charge
E	Energy
E_a	Activation energy
E_K	Kinetic energy
E_P	Potential energy
F	Fractional absorption
h	Enthalpy
h	Planck constant
I_0	Incident light intensity
I	Transmitted light intensity
I_{laser}	Laser irradiance
k	Reaction rate coefficient
l	Length
m	Mass
M	Mach number
M	Molar mass
n	Number density
N	Number of particles
p	Pressure
Q	Quality factor
Q_{21}	Quenching rate constant
Q_{pre}	Predissociation rate constant
Q_{ion}	Photo-ionization rate constants

r	Reaction rate
R	Universal gas constant
S_0	Ground singlet state
S_1	First excited singlet state
t	Time
T	Transmittance
T	Temperature
u	Velocity
v	Velocity
v_{cs}	Contact surface velocity
v_i	Incident shock wave velocity
V	Detection volume
z	Number of electron charges
X_i	Chemical species

Greek symbols

α	Absorption coefficient
γ	Heat capacity ratio
λ	Wavelength
ν	Frequency of photon
ν	Stoichiometric coefficient
ρ	Density
ϕ	Fluorescence quantum yield
σ	Absorption cross-section
Ω	Detection angle
η	Detection efficiency

Abbreviations and acronyms

ARAS	Atomic resonance absorption spectroscopy
A/D	Analog to Digital
BBO	Beta-barium borate
CCD	Charge-coupled device
CIC	Clock-induced charge
EI	Electron ionization

EMCCD	Electron-multiplying charge-coupled device
HRR	High repetition rate
HOMO	Highest occupied molecular orbital
IC	Internal combustion
IC	Internal conversion
ICAS	Intracavity absorption spectroscopy
ISC	Intersystem crossing
ICCD	Intensified charge-coupled device
IRO	Intensified relay optics
LAS	Laser absorption spectroscopy
LIF	Laser-induced fluorescence
LIFF	Laser-induced fragmentation fluorescence
LII	Laser-induced incandescence
LUMO	Lowest unoccupied molecular orbital
MBS	Molecular-beam sampling
MCP	Microchannel plate
MS	Mass spectrometry
PAH	Polycyclic aromatic hydrocarbons
RTR-LIF	Reaction-time-resolved laser-induced fluorescence
SHG	Second harmonic generation
TDC	Top dead center
TMB	Trimethylbenzene
TOF	Time of flight
TR-LIF	Time-resolved laser-induced fluorescence
UV	Ultraviolet region of light
Vis	Visible region of light
VR	Vibrational relaxation
XL	Xylene

Acknowledgements

Like any other Ph.D. thesis, the one presented here would not have been possible without help, advice, and support of many other people: staff and colleagues at Institute for Combustion and Gas Dynamics (IVG) and also friends and family.

First and foremost I would like to express my deep gratitude to my supervisor Prof. Dr. Christof Schulz. I would like to thank for his mentorship and generous support throughout my time at IVG. I am also very grateful to him for the opportunity that he offered me to work in his world-class research group and laboratory. I am very fortunate to have received training under one of the pioneers in the field.

Special thanks to my group leader Dr. Mustapha Fikri for the tireless support, great guidance and useful comments that have contributed significantly in the works presented in this dissertation.

I would like to thank Dr. Oliver Welz and Dr. Stephan Faust for the help, discussions, and for sharing their immense knowledge about chemical kinetics and spectroscopy.

I would like to thank Prof. Thomas Dreier and Prof. Sebastian Kaiser for all the advice on photophysics, optics, lasers, and CCD cameras. I am also thankful to the management Dr. Ralf Starke for his valuable support throughout the work at IVG. My former and current office mates Dr. Mohammad Aghsaei and Dr. Damien Nativel: thank you very much for offering me a nice working environment. I deeply thank Barbara Nota and Barbara Graf for their help and assistance in overcoming all administrative obstacles. I gratefully acknowledge the invaluable technical support and assistance of Birgit Nelius, Ludger Jerig, and Dieter Hermanns in the shock-tube laboratory. I would like to thank all the current and former colleagues of the IVG not mentioned by name who overlapped with my graduate years in the group. It has been fun to work with you guys and I hope our paths will cross again soon.

I would like to thank my mother Ladan, father Ahmad and sister Mitra for all the support and dedication they have provided me my whole life and faith in me. You always care for me so much even though I have been away from you.

Last, but definitely not least, I would like to express my heartfelt gratitude to my loving wife and my best friend Anahita for her endless love, encouragement, support and assistance in all kind, cheerful sense of humor and care which has been always important part of my success. Without your encouragements I would not have made it so far.

1. Introduction and Motivation

In today's world, increasing problems caused by transportation and industrial growth have the potential to damage human life and nature. Combustion of fossil fuels is the largest atmospheric source of carbon dioxide (CO_2) and toxic gases and pollutants such as carbon monoxide (CO), sulfur dioxide (SO_2), nitrogen oxide (NO_x), and soot. All these species have significant destructive effects on the local, regional and global environment. The emission of these harmful gases in the air, not only causes air pollution but also combined with atmospheric precipitation creates acidic rain that causes water acidification of rivers, lakes and underground sources. According to the World Energy Outlook 2017 the world energy demand from today to 2040 will increase of about 30% in the New Policies Scenario [1]. In spite of fast growth of non-fossil fuel consumption, it is expected that fossil fuels still account for 78% of energy use in 2040 [2]. Among fossil fuels, petroleum-based liquid fuels remain the main source of the world energy consumption. Even though advances in non-fossil fuel transportation technologies are anticipated, we are still far from practical and economical solutions and the transportation sector accounts for 55% of the total increase in the use of liquid fuels [3]. In this sector, gasoline remains the most important transportation fuel (Fig. 1). Hence, reducing pollutant emissions together with increasing energy-conversion efficiency in internal combustion (IC) engines is one of the most promising and effective approaches to improving the energy, economy, and environmental management in the near future.

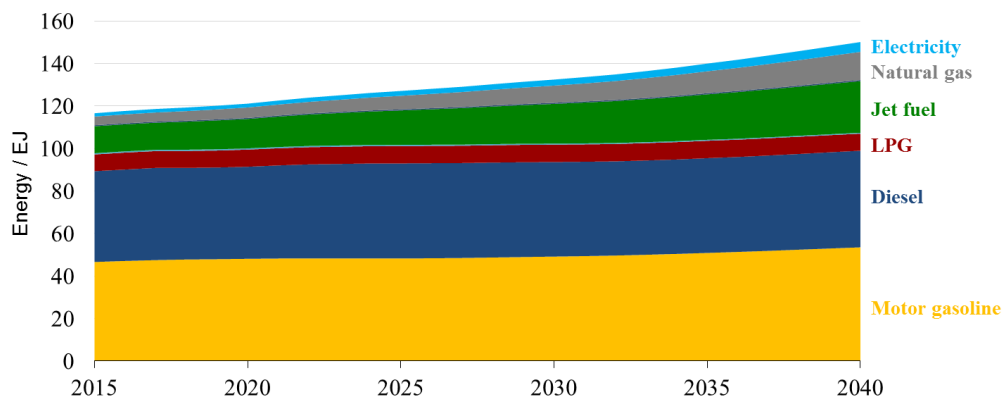


Fig. 1: World transportation energy consumption per year by energy source [3].

Lack of precise understanding of in-cylinder combustion processes and ability to accurately simulate them, as well as inadequate knowledge and capability to use fuel/oxidizer composition fully and effectively are some of main barriers to improve the efficiency and reduce the emission in IC engines. In other words, IC engine require in-depth understanding of the underlying combustion processes to control/optimize. It is therefore important to obtain quantitative information about the conditions of the unburned gas prior to and during ignition, i.e., fuel/air ratio, oxygen concentration, fuel concentration, and temperature, as well as the progress of fuel decomposition during the pre-ignition phase. Over the last two decades, fuel-imaging techniques based on laser-induced fluorescence (LIF) of different fuels and tracer

molecules have developed into a widely used diagnostics tool for the rapid detection of fast in-cylinder processes [4-7]. The study and analysis of processes using LIF in an engine enables the implementation of pollutant emissions reduction without sacrificing engine performance. It has been shown that LIF techniques not only allow for mixing studies but also for quantitative temperature and oxygen concentration measurements [5]. It provides high spatially- and time-resolved visualization and measurements of the fuel, intermediates of the combustion processes and also pollutants such as nitrogen oxide and soot precursors in internal combustion (IC) engines.

The accurate interpretation of the complex interactions of photo-physics and chemical kinetics, however, is a particular challenge for analyzing LIF signals. Commercial fuels such as Diesel and gasoline contain numerous organic species that upon UV laser excitation emit significant fluorescence signal. However, due to the unknown source of the LIF emissions a precise interpretation of the LIF signals from commercial fuels is very difficult. In order to characterize absorption and fluorescence signal of detecting in-cylinder processes, well-characterized fluorescent species (the so-called tracers) are typically added to a non-fluorescing surrogate fuel (e.g., iso-octane). Different type of fluorescent organic species, mostly ketones (e.g., acetone, 3-pentanone) and aromatics (e.g., toluene, naphthalene) have been the subject of extensive investigations [8-15].

It is well known that the LIF signal of organic tracer molecules depends on temperature, pressure, and bath gas composition. Effects of variations in those physical quantities on absorption cross-sections as well as fluorescence quantum yields have been frequently measured in heated static cells and flow cells [15-18]. The maximum temperature, that was accessible to investigations in static and flow cell experiments, however, is limited by the restricted lifetime of the tracers at high temperature. These experimental devices have typical residence times of seconds to minutes (at high temperature) which is much longer than the residence time of hot compressed gases in an IC engine prior to ignition. Furthermore, at temperatures above ~ 700 K, the degradation of the tracers is observed that is often attributed to the contact with hot metal surfaces. This temperature regime, which is of high importance for applications in IC engines, was therefore not investigated and quantitative interpretation of LIF signals often relies on extrapolation of the available data towards higher temperatures. Without detailed understanding of the chemical kinetics at high temperatures along with photo-physics, the implementation of tracer-based LIF techniques to optimize combustion processes in future IC engines is impossible.

Because organic tracers behave similar to the fuel compounds, they might be influenced by pre-ignition reactions just in a similar way as the fuel compounds (i.e., decomposes and is oxidized at the same rate as the fuel). In this case, close to autoignition, the tracer would disappear early in the cool-flame phase before the onset of heat release. At high temperature, unimolecular decomposition can happen in the gas phase [5, 10], and if this reaction proceeds more rapidly than the decomposition of the parent fuel, the tracer will not track the parent fuel

concentration reliably. Simulations have indicated that the decomposition and ignition behavior of fluorescence tracers can differ significantly from the behavior of the parent fuel [19, 20]; these effects strongly depend on the chemical structure of the tracer. Potential decomposition products may contribute either to absorption (leading to laser and signal attenuation) or even fluorescence (forming a potential source of interference or opening new diagnostics opportunities). Therefore, detailed investigations of the optical properties of tracers and their decomposition products during their thermal degradation are necessary for the quantitative interpretation of tracer-LIF measurements under IC engine conditions at high temperatures.

Experimental studies of tracer decomposition at high temperatures that would provide the required kinetics and spectroscopic data are sparse and have often been carried out in application-motivated environments without perfect control of the reaction conditions [21-23]. Because of the rapid gas-dynamic heating of gases within a few microseconds, shock tubes give access to measurements on shorter time scales and offer the opportunity to extend the investigated temperature range to higher temperatures in shock-heated gases (i.e., no contact to metal surfaces and very short residence times at high temperature) and on engine-relevant time scales. Therefore, the experiments in shock-heated gas mixtures are very important to close the gap in understanding high-temperature data obtained from tracer-LIF-signal intensities in a spectroscopic cell and an IC engine.

An additional concern is the potential interaction of tracers with the ignition chemistry of the parent fuel, which may affect the ignition and combustion properties of the parent fuel [24, 25]. Experiments in HCCI engines have shown that the 3-pentanone as tracer disappears several hundred microseconds before autoignition and additional species (here: formaldehyde) are formed during the ignition of the fuel/air mixture [23]. Longer-chain ketones, such as 5-nonanone, have shown significant changes in fluorescence spectra indicating tracer decomposition in a Diesel environment where, however, non-specified fluorescing decomposition products compensated for the loss of the original tracer [22]. Hence, determining the stability of the pure tracer in shock tubes enables the investigation of the decomposition kinetics of tracers and their interaction with the parent fuel in a homogeneous environment. The obtained spectra and the temporal variation of effective absorption cross-sections provide a valuable database for practical applications in high-temperature environments and can also serve as validation targets for chemical kinetics modeling of the different reaction steps during tracer decomposition. The overall goal of such measurements in shock tubes is to study the LIF and absorption spectroscopy of tracer in order to characterize the LIF-signal behavior for quantitative signal interpretation at high temperatures and determine thermal stability limits for each tracer. Within these limits negligible variation of tracer concentration is desirable to provide direct information about fuel/air mixing.

One drawback in conventional shock-tube experiment is the low repeatability because shock-tube experiments require considerable time in between the individual runs. While reaction-time-resolved species concentration and temperature measurements with fast absorption

methods are established, conventional LIF measurements with pulsed lasers provide data only at a *single reaction time*. Therefore, only a single data point at a fixed reaction time could be generated for each shock-tube run via signal detection through a window in the end flange. In this thesis, a new test section for the shock tube has been developed that helps to overcome this limitation. The laser beam is inserted through a window in the end flange and sent along the center of the shock tube. In this way, LIF measurements with the imaging spectrometer – placed orthogonally to the beam axis – provide the capability of investigating the reactive gas mixture at multiple delay times after the passage of the reflected shock wave with a single laser shot. The one-dimensional spatial resolution of the measurement translates into a reaction-time-resolved measurement while species information can be gained from the spectral axis of the detected two-dimensional image. With this modified test section, it is possible to investigate the fluorescence properties of the initial heated tracer as well as its decomposition products (and possible steps in between) within a single shock run as a function of time for a time interval of several hundreds of microseconds.

This thesis is divided into eight chapters. Chapter 2 provides the principles of absorption and LIF spectroscopy, shock tube, and reaction kinetics. Chapter 3 provides general information about tracer-based LIF and detailed background of tracers applied in this work. Chapter 4 introduces the shock-tube facility and the experimental setup that was used for absorption and LIF measurements as well as time-of-flight mass spectrometry (TOF-MS). Experimental results are presented in chapter 5. The selected tracers (toluene, anisole, p-xylene (p-XL), and 1,2,4-trimethylbenzene (1,2,4-TMB)) and acetylene were investigated in terms of their optical properties, i.e., absorption cross-sections, LIF intensities and spectra as well as their relative fluorescence quantum yield at moderate and high temperatures. Furthermore, time-resolved absorption spectra of tracers and their decomposition products were measured as a function of reaction time behind reflected shock waves. These measurements were interpreted based on simulations using kinetics models for tracer pyrolysis. To aid the interpretation of anisole experiments, the products of anisole pyrolysis were investigated using a shock tube coupled to a high-repetition-rate time-of flight mass spectrometer (HRR-TOF-MS) for time-resolved multispecies measurements. In chapter 6, a novel experimental concept is presented that allows reaction-time-resolved laser-induced fluorescence (RTR-LIF) measurements with one single laser pulse using a new test section that is equipped with several optical ports. Chapter 7 and 8 present outlook for future work and conclude the thesis.

2. Theoretical Background

This chapter provides an outline of the necessary knowledge to describe the research approach. The chapter will first be devoted to the fundamentals of absorption and LIF followed by an introduction to shock-tube theory and reaction kinetics in the gas phase.

2.1. Basic concepts of photophysics of organic molecules

In the case of LIF, energy is first absorbed by the participating molecule and then emitted again in the form of light often with different photon energy. Therefore, the emitted light has a different wavelength than the excitation light. The processes absorption, energy conversion in the molecule, and emission are discussed in more detail below.

2.1.1. Light absorption (Beer-Lambert law)

A fundamental aspect of fluorescence spectroscopy is the measurement of light absorption. If light propagates in a medium, there is always an interaction of light with the surrounding matter. In order to electromagnetic waves interact with molecules following conditions must be fulfilled. The energy of the absorbed photon ($h\nu$) must exactly correspond to the energy difference (ΔE) between ground- and excited states of the involved molecule (i.e., $\Delta E = h\nu$). The number of absorbed photons per unit time is proportional to the concentration of the molecules in the ground state and the photon flux as well as the strength of the interaction described by the absorption cross-section. The process of absorption from ground singlet state S_0 to the first excited singlet state S_1 in an organic molecule can be written as a reaction including energy of the absorbed photon and two energy states.



The probability that absorption takes place is also decisive. In other words, the value of the transition moment must not be zero (see Sec. 2.1.2). In molecules, depending on the size and structure, possible transitions are arranged between strongly forbidden and fully allowed depending on the probability of their occurrence. The transition probabilities are found out by the electronic structure of the initial and final states and can be calculated with quantum theory. It is possible to experimentally determine this from the absorption strength.

The total absorption of light in a sample is the absorbance A , which is defined by the proportion of the transmitted light intensity $I(\lambda)$ to the incident light intensity $I_0(\lambda)$.

$$A(\lambda) = -\log \frac{I(\lambda)}{I_0(\lambda)} = -\log T(\lambda), \quad (1)$$

where $T(\lambda)$ is the transmittance.

If the absorber(s) are homogeneously distributed in the medium, the differential loss of the radiation intensity by absorption is proportional to the absorption coefficient $\alpha(\lambda)$, the irradiated intensity I and to layer thickness dl .

$$dI = \alpha(\lambda)I dl \quad (2)$$

The absorption coefficient is proportional to the concentration of the absorber(s). With integration over the absorption length, one obtains the Beer-Lambert law that describes the relationship between absorption and concentration of an absorbing species.

$$I(\lambda) = I_0(\lambda)e^{-\sigma(\lambda,T)nl} \quad (3)$$

It is therefore possible to determine the absorption cross-section $\sigma(\lambda)$,

$$\sigma(\lambda, T) = -\frac{\ln(I(\lambda)/I_0(\lambda))}{nl}, \quad (4)$$

where n is the number density and l is the absorption length.

The absorption cross-section is material-specific and wavelength-dependent. In tracer LIF it can be related to the probability of excitation from the ground state to excited state of the molecule, at a given wavelength and a given photon flux. It is due to the population statistics in the ground state also temperature dependent. UV/Vis absorption spectrum is typically a plot of absorption intensity as a function of wavelength. For more information about absorption spectrum and absorption measurements refer to section 4.3.1.

2.1.2. Electronic states and transitions in polyatomic molecules

As described in the previous section, when a medium is exposed to UV/Vis light, a part of the incident light that matches possible electronic transitions will be absorbed. The spectrum of transmitted light shows certain frequencies that are attenuated. Generally, absorption spectra of atoms and small molecules show sharp lines. In larger molecules, the observed absorption is typically broadband. The reason of this is that molecules have a large number of vibrational and rotational energy levels that are associated with each electronic state of a molecule and very close together. Therefore, the population of the respective states is distributed over many possible energy levels and molecules can be generally promoted to the vibrational and rotational sub-levels of the excited electronic state. This distribution gives a combination of overlapping absorption lines due to the line broadening at ambient conditions, which results in a broadband spectrum.

Ordinary UV/Vis spectra of organic molecules are observed from 200–700 nm. The transferred energy to the molecules excites electrons from the occupied orbital of electronic ground state (lower energy) to an unoccupied orbital of excited state (higher energy). As mentioned before, the absorbed energy of the light is equal to the energy difference between the ground and excited states. Generally, the electrons move from highest occupied molecular orbital (HOMO) to the lowest unoccupied molecular orbital (LUMO). There are three types of orbitals in a molecule, i.e., σ , π , and n orbitals. A σ orbital can be made from two atomic orbitals, or one s and one p orbital, or two collinear p atomic orbitals. π orbitals have higher energy than σ orbitals. A π orbital is made from two lateral atomic p orbitals. Orbitals with lone pair electrons are non-bonding molecular orbitals n and have a higher energy level than π orbitals. Antibonding orbitals (σ^* , π^*) have the highest energy and are usually not occupied in the ground state. The stimulation of a σ electron needs a much higher energy than π electron that leads to the absorption in far UV and therefore will not be studied in this work. An appropriate energy of a photon can promote one of the π electrons to an antibonding orbital π^* . Excitation of a non-bonding electron to an antibonding orbital (σ^* , π^*) is also possible.

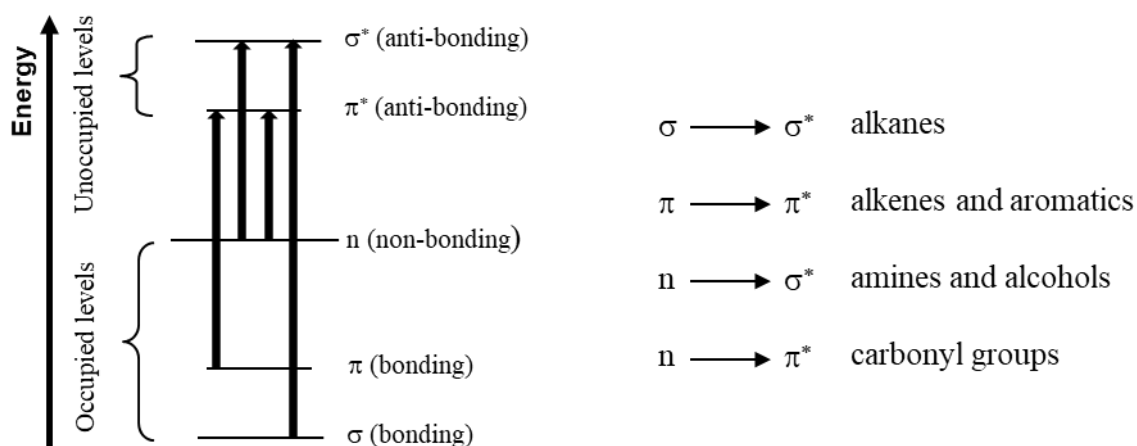


Fig. 2: Electronic states and possible electronic transitions that can occur in the molecular orbitals [26]. The transitions are illustrated by arrows.

Figure 2 shows the general order of electronic transitions and gives examples for those transitions. In alkanes and saturated hydrocarbons, which consist solely of single bonds (σ) and have no lone pair electrons the only possible transition is $\sigma \rightarrow \sigma^*$. The σ bonds are very strong and this transition requires very high energy and absorbs UV light in the vacuum ultraviolet region ($\lambda < 200$ nm). In saturated molecules such as ethers, alcohols, amines and sulfides with unshared electrons, the $n \rightarrow \sigma^*$ transition can occur. These transitions are fairly strong and have absorption band in 150–260 nm region. In unsaturated molecules such as alkenes, alkynes, aromatics, and carbonyl compounds the $\pi \rightarrow \pi^*$ transition can occur. Here, the π electron of the double or triple bond promotes to the π^* antibonding orbital ($\lambda > 200$ nm). Due to experimentally appropriate spectral range, the applications of absorption spectroscopy of organic molecules are typically based on the $\pi \rightarrow \pi^*$ and $n \rightarrow \sigma^*$ transitions. However, the central focus of

this work is on aromatic molecules with $\pi \rightarrow \pi^*$ transitions and non-bonding electrons which located on heteroatoms such as oxygen or nitrogen will not be considered here. One good example with all possible transitions is formaldehyde (Fig. 3).

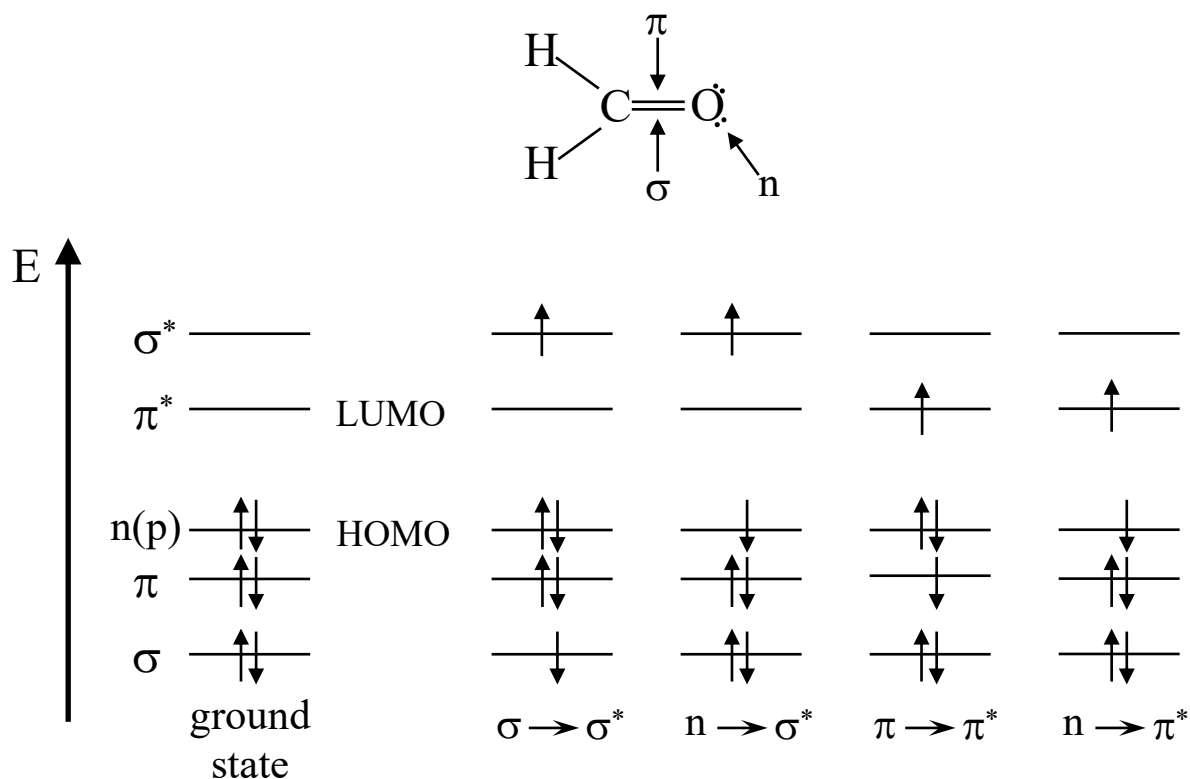


Fig. 3: Energy levels of molecular orbitals and possible electronic transitions in formaldehyde [27].

All transitions, however, are not always observed and some limitations for transitions exist that are provided by so-called selection rules. The numbers of electrons that can be promoted at one time, symmetry properties of the molecule and of the electronic states are some examples of the selection rules. Two major selection rules for absorption transitions are spin-forbidden and symmetry-forbidden transitions. The strictest prohibition of transition applies to spin-forbidden transition. This rule expresses that the spin quantum number of an electron cannot change during a transition. According to the Pauli exclusion principle, the electrons at the same energy level must have opposite spin $\uparrow\downarrow$ that is called a singlet state. If they have the same spin $\uparrow\uparrow$, they must occupy different energy levels. This is then called a triplet state. The spin selection rule says that during a transition the total spin cannot change. Therefore, singlet-singlet and triplet-triplet transitions are allowed, but singlet-triplet and triplet-singlet transitions are forbidden. In other words, in a transition from ground singlet state S_0 to the first higher excited singlet state S_1 , the spin does not change ($S = +1/2 - 1/2 = 0$). In a transition from singlet to a triplet state, the spin of the excited electron changes, so that $S = 0$ in the singlet state alters to $S = +1/2 + 1/2 = +1$ in the triplet state. Such a transition is generally forbidden. Another forbidden transition is the symmetry-forbidden transition. It states that transitions between states of the same parity (symmetry with respect to a center of inversion) are forbidden and the transitions that take place between orbitals of unequal parity are allowed.

This is the case for the S_0 – S_1 transition in aromatic molecules (studied in this thesis). However, as it is discussed in Ref. [28], these molecules absorb light, in contrast to the selection rules, because the Born-Oppenheimer approximation is partly violated. Molecular vibrations couple with the electron system and break the perfect symmetry by distorting the electron wave functions. This introduces non-zero contributions to the integral, i.e., the resulting transitions are “vibrationally allowed” [28]. Selection rules are based on approximations, therefore forbidden transitions are often observed, although at weak intensity. The $\sigma \rightarrow \pi^*$ and $\pi \rightarrow \sigma^*$ transitions are other examples of forbidden transitions that have very low transition probabilities. For detailed information about selection rules refer to Ref. [29].

2.1.3. Monomolecular deactivation processes – Jablonski diagram

After absorption of light from S_0 into the electronically higher excited singlet states S_n , the excited molecule is not in thermal equilibrium with its surroundings. The state has a short lifetime and is deactivated by various intramolecular and intermolecular processes (radiative or non-radiative). Decisive factors for determining the dominating deactivation processes are the chemical structure of the molecule, the nature of the excited state, temperature, pressure, and the nature of the colliding molecules. These complex energy transfer processes can be simplified and illustrated in the Jablonski diagram (Fig. 4). The electronic transitions that are illustrated with vertical lines in Fig. 4 are called vertical transitions. Photochemical processes in which the molecule is altered or destroyed such as photolysis are not considered here. Electronic transitions are accompanied by both rotational and vibrational transitions. For simplification, no rotational energy levels were plotted.

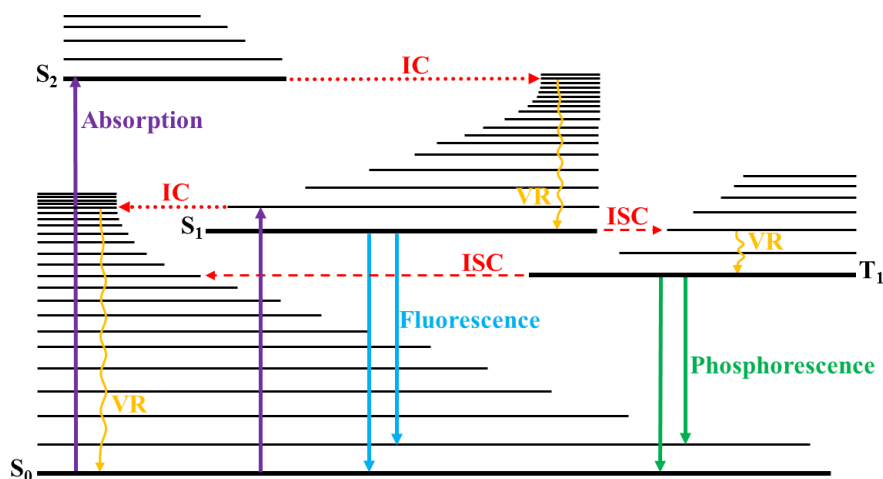


Fig. 4: Jablonski diagram showing energy conversion pathways for the photo-physical deactivation of electronically-excited organic molecules [5]. Radiationless processes are represented by dashed lines and radiation processes with solid lines. VR: vibrational relaxation, IC: internal conversion, ISC: intersystem crossing.

Due to collisions with bath gas molecules, the electronically-excited molecule loses its vibrational energy to the surroundings and relaxes quickly (within about 10^{-13} to 10^{-10} s) into states that are in thermal equilibrium with their ambient condition. This process is called vibrational relaxation (VR). Since vibrational relaxation occurs between vibrational levels of a same

state, electrons will not change from one electronic level to another. The energy is released in form of heat into the environment and the probability of states is determined by the Boltzmann distribution of each electronic state.

If vibrational energy levels of electronic states with same multiplicity overlap, population from vibration at levels in the higher electronic state can be transferred to another vibration level in a lower electronic state. For example, a transition from the S_1 state occurs to the same energy vibrational level of the ground state S_0 . This process is known as internal conversion (IC) and is typically completed on the same timescale as the vibrational relaxation. Another non-radiative process is intersystem crossing (ISC), which describes a transition with changing in the total spin quantum number, i.e., transfer of population between states of different multiplicity (e.g., $S_1 \rightarrow T_1$). According to Hund's rule for organic molecules, the first triplet state always lies energetically lower than the first corresponding singlet state. Therefore, crossing is energetically favorable, although the transition is forbidden by spin selection rules (cf. Sec. 2.1.2) and usually occurs rather slowly. The intersystem crossing rate constant is in many cases on the order of the fluorescence rate constant, but it can be strongly influenced by the bath gas (e.g., collision with O_2 , which is important in case of aromatics).

Fluorescence refers to the radiative transition between states with the same spin multiplicity. Fluorescence process occurs on the order of 10^{-9} to 10^{-7} s. Since the non-radiative relaxation occurs very quickly from higher excited singlet states S_n ($n > 1$) into the ground vibrational state of the lowest excited state of a given multiplicity, i.e., first excited singlet state, fluorescence typically take place from the vibrational ground state of the S_1 into a vibrational state of the S_0 (Kasha's rule). Although this rule is based on empirical observations and there are some exceptions where the emission occurs from a higher excited state, it is true at least for the majority of the organic molecules. It can be explained by the fact that the higher singlet states have a significantly smaller energy difference, resulting in very fast vibrational relaxation and internal conversion.

Absorption and fluorescence in organic molecules usually show a so-called mirror-image behavior. This is true for most organic molecules when referring to the S_1 to S_0 transition. The emission spectrum is therefore a mirror image of the absorption spectrum (S_0 to S_1 transition) and mirrored towards the red spectral range. However, the emission spectrum is weaker than absorption spectrum. In general, the energy difference, i.e., the energy of the emitted radiation (fluorescence) is at most equal to the absorbed energy. The maximum of the fluorescence intensity is thus red-shifted (Stokes shift) with respect to the excitation wavelength. The reason for this is that a partial radiationless deactivation, i.e., rotational and vibrational relaxation occurs before the emission of a fluorescence photon.

The radiative transition between states with different spin multiplicity is called phosphorescence. Since the ground state normally is a singlet state, the phosphorescence occurs from the first excited triplet state T_1 into a vibrational state of S_0 . As already mentioned above, a direct excitation of the first triplet state from the ground singlet state is spin forbidden transition;

therefore, an occupation can only occur by intersystem crossing from the S_1 state. Respectively, the transition from the first triplet state by phosphorescence is also spin-forbidden. For these two reasons, the first triplet state has a much longer lifetime than the first singlet state and phosphorescence occurs on the order of microseconds to seconds and longer.

2.1.4. Laser-induced fluorescence (LIF)

LIF is a spectroscopic measurement method that uses laser radiation to excite molecules for fluorescence. It is frequently used in combustion diagnostics, due to its high sensitivity and selectivity for detecting species in intended operating environment. The high selectivity of the LIF techniques can be obtained through the selective excitation of specific molecules using high power narrowband laser sources and treating the emitted fluorescent light with a high-performance detection technique (cf. Sec. 4.2). The spectrally narrow low-divergence laser beam allows a spatial resolution of few micrometers and the short pulse duration ensures a high temporal resolution. The time scales of the LIF are orders of magnitude smaller than the time scales for chemical reactions and transport processes and this allows to take snapshots even from highly turbulent reactive systems such as processes in combustion engines, in gas turbines, in heated flow channels, and in shock tubes. The application of LIF for studying non-reactive and reactive systems has been proven particularly for ultraviolet and visible excitation [5, 30]. The high sensitivity of the LIF technique (down to the sub-ppm values) also allows the detection and monitoring intermediate species which are only partially forming during pyrolysis and combustion. Thanks to the rapid development of image-intensified CCD cameras and the presence of high-power pulsed lasers, it is also possible to shape the laser beam into a laser light sheet and advance two-dimensional measurements, which ensure a high degree of spatial and temporal resolution [31, 32].

2.1.4.1. Signal intensity and FQY

The traditional approach to explain the theory of LIF concept is a two-level model. This model describes the basic processes involved in absorption and emission of a photon covers most of the important items of laser-induced fluorescence for the usually applied situation, i.e., the weak excitation. It considers a system from identical molecules (or atoms) with two different energy levels that represent the ground state (energetically lower level) and the excited state (energetically higher level) of the molecule. As mentioned before, if the energy of a photon corresponds to the difference energy between these two states, the photon energy will be absorbed and an electron is promoted from its ground state into the excited state. This process is called stimulated (or also induced) absorption. It is assumed that the system is in thermal equilibrium. The possible transitions between two levels and their corresponding rate coefficients are shown in Fig. 5.

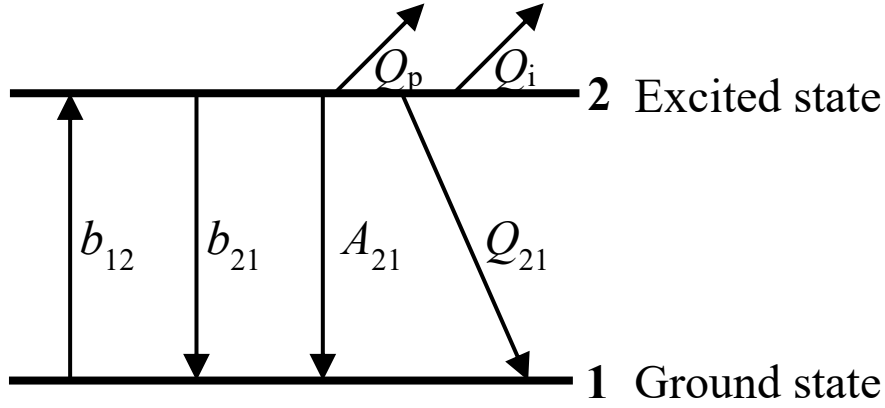


Fig. 5: Two-level model with stimulated absorption (b_{12}) and emission (b_{21}), spontaneous emission (A_{21}), quenching (Q_{21}), predissociation (Q_p), and photo-ionization (Q_i) [33].

The rate constant of the stimulated absorption is shown with b_{12} . b_{21} represents the rate constant of stimulated emission that induced by a photon interacting with the excited system. b_{12} and b_{21} are directly correlated with Einstein coefficients of the stimulated absorption B_{12} and emission B_{21} by incident laser irradiance I_{Laser} . A_{21} denotes the rate constant for the spontaneous emission of a photon, i.e., fluorescence that is also referred to as Einstein coefficient for spontaneous emission. Note that the phosphorescence process is not taken into account in the two-level model. Q_{21} is the quenching (de-excitation) rate constants for non-radiative deactivation processes of the excited state, i.e., ISC, IC or collisional quenching by ambient molecules. This is dependent on the nature and concentration of the surrounding species. Q_p and Q_i are the predissociation and photo-ionization rate constants. Q_p and Q_i are commonly negligible, which is the situation in most LIF experiments unless in specific chosen conditions. In contrast to the rate constants of the stimulated transitions, A_{21} is a species-specific constant.

Hence the intensity of the fluorescence depends on many factors that can be classified by their impact on absorption and emission (fluorescence quantum yield) efficiencies or on the efficiency of the fluorescence detection. A detailed derivation of the integrated signal intensity is given in Ref. [33] and it is not repeated here. The main relation to describe the detectable fluorescence intensity S_{fl} in the linear regime (low laser intensity) is shown in Eq. 5.

$$S_{\text{fl}} = I_{\text{laser}} \frac{h\nu}{c} B_{12} V N_0 \frac{A_{21}}{A_{21} + Q_{21}} \eta \Omega / 4\pi \quad (5)$$

For a quantitative evaluation of the fluorescence intensity, the laser irradiance I_{laser} must be known. The wavelength and temperature dependent absorption cross-section $\sigma(\lambda, T)$ can be mathematically defined by $\frac{h\nu B_{12}}{c\Delta\nu_1}$, where $h\nu$ denotes the energy of the absorbed photon. The term $\frac{A_{21}}{A_{21} + Q_{21}}$ in Eq. 5 represents the fluorescence quantum yield $\phi_{\text{fl}}(\lambda, T, p, p_{\text{O}_2})$ and indicates the fraction of the actual excited molecules that relax to the ground state by fluorescence emission. Generally, ϕ_{fl} is wavelength-, temperature-, and pressure-dependent and depends

also on the fluorescing molecule – due to intermolecular collision processes, i.e., quenching by the bath gas species (mostly O_2) – there might be also a substantial dependence on the bath gas composition. The value of ϕ_{fl} gives a measure of the strength of the fluorescence as it represents the ratio of emitted photons in the form of fluorescent light to the overall absorbed photons. Therefore, its value is unity at the maximum, if all absorbed photons lead to the emission of fluorescence. The fluorescence signal S_{fl} is also linked to the detection volume V and the number density of the investigated molecules N_0 . When all other factors are known, it gives the possibility to directly determine species concentration from the fluorescence signal S_{fl} . In this equation, there are also quantities which depend on the specific experimental arrangement, i.e., the fractional detection solid angle collected by the optics $\Omega/4\pi$ and factor for detection efficiency of the detection system η . The detection solid angle and the quantum efficiency of the recording system are determined by the experimental setup and the used imaging system. Also depending on the working distance and the used optics, there can be considerable differences in signal yield.

Hence, for weak laser excitation, the fluorescence signal intensity can be calculated from the following equation:

$$S_{fl} = I_{laser} V n \sigma(\lambda_{ex}, T) \phi_{fl}(\lambda_{ex}, T) \eta_{opt} \Omega / 4\pi \quad (6)$$

If the number density of the tracer is time-independent, the combined effects of σ and ϕ_{fl} determine the dependence of the LIF intensity on wavelength and temperature. As a consequence, knowledge of the value and the temperature dependence of the fluorescence quantum yield of tracer species is crucial for quantitative applications.

In general, pressure affects the fluorescence quantum yield; albeit in the presented LIF data in this work, the pressure was kept constant. The detection efficiency η and the fractional detection solid angle $\Omega/4\pi$ are constant throughout the measurements with the same setup. According to Eq. 6, the relative fluorescence quantum yield can be derived from the expression

$$\frac{\phi_{fl,T}}{\phi_{fl,ref}} = \frac{S_{fl,T}}{I_T n_T \sigma_T} \frac{I_{ref} n_{ref} \sigma_{ref}}{S_{fl,ref}} \quad (7)$$

where the index “ref” represents the quantities determined at reference conditions, typically the lowest temperature investigated (in this work: room temperature).

2.1.5. Effects of temperature on absorption and emission spectra

Absorption

Absorption spectra of many polyatomic organic molecules including aromatics exhibit a continuous bell-shaped form. Typically, an increase in temperature leads to a considerable shift (generally red-shift), broadening of the shape and blur of the vibrational fine structure of the

spectra. The latter is attributed to the population increase of the excited molecules, i.e., the formation of a so-called molecular ‘hot’ band [34].

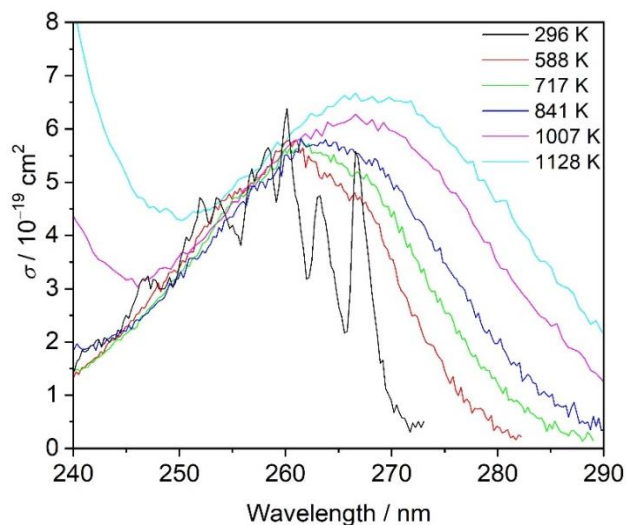


Fig. 6: Toluene absorption spectra at various temperatures [12].

In the simplest way the temperature dependence of the UV/Vis absorption features can be described by the Sulzer–Wieland formalism. Sulzer and Wieland [35] introduced several simplifications to derive simple equations determining the temperature dependence of absorption spectra. For instance, because there is no prior information available about the upper potential curve of state, they considered linear dependence and constant total absorption strength of each band at all temperatures. Using their formalism, Sulzer and Wieland represented the shape of the absorption spectra of Cl_2 , Br_2 , I_2 , and $(\text{C}_6\text{H}_5)_2$. Their formalism describes fairly well the form of the main part of the absorption spectrum; however, it does not take into account the weak but experimentally clearly observed shift of the maximum of the absorption curve [36]. Brouwer and Troe [36] showed that the temperature dependence of the spectrum is complicated and cannot be easily predicted based on simple models like the Sulzer-Wieland method combined with the room-temperature spectrum alone. In a similar approach, following the Sulzer-Wieland formalism, Astholz et al. [37] included the red shift of the spectral contributions from higher vibrational states $\nu > 0$. In order to do this, they assumed an average red-shift as given by the average vibrational energy. This modification gives an asymmetry and temperature-dependent shift of the spectra. Astholz et al. [37] measured UV absorption of substituted cycloheptatrienes, toluene, p-xylene, and of benzyl and methyl-benzyl radicals at temperatures between 700 and 1650 K in a shock tube. They reported that the difference between the measured spectra and the simplified numerical calculation increases with increasing the substituent size. Later, Hippler et al. [38] removed some simplifications (such as frequency of the spectral change-inducing oscillator) in the Sulzer-Wieland derivation and simulated the experimental results of the temperature dependence of the absorption spectra of toluene in a shock tube up to 1800 K.

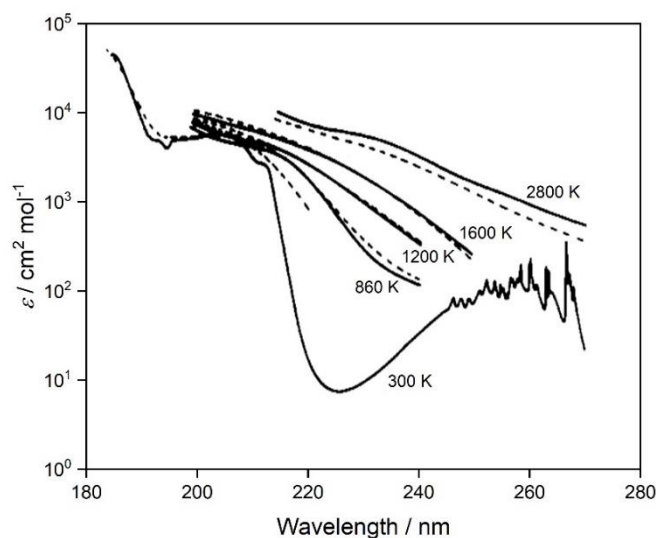


Fig. 7: Comparison of measured (solid lines) and simulated (dashed lines) absorption coefficients of toluene [38].

Fluorescence

In case of organic tracers, the fluorescence signal intensity per molecule at a fixed excitation (e.g., 266 nm) and pressure is strongly temperature dependent $S \sim \sigma(266 \text{ nm}, T) \phi(266 \text{ nm}, T)$. In recent years, dependences of fluorescence spectra of ketones and aromatics on temperature have been studied to some extent [5, 39, 40]. However, the temperature dependence of the fluorescence signal intensity and fluorescence quantum yield of many of those tracers is still less understood. Since aromatic tracers are frequently used for practical applications such as fuel concentration measurements in IC engines, there is an increasing need for further research to correct the temperature effects on their fluorescence signal.

The dependences of the fluorescence signal i.e., the FQY are more complex than for absorption. Generally (for the tracers and excitation wavelength considered in this work), the quantum yield decreases with increasing temperature. This is assigned to non-radiative relaxation processes such as intersystem crossing and internal conversion, being in competition with the fluorescence from the excited state (cf. Sec. 2.1.3). The magnitude of this reduction strongly depends on the tracer species [41]. Usually, a low temperature dependence of the FQY is desirable to gain strong LIF signal at high temperatures. However, strong temperature dependence can be favorable when the temperature is the quantity of interest [5]. Figure 8 shows the relative quantum yield of several tracers as a function of temperature in as a bath gas of nitrogen N_2 [39].

In addition to the variation in fluorescence quantum yields, a temperature-dependent shift in fluorescence spectra is typically observed. In the case of aromatic molecules, when the temperature increases, the fluorescence band shifts to the longer wavelength range is noticeable. For instance, Koban et al. [12] reported a red shift of 2 nm of spectrum peak per 100 K for toluene. It was attributed to the vibrational level-dependent internal energy flow and relaxa-

tion processes after photo-excitation [41]. This shift was exploited to develop a temperature measurement method [5].

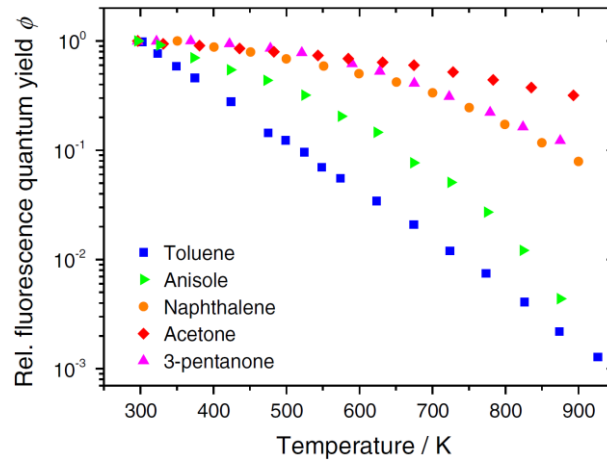


Fig. 8: Temperature dependence of the fluorescence quantum yield of some tracers in 1 bar N_2 at 266 nm normalized to the value at the lowest investigated temperature [39].

Benzler et al. [42] introduced a new semi-empirical model similar to the one of Koban et al. [12] and Faust et al. [11] for predicting relative LIF signal intensities of toluene, o-XL and 1,2,4-TMB considering specific terms for each species. The model was validated against experimental absorption cross-sections and effective fluorescence lifetimes obtained from previous studies in high-temperature optical cells of Koban et al. [12], Rossow [40] and Faust et al. [16] at 300–1000 K up to 10 bar in pure N_2 and at 1 bar for environments between pure N_2 and air composition.

2.2. Shock-tube theory

The shock tube in the basic form that was used for the first time by Vieille at 1899 [43] is still applied for investigations of gases at high temperatures. The main applications of shock tubes are studies of chemical reactions, dissociation, ionization, relaxation, and impact processes as well as spectroscopic investigations in gases. Shock tubes provide a way to observe substances in the gas phase in a wide range of pressure and temperature. It is easily possible to generate the intended conditions, e.g., high temperatures and pressures behind shock waves to study those using various diagnostics methods, which is not accessible with other methods or only with difficulty. These conditions generally occur very rapidly (within less than 1 μ s) after the passage of the (reflected) shock wave and can be retained for up to several milliseconds. This requires measurements with high time resolution in shock tubes to monitor changes in the high-temperature gas environment, e.g., due to chemical reactions. One important property of the shock-tube methods is that the experimental condition is achieved homogeneously across the cross-section of the tube without the influence of the wall of the apparatus.

A shock tube is usually a long straight tube with constant cross-section that is divided into a low- and a high-pressure section by a diaphragm. The low-pressure section contains the test

substance or mixture (usually diluted in a bath gas like argon or nitrogen) and the other section contains a suitable driver gas at high pressure. Generally, a low-molecular-weight gas such as helium or hydrogen is introduced into the high-pressure section until the diaphragm bursts. After the burst of the diaphragm, the gas expansion turns into a shock wave that propagates into the low-pressure section. The shock wave spreads through the test gas with supersonic velocity ($M > 1$) regarding to the sound velocity of the test gas before the experiment and subsonic velocity ($M < 1$) regarding to the heated gas behind the shock front. The compression in the shock front results in a temperature increase, however, without heat exchange with the wall due to the limited time. At the end of the low-pressure section, the shock wave hits the end plate of shock tube and is reflected. Consequently, the gas experiences a second sudden increase in pressure and temperature. The propagation velocity decreases in comparison to the incident wave. The temporal arrangement of these processes and the corresponding conditions and zones are illustrated in the $x-t$ diagram (Fig. 9). The qualitative pressure and temperature profiles are also shown in this figure. The shock wave is formed immediately after the burst of the diaphragm and directed toward the end plate with a constant velocity v_i and is reflected there. Furthermore, the contact surface, which separates the driven and driver gas, also moves toward the end plate with a lower velocity $v_{cs} < v_i$. In addition, a rarefaction wave is generated that moves towards end plate of the driver section. It thus forms an expansion fan. The rarefaction wave hits the end plate of the driver section and travels back into the driven section. Typically, the occurring temperature and pressure states (T, p) are determined by different zones:

Zone 1: Initial state of the test gas, i.e., test gas in front of incident shock wave

Zone 2: Test gas behind incident shock wave between the shock front and contact surface

Zone 3: Driver gas between the contact surface and the end of the expansion fan

Zone 4: Initial state of the driver gas

Zone 5: Test gas behind the reflected shock wave

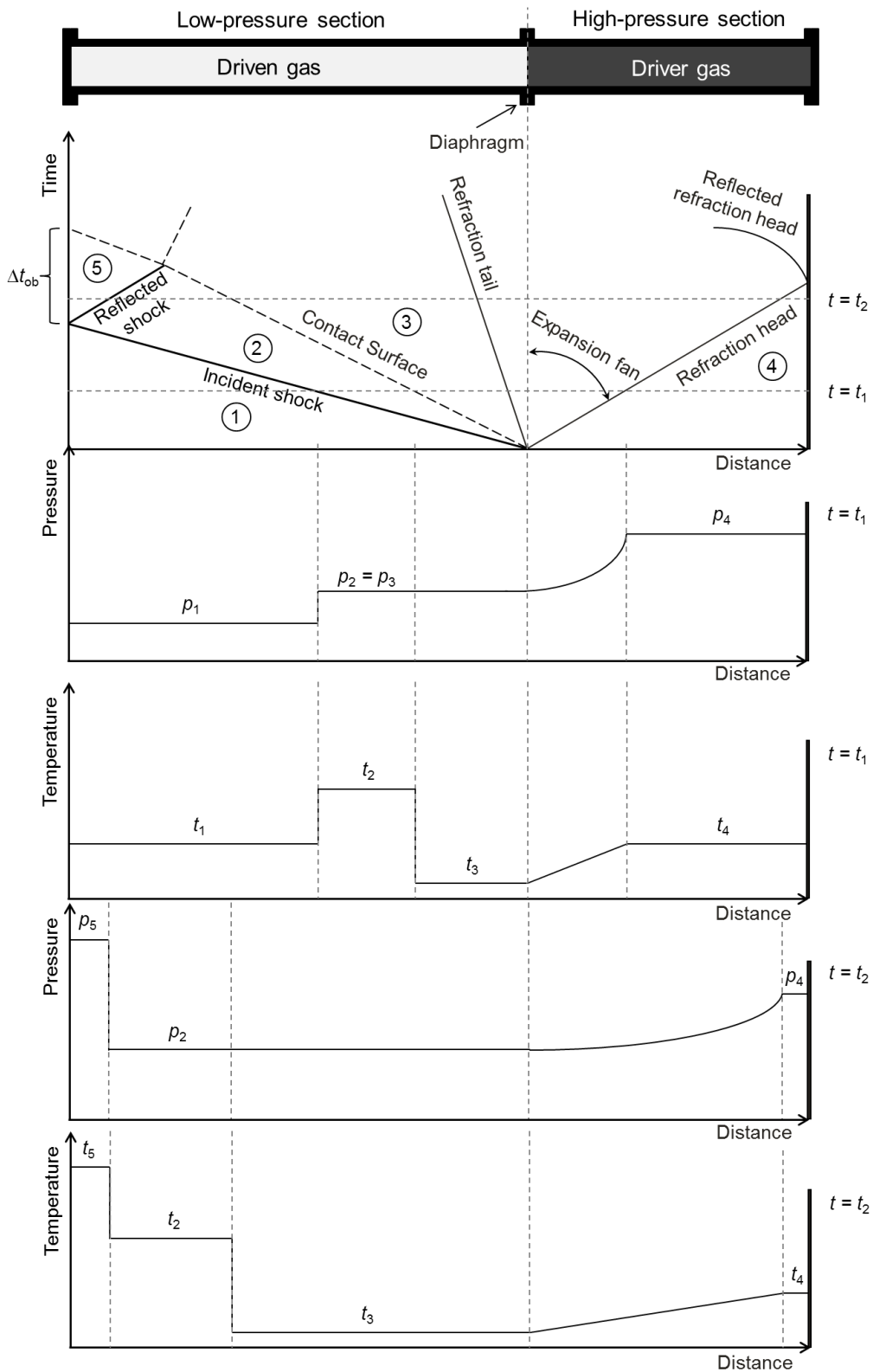


Fig. 9: Schematics of the propagation of incident and reflected waves, contact surface, and rarefaction wave along with the pressure and temperature distribution in the shock tube as a function of location and time [44].

The description of the state of the gas behind the incident shock wave is given by the conservation laws for mass, momentum, and energy using density ρ , velocity u (relative to the shock front), pressure p , and the specific enthalpy h .

$$\rho_1 u_1 = \rho_2 u_2 \quad (8)$$

$$p_1 + \rho_1 u_1^2 = p_2 + \rho_2 u_2^2 \quad (9)$$

$$h_1 + \frac{1}{2} u_1^2 = h_2 + \frac{1}{2} u_2^2 \quad (10)$$

Index 1 denotes the state of the gas in front of the incident shock wave and the index 2 denotes the state of the gas behind the incident wave.

For an ideal gas with constant heat capacity ratio (γ), Eqs. 8–10 can be transformed into the Rankine-Hugoniot equations using the thermal $pV = nRT$ and the caloric $h_2 - h_1 = c_p(T_2 - T_1) = \frac{\gamma}{\gamma-1}R(T_2 - T_1)$ equations.

$$\frac{p_2}{p_1} = \frac{1 - \left(\frac{\gamma-1}{\gamma+1}\right) \frac{\rho_1}{\rho_2}}{\frac{\rho_1}{\rho_2} - \frac{\gamma-1}{\gamma+1}} \quad (11)$$

$$\frac{\rho_2}{\rho_1} = \frac{\frac{\gamma-1}{\gamma+1} + \frac{p_2}{p_1}}{\left(\frac{\gamma-1}{\gamma+1}\right) \frac{p_2}{p_1} + 1} = \frac{u_1}{u_2} \quad (12)$$

$$\frac{T_2}{T_1} = \frac{p_2 \rho_1}{p_1 \rho_2} \quad (13)$$

By introducing the Mach number $M_1 = \frac{u_1}{\sqrt{\gamma M T_1}}$ (here, M is the molar mass of the test gas) one

obtains:

$$\frac{p_2}{p_1} = \frac{2\gamma M_1^2 - (\gamma - 1)}{\gamma + 1} \quad (14)$$

$$\frac{\rho_2}{\rho_1} = \frac{(\gamma + 1)M_1^2}{(\gamma - 1)M_1^2 + 2} \quad (15)$$

$$\frac{T_2}{T_1} = \frac{\left(\gamma M_1^2 - \frac{\gamma-1}{2}\right) \left(\frac{\gamma-1}{2} M_1^2 + 1\right)}{\left(\frac{\gamma+1}{2}\right)^2 M_1^2} \quad (16)$$

Therefore, the state variables of the gas can be determined using a known velocity of the shock wave. When the incident shock wave reaches the endwall, it is reflected back into the

gas, which is already heated by the incident wave. It leads to a further increase in temperature, pressure, and density. Due to the stagnant condition (zero velocity) behind the reflected shock wave, the gas releases all its kinetic energy and experiences an increase in the state variables greater than behind the incident wave. The state variables behind the reflected shock wave determined with following equations:

$$\frac{p_5}{p_1} = \left[\frac{\left(\frac{3\gamma-1}{\gamma-1}\right) M_1^2 - 2}{M_1^2 + \frac{2}{\gamma-1}} \right] \left[\frac{\left(\frac{2\gamma}{\gamma-1}\right) M_1^2 - 1}{\left(\frac{\gamma+1}{\gamma-1}\right)} \right] \quad (17)$$

$$\frac{\rho_5}{\rho_1} = \left[\frac{M_1^2 \left(\frac{\gamma+1}{\gamma-1}\right)}{M_1^2 + \frac{2}{\gamma-1}} \right] \left[\frac{\left(\frac{2\gamma}{\gamma-1}\right) M_1^2 - 1}{2M_1^2 + \frac{3-\gamma}{\gamma-1}} \right] \quad (18)$$

$$\frac{T_5}{T_1} = \frac{p_5 \rho_1}{p_1 \rho_5} \quad (19)$$

The reflected wave provides a convenient way to achieve high gas temperatures within short times. In addition, as mentioned the test-gas molecules are at rest behind the reflected shock waves. This offers a good possibility to investigate a precisely defined gas volume spectroscopically. The temperature range can be varied by the initial experimental conditions. Typical temperatures in low-pressure shock-tube experiments are between 500 and 2500 K. A disadvantage of the shock tube method is the single-shot nature of the facility associated with short time limitation (a few milliseconds) with stable conditions behind the shock waves. This time limitation imposes the use of very sensitive and high time-resolved detection technique. It is crucial to collect extensive information from each single experiment using appropriate measurement strategies (e.g., laser absorption spectroscopy (LAS) [45, 46]) that allow for time-resolved detection after the arrival of the shock wave. In section 6, a novel method for reaction-time-resolved LIF (RTR-LIF) in shock tubes is introduced.

2.3. Reaction kinetic in the gas phase

Chemical reaction kinetics look into the temporal behavior of chemical conversion processes. In particular, it is of interest at which rate and in which way chemical reactions take place, for example in combustion. A single reaction step that cannot be further subdivided is called an elementary reaction. The consecutive elementary reaction steps contribute to the overall reaction. In the homogeneous gas-phase reactions, an elementary reaction with N different species X_i can be represented as:



Depending on the sum of the stoichiometric coefficients $\nu_{i,j}$, i.e., the number of involved species, an elementary reaction is denoted as unimolecular, bimolecular or trimolecular reaction. The change in the concentration of the species (caused by j elementary reactions) can be expressed by the reaction rate r_j :

$$\frac{d[X_i]}{dt} = \nu_{i,j} r_j \quad (20)$$

The reaction rate r_j is proportional to the concentrations of the reacting species and reaction rate coefficient k_j which is characteristic of the respective elementary reaction j . If the reverse reaction is also taken into account with the coefficient k_{-j} :

$$r_j = k_j \prod_{i=1}^N [X_i]^{\nu_{i,j}} - k_{-j} \prod_{i=1}^N [X_i]^{\nu_{i,-j}} \quad (21)$$

Determination of reaction coefficients as well as study of their temperature and pressure dependence in addition to finding reaction mechanisms is the main task of the reaction kinetics.

2.3.1. Temperature dependence of reaction rates: Arrhenius equation

The temperature or pressure change of a system has an effect on the reaction rate of the elementary reactions. The often strong temperature dependence of the reaction rate coefficient can be typically expressed using Arrhenius equation with a good approximation:

$$k(T) = A e^{-\frac{E_a}{RT}} \quad (22)$$

The activation energy E_a corresponds to the minimum required energy in the reaction procedure to overcome the energy barrier. A is pre-exponential factor, R is the universal gas constant and T is the temperature.

$$\ln k(T) = \ln A - \frac{E_a}{RT} \quad (23)$$

Thus, the Arrhenius equation indicates that $\ln k(T)$ depends linearly on $1/T$.

According to the logarithmic form of the Arrhenius equation, E_a is defined by the slope of the plot.

$$E_a = -R \frac{d \ln k(T)}{d \frac{1}{T}} = RT^2 \frac{d \ln k(T)}{dT} \quad (24)$$

The activation energy must not be equated with the theoretical description of the reaction barriers that is used for the reaction threshold energy. Tolman described the activation energy as the difference of the average energy of reacting species and the average energy of all species [47]. It is reasonable to approximate the activation energy and the pre-exponential factor is

temperature independent. However, this assumption can usually be made only for small temperature ranges. For large temperature ranges, it is often suitable to introduce further temperature-dependent factors:

$$k(T) = BT^n e^{\left(-\frac{E'_a}{RT}\right)} \quad (25)$$

It should be noted that in this equation E'_a does not correspond to the activation energy of the original Arrhenius equation.

3. Tracer-based laser-induced fluorescence

The tracer-based LIF diagnostics is frequently applied in several fields such as chemistry, physics, engineering, biology, and medicine. Tracers are molecules or atoms that yield strong LIF signal intensities from which desired quantities about the local conditions in the gas phase are obtained with sufficient temporal and spatial resolution. In recent years, the application of tracer-based LIF spectroscopy have become important tools to better understand quantitative processes even under extreme physical conditions like high temperature and high pressure in practical combustion systems such as in IC engines [4, 5]. Path-integrated measurements such as absorption measurements do not typically give local information. In contrast, optical diagnostic techniques such as tracer-based LIF are well suited for quantitative measurement and are convenient choices to study fuel concentration, equivalence ratio, and temperature in combustion applications [48-50]. Suitable lasers and detectors enable one- to three-dimensional observations [31, 32] after quantifying the results using high spectral and temporal resolution.

Commercial fuels consist of several hundred varying components (e.g., paraffin, olefin and aromatic hydrocarbons). Due to the unknown individual fuel composition and the large number of fluorescent species, it is not possible to precisely determine which species and to what extent fluoresce. Therefore, these fuels are not suitable for investigations via LIF. Therefore, IC engine measurements are typically carried out using known amounts of tracers added into a so-called primary reference fuel (PRF). The primary reference fuels are made up of different mixtures of iso-octane and n-heptane that have no fluorescence and are also convenient to study via detailed chemical kinetics simulations. Two-component PRFs are the simplest fuel systems that can be applied to match up with the real fuels, but also more complex multi-component surrogate fuels are being used.

The choice of the appropriate tracer depends on several criteria and the conditions provided by the application. In particular, the evaporation properties of the tracer should match those of the fuel. Therefore, low volatile tracers are typically compatible with Diesel surrogates whereas high volatile tracers are typically applied for gasoline. In addition, the spectroscopy of the tracer should be convenient to permit the use of available laser sources. Also, fluorescence intensities of many tracers are strongly influenced by the presence of molecular oxygen because of collisional quenching. This effect can be exploited to determine fuel/air equivalence ratios in pre-combustion mixing. One important criterion is related to the signal intensity, which should be strong. Another important criterion is related to the decomposition kinetics that is often not considered when choosing tracers – mostly because of the lack of data.

One uncommon class of fluorescence tracers are small di- and tri-atomic inorganic molecules (e.g., I_2 , NO, SO_2). Since iodine (I_2) is not chemically stable in a reactive environment, it has been applied in non-combusting systems [51, 52]. Thermodynamic stability and accessible excitation wavelengths of sulphur dioxide (SO_2) make its application in flames possible.

However, strong quenching of SO₂ by many molecules such as N₂ as well as its toxicity and corrosiveness hinder its practical applications [53, 54]. LIF of nitric oxide (NO-LIF) is a well-known example of inorganic tracer that is frequently used for the flow visualization and gas-phase thermometry in both non-reacting and reacting systems, although during many combustion processes NO is formed as a reaction product in significant amount and therefore seeding of NO may not be needed [55, 56]. Toxicity and/or corrosiveness of all these three species restrict their practical applicability. In recent years, organic species have become popular tracers for imaging techniques to investigate gaseous flows and in-cylinder combustion processes. In comparison to atoms and small inorganic molecules, the high density of vibrational states in organic molecules results in broadband absorption, which permits the direct utilization of radiation generated from high-power lasers (e.g., 248 nm (KrF excimer) and 266 nm (fourth harmonic of Nd:YAG)) for excitation.

A variety of organic tracers (e.g., aromatics, ketones, aldehydes, and amines) with different sizes, structures, and volatilities have been used for experimental studies in fluid mechanics and combustion. Specific spectroscopic properties of ketones and aromatic hydrocarbons make the application of these groups of organic molecules more attractive as fluorescence tracers. Single-ring (e.g., toluene) and double-ring (e.g., naphthalene) aromatic derivatives are abundantly present in gasoline and Diesel fuels. Due to broadband absorption spectra, high fluorescence quantum yield, chemical similarity to hydrocarbon fuels and strong dependence of the LIF signal intensity upon oxygen concentration (quenching), aromatics are favored in many situations. In the case of ketones (e.g., acetone and 3-pentanone), their insensitivity to oxygen quenching and their visible fluorescence emission make them a better choice where constant LIF signals proportional to the local tracer concentration is required.

The photophysics of some aromatics and ketones have been studied over recent years [5, 39, 57], including high temperatures and pressures. However, other tracer candidates such as methylated benzenes (e.g., p-xylene (p-XL) and 1,2,4-trimethylbenzene (1,2,4-TMB)) and methoxybenzene (anisole), are just appearing and the temperature dependence of their fluorescence and absorption properties is not yet fully characterized. In general, there is still a significant lack of fundamental understanding of the photophysics and kinetics of many other tracers especially at conditions relevant for practical combustion environments.

Depending on the absorption spectrum of the tracer and the energy difference between the ground and excited state, UV lasers of various wavelengths are used. Typically excimer lasers ($\lambda = 248$ nm or 308 nm) or frequency-quadrupled Nd:YAG laser ($\lambda = 266$ nm) are used to excite the tracers [7, 49, 50, 58, 59]. Attenuation of laser light along its input direction to the measurement volume must be kept as small as possible. This is typically accomplished with an appropriate combination of selected tracer, tracer concentration, and excitation wavelength. The light absorption of a molecule depends on wavelength and temperature (Sec. 2.1.1). For the most common tracers (e.g., toluene and acetone), temperature and wavelength-dependent

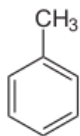
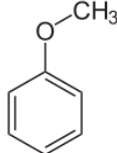
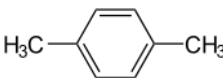
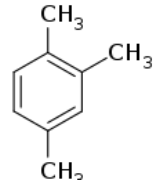
absorption and emission spectra are available [12, 60]. However, there is a lack of spectroscopic information for many others.

The selection of optics and the detection system is based on the emission spectra of the tracer. Whereas conventional image sensors and optics can be used for the detection of fluorescence in the visible spectral range, detection of LIF in the UV requires the use of specialized equipment. Since the fluorescence of common organic tracers is predominantly in the UV, more expensive UV-transparent optics and UV-sensitive imaging systems are required (Sec. 4.2).

3.1. Single-ring aromatics tracers

Single-ring aromatic species are frequently used as LIF tracers due to their possible natural occurrence in commercial fuels. The large absorption cross-sections in the UV range, the high fluorescence quantum yields, and the appropriate thermodynamic properties such as high vapor pressure make them suitable for measurements in practical devices (e.g., prior to combustion phase in engines). The broadband absorption spectra of single ring aromatics (220–300 nm) can be easily reached with commercial lasers. Strong UV lasers stimulate the $\pi \rightarrow \pi^*$ electronic transition (cf. section 2.1.2) and consequently the fluorescence bands appear between 250 and 360 nm. Some thermodynamic properties of aromatics studied here are provided in Table 1.

Table 1: Thermodynamic properties of the investigated aromatic tracer compounds

Tracer	Toluene	Anisole	p-Xylene	1,2,4-Trimethylbenzene
Structure				
Chemical formula	$C_6H_5CH_3$	$C_6H_5OCH_3$	$C_6H_4(CH_3)_2$	$C_6H_3(CH_3)_3$
Molecular mass / g/mol	92.1	108.1	106.2	120.2
Density at 293 K / g/cm ³	0.86	0.99	0.86	0.88
Melting point / K	178	236	286	229
Boiling point / K	384	427	411	442
Vapor pressure at 293 K / mbar	29	3.6	8.7	2.8

Reliable and quantitative application of tracer-based LIF of a tracer at high temperature requires knowledge about photophysical properties and its thermal stability of tracer species. In most of studies, it is usually assumed that the added tracer characteristics follows those of the parent fuel by matching the thermodynamical and chemical properties of the tracer/fuel combination. However, in the case of high-temperature applications, the depletion of the tracer and the parent fuel is not necessarily concurrent and the tracer and/or the fuel can experience chemical reactions before the onset of the main combustion process. Therefore, in experi-

ments where measurements at high temperatures (>700 K) are considered, the thermal stability limit of the tracer and potential effects of decomposition of tracer or interfering emissions or absorption originating from the decomposition products on the tracer signal must be understood. Nevertheless, in some cases species formed during the decomposition processes might be used as nascent fluorescence tracers for imaging at higher temperatures [22, 23].

Toluene

Among the aromatic hydrocarbons found in commercial fuels, the methylated benzenes (toluene, XL and TMB) comprise relatively high concentrations in commercial gasoline and Diesel fuels (about 25 and 33% by volume on average, respectively [61]). Toluene is the simplest methylated benzene that is frequently used as a fluorescent tracer for engine applications because of its strong fluorescence signal. Toluene alone exists typically with 5–15 Vol.% in commercial gasoline [62, 63].

Photophysical properties of toluene at elevated temperatures have been extensively studied by several groups [12, 16, 40]. They have mostly studied the fluorescence spectra of toluene upon excitation at 266 and 248 nm. The broadband absorption spectrum of toluene has a maximum around 260 nm at room temperature that shifts to longer wavelength with increasing temperature. The broadband emission spectrum shows also red shift with increasing temperature by approximately 2 nm per 100 K. The fluorescence signal intensity decreases exponentially by three orders of magnitude from 300 to 950 K at 1 bar upon a laser excitation at 266 nm [12, 40].

The limited thermal stability of toluene at high temperature has restricted previous experiments on its spectral properties in flow cells to temperatures below 1100 K [11, 12]. In the compression phase of combustion in IC engines the fuel-air mixture is heated significantly within a short time of few milliseconds. At high temperatures, decomposition of the fuel or tracer may lead to auto-ignition of the mixture. In addition, tracers which are applied in the IC engines might also undergo a concentration decrease before the beginning of the ignition. In this case the tracer LIF intensity cannot longer represent the concentration of the fuel. Sick and Westbrook have shown that gas-phase decomposition of toluene proceeds with a different rate than the decomposition of typical model fuel components such as *iso*-octane or *n*-heptane [19]. This result highlights the need for to understand the fate of toluene when used as tracer.

The kinetics and mechanism of the thermal decomposition of toluene in the gas phase,



have been intensively investigated both experimentally and computationally [64-66]. The main unimolecular reaction channels of toluene are C-H bond fission (R4) forming an H atom and the resonance stabilized benzyl ($\text{C}_6\text{H}_5\text{CH}_2$) radical [66], and C-C bond fission (R5) producing methyl (CH_3) and phenyl (C_6H_5) radicals [65]:



The products of R4 and R5 can undergo subsequent reactions, which need to be accounted for in the kinetics modeling of toluene pyrolysis.

Anisole

Anisole was recently suggested as a fluorescence tracer for combustion applications due to its favorable optical properties [13, 14, 39]. Hirasawa et al. [67] performed LIF measurements of seven fluorescent species including anisole to propose the best pair of fluorescent species for gas-temperature imaging based on two-color LIF. Pasquier et al. [68] chose anisole as a tracer due to its sensitivity to O_2 quenching for measurement of the equivalence ratio. Tran et al. [14] investigated the influence of temperature, pressure, and ambient gas composition on absorption, fluorescence, and the relative fluorescence quantum yield $\phi_{\text{fl}}(T)$ in a high-temperature cell up to 823 K and at 1 bar. Faust et al. [13] studied fluorescence spectra, lifetimes, and relative $\phi_{\text{fl}}(T)$ after 266-nm excitation up to 977 K and compared relative LIF-signal intensities of anisole with toluene, naphthalene, and acetone in a gas jet upon 266-nm excitation [39]. They have shown that anisole yielded the strongest fluorescence in both N_2 and air. Figure 10 demonstrates a comparison of signals per volume for anisole, toluene, naphthalene, and acetone in nitrogen and air at room temperature, relative to those of toluene in N_2 . Anisole exhibits the strongest signal even in air which makes it suitable for LIF diagnostics applications [39].

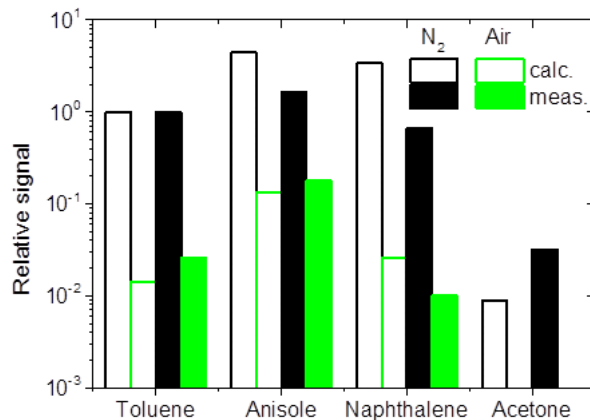


Fig. 10: Measured and calculated signals per volume in N_2 and air (acetone only in N_2) relative to those of toluene in N_2 at room temperature [39].

The spectroscopic properties of anisole have not been studied before at temperatures above 977 K, nevertheless these temperatures are relevant for measurements in IC engines. Under such conditions, thermal decomposition of anisole is one concern. Also, the decomposition products might interfere with the anisole-LIF wanted signals. Several studies investigated the

thermal decomposition of anisole [69-73] that occurs through C–O bond dissociation in the methoxy group forming CH₃ and the resonance-stabilized phenoxy radical (C₆H₅O). C₆H₅O can undergo subsequent bimolecular reactions towards phenol (C₆H₅OH) or cresol (C₆H₅CH₃OH) or unimolecular decomposition towards cyclopentadienyl (C₅H₅) and CO.



Nowakowska et al. [72] proposed a detailed kinetics model for the pyrolysis and oxidation of anisole based on a combustion model for light aromatic compounds. The kinetics mechanism was validated against experimental data studied in a jet-stirred reactor coupled with gas chromatography and mass spectrometry. They have postulated C₅H₅ as a main decomposition product and a precursor for the formation of benzene, naphthalene, and PAH.

p-XL and 1,2,4-TMB

p-XL and 1,2,4-TMB exhibit similar photophysical characteristics, therefore, they are reviewed here simultaneously. As already mentioned, it is necessary to develop surrogate fuels with known proportions and properties of components that mimic the behavior of real fuels such as gasoline, Diesel, and jet fuels. In addition to the frequently used toluene, alternative methylbenzenes (e.g., *p-XL* and 1,2,4-TMB) were suggested and partly investigated as fuel tracers due to their presence in real fuels and significant signal intensities [40, 42, 74]. The relatively low boiling point of *p-XL* (138.3°C) makes it compatible to gasoline-type fuels. In contrast, 1,2,4-TMB has evaporation characteristics comparable to Diesel and kerosene (boiling point at 170°C). In addition, studying the behavior of methylbenzenes is necessary for understanding the behavior of larger and more complex aromatic molecules that also present in large amounts in real fuels. Although toluene is one of the relatively well studied fluorescence tracers, studies of photophysical properties and gas-phase kinetics of *XL* and *TMB* are sparse. Consequently, there is an urgently requirement of background data to make these tracer candidates with high potential applicable for LIF measurements at high temperatures.

Rosow [40] studied the temperature-dependent relative fluorescence quantum yields (FQY) of 1,2,4-TMB. He reported that the variation in FQY regarding temperature, pressure, and oxygen partial pressure changes is analogous to that of toluene. Benzler et al. [41] have presented the fluorescence lifetime of 1,2,4-TMB for pressures up to 1 bar in the 295–475 K range. They reported a change of FQY with increasing pressure and rising temperature, which could be explained by the difference of the relative thermal energy distribution and the excess energy right after excitation in the S₁ state. Recently they investigated the dependence of the absorption cross-sections and fluorescence lifetimes of 1,2,4-TMB, respectively up to 725 K

and 1075 K, in N₂ from 1 to 10 bar total pressure and in N₂/O₂ mixtures with varying O₂ partial pressures at 1 bar total pressure [42].

Previously, no study on photophysical behavior of p-XL, i.e., its absorption cross-section, FQY, and the evolution of fluorescence spectra at high temperature has been published. A thorough search of the relevant literature yielded only one related article. Wang et al. [74] explores the characteristics of absorption and fluorescence spectra of p-xylene in N₂ upon 266-nm laser excitation within the very small temperature range i.e., from 423 to 623 K for absorption and from 428 to 523 K in the case of fluorescence. They reported that fluorescence peak intensity drops by a factor of three by 100 K increase in temperature.

Very few reaction mechanisms have been developed for single-ring aromatics heavier than toluene with methyl substituents and the development of the XL and TMB sub-mechanisms has been based mainly on toluene [75-77]. Roubaud et al. [78, 79] studied the autoignition of alkylbenzenes in a rapid compression machine at temperatures between 600 and 900 K and at pressures up to 25 bar. They separated the alkylbenzenes into two groups. First group contains compounds that only ignited at temperatures above 900 K and 16 bar (e.g., toluene, p-XL, and 1,3,5-TMB) and second group that ignited at much lower temperature and pressure (e.g., o-XL, 1,2,4-TMB). This was ascribed to the availability of ortho alkyl groups with more easily H-atoms transfers in the alkylbenzylperoxy radicals (C₆H₅CH₂OO) that lead to chain branching and higher reactivity.

Gail et al. [80-82] studied the oxidation of xylene isomers in a jet stirred reactor over a wide temperature range 900 to 1400 K at pressure of 1 bar and equivalence range of 0.5 to 1.5 and developed a detailed chemical kinetics mechanisms. Their study shows that the reactivity of p- and m-XL are quite similar whereas in comparison the reactivity of o-XL is much higher. This corroborates the observations by Roubaud et al. [79] where the ignition delay times of p- and m-XL were similar but the ignition delay times of o-XL were considerably shorter.

Battin-Leclerc et al. [75] developed a comprehensive kinetics model for the oxidation of all xylene isomers. They validated the predictions of their mechanism with their shock tube ignition measurements for temperatures from 1330 to 1800 K, pressures from 6.7 to 9 bar and equivalence ratios from 0.5 to 2.0. They also obtained reasonable agreement for m- and p-XL with literature data in a flow reactor at ~1150 K observed by Emdee et al. [83]. However, they observed no apparent difference in the reactivity of the three isomers at their conditions behind reflected shock waves. Early kinetic study of [84, 85] observed that p-XL was much less reactive with oxygen than o-XL. Later, Shen et al. [61] investigated the autoignition of xylene isomers using a shock tube at temperatures between 941 and 1408 K at pressures of 9 to 45 bar and equivalence ratios of 0.5 and 1.0.

Bikas [76] proposed a detailed chemical kinetics model for 1,2,4-TMB as a component in a kerosene surrogate fuel. He assumed that the initial oxidation of 1,2,4-TMB is dominated by side-chain chemistry due to the H-abstraction from the methyl group at position 4. The model was compared with the experimental data of ignition delay times from Roubaud et al. [79]

near 900 K, critical conditions of autoignition obtained using a counterflow burner for non-premixed flows and also species measured in a jet-stirred reactor such as 1,2,4-TMB and some intermediate species as well as products. Honnet et al. [77] developed a mechanism for a surrogate fuel of 80% n-decane and 20% 1,2,4-TMB by weight for kerosene-type fuels based on improved mechanism of Bikas [76]. They reported the critical conditions of extinction and autoignition as well as volume fraction of soot in laminar non-premixed flows.

3.2. Acetylene

In many practical applications unwanted fluorescence signals that originate from interference might affect species specific measurements as well as signal quantification. Consequently, for the respective species, the effective absorption cross-section at selected wavelengths must be known to assess laser and signal attenuation. Species that are assumed fully transparent in the respective wavelength range at room temperature, such as CO₂ and acetylene (C₂H₂), are often ignored as potential sources for the above mentioned interferences also at high temperatures. It is established that UV light attenuation [86, 87] as well as fluorescence [88] increases, e.g., during the flame evolution in engine experiments due mainly to the CO₂ contribution. In this case, spatial and temporal variations of absorption cross-sections within the combustion process provide an important benchmark for the quantification of signal intensities. The species responsible for these effects are, however, not fully investigated.

For wavelengths frequently used for laser diagnostics, the thermal excitation of bending modes in the electronic ground state of the linear molecule leads to a strong increase in absorption cross sections in the UV from virtually zero at room temperature to significant values. In the case of CO₂ [89, 90], for instance, it was shown that absorption is followed by fluorescence that could spectrally interfere with other measurements or could provide diagnostics capabilities – or subject of correction when other tracer are used – in high-temperature applications when excited with a laser [20, 91].

In analogy, C₂H₂ is present in many high-temperature processes where larger hydrocarbons undergo pyrolysis [92]. Acetylene is also known to participate in soot forming reactions [93, 94]. C₂H₂ is the lightest unsaturated hydrocarbon and as a non-toxic fuel used, e.g., in welding torches. Previous publications noted that C₂H₂ has no spectral absorption above 240 nm and the first signs of acetylene absorption start at approximately 237 nm and continues towards shorter wavelengths [95, 96]. The reported studies were limited to the 210–240 nm wavelength range [95-100]. In this range, the absorption is related to the vibrational bands in the S₀($\tilde{X}^1\Sigma_g^+$)→S₁(\tilde{A}^1A_u) electronic transition [96].

Spectroscopic background

The equilibrium geometry of the acetylene molecule changes during electronic excitation. The ground electronic state (S₀) of acetylene is linear (D_{∞h}) and at lowest excited singlet state (S₁) it has a planar trans-bent equilibrium geometry (C_{2h}) [98, 101]. Therefore, the transition

probability from vibrationless states at room temperature is negligible unless bending vibrational modes are excited in the electronic ground state at high temperature. Similar to CO_2 , C_2H_2 therefore exhibits an onset of absorption only at elevated temperatures with an unexpectedly strong increase in absorption in the UV at high temperature.

Watson et al. [96] and Van Craen et al. [100] presented a detailed vibrational and rotational analysis of the $\tilde{\text{A}}-\tilde{\text{X}}$ band system. Brus [97] obtained the first fluorescence spectrum of acetylene at 4 K in solid neon and in solid argon excited by an ArF laser (193.3 nm). Hamai et al. [102] have observed a weak emission with a maximum at 320 nm from gaseous C_2H_2 upon 200 nm excitation. They have also reported a fluorescence yield of acetylene about 10^{-4} at 667 mbar for 200 nm excitation. Later, Stephenson et al. [103] observed the fluorescence excitation spectrum of gaseous acetylene at room temperature with laser excitation at 230 nm and Raiche et al. [99] investigated fluorescence in the UV/VIS region using excitation at 215.9 nm in acetylene low-pressure flames where they monitored C_2 fluorescence, which provided much stronger signals than acetylene fluorescence. Williams et al. [104] extended these investigations to acetylene fluorescence following excitation at wavelengths up to 450 nm and lower laser fluence. They demonstrated that acetylene can be detected in flames with reasonable signal-to-noise ratios as an intermediate species formed as a combustion intermediate by laser-induced fluorescence with excitation at 225–235 nm. Osborn and Frank [105] used laser-induced fragmentation fluorescence (LIFF) to detect C_2 from acetylene and vinyl radicals among other prospective C_2 precursors at low pressure (6.67 mbar) in a room temperature cell. They have shown that vinyl produced significant C_2 Swan band emissions compared to C_2H_2 after excitation at 230 nm. The latter requires multi-photon excitation resulting in C_2 -LIF intensities three orders of magnitude lower than the LIF signal from the vinyl precursor. Recently, Miles et al. [106] investigated the effect of excitation wavelength and temperature on the C_2 fluorescence from C_2H_2 in the visible range at 295, 600, and 800 K for atmospheric pressure using broadband excitation at 210–240 nm and LIFF detection. They have observed significant C_2 emissions at excitation wavelengths that are non-resonant with acetylene $\tilde{\text{A}}-\tilde{\text{X}}$ transitions at elevated temperatures.

Near- and mid-infrared absorption has frequently been applied for measuring acetylene concentration during pyrolysis and oxidation of fuels [107–111]. Line-of-sight absorption methods provide high sensitivity but are best applied to homogeneously absorbing media. Therefore, in inhomogeneously distributed media, such as reactive flows, fluorescence-based diagnostics may be advantageous.

The only study at high temperatures in the UV reported the absorption cross-section of C_2H_2 measured in a heated and pressurized quartz cell at 873 K between 195 and 250 nm and at 1073 K between 195 and 300 nm [112]. The authors have shown an increase of absorption with temperature but the temperature range they could investigate is insufficient for combustion conditions. Because of the comparably long residence time of gases in heated cell experiments, the limited stability of C_2H_2 at high temperature restricts the maximum temperature.

The absorption measurements showed a strong increase in absorption cross-sections of C_2H_2 in a temperature range where no decomposition products occur on the shock-tube experimental timescale (cf. Sec. 5.4). It allows to study the laser-induced fluorescence of C_2H_2 that might occur in combustion systems as an unwanted interference, e.g., in tracer-based measurements of fuel evaporation and mixing studies; this signal might on the other side provide new diagnostics capabilities, e.g., for imaging measurements of C_2H_2 that exists in high concentrations as pyrolysis product of hydrocarbon fuels. For quantitative LIF measurements, knowledge of the temperature dependence of the fluorescence quantum yield and potential variations in emission spectra is crucial.

3.3. Bath gas selection

Selection of an appropriate bath gas for the tracer-based LIF spectroscopy is extremely important. The first feature of a suitable bath gas is that the bath gas should not absorb or fluoresce light in the considered wavelength range for tracers. The second feature is that the bath gas should not have an effect on the shape or position of absorption or fluorescence spectra except when the effect of the bath gas on spectra is a part of study (for example quenching by molecular oxygen). The third important point for selection of a bath gas is the thermal stability of the bath gas, thus at high temperatures it must not decompose and/or react with the tracer again except if it is a part of study. Generally, noble gases and nitrogen are chosen as the bath gas for study the oxygen free environment and a composition of nitrogen and oxygen or air are used to investigate photophysical effects of O_2 as well as combustion of tracers.

4. Experiment

4.1. Shock-tube facility

Measurements were performed in a stainless-steel diaphragm-type shock tube. The shock tube has an inner diameter of 80 mm. The driven section (length of 8 m) was separated from the driver section (length of 3.6 m) by an aluminum diaphragm (thickness 20–90 μm). The driver section of the shock tube is evacuated to 1×10^{-3} mbar by a rotary vane pump (Leybold Vacuum GmbH, TRIVAC D 16 B) and the driven section is evacuated using a turbomolecular pump (Leybold Vacuum GmbH, turbovac 361 C) which enables pumping the tube down to 1×10^{-7} mbar in between experiments. The test gas mixtures are prepared in a stainless-steel vessel (60 l, evacuated by a turbomolecular pump Edwards EXT255DX down to 1×10^{-7} mbar). The mixing vessel is filled with the tracer vapor to the desired partial pressure, which is then diluted with a bath gas (e.g., argon and N_2) to achieve the desired concentration. Gaseous mixtures were allowed to homogenize at least 12 h before use. Both the incident and reflected shock-wave velocities are measured by four fast response adjacent (200 mm to each other) piezoelectric pressure transducers (603B, Kistler). The last pressure transducer is placed 5 mm upstream of the endwall of the tube. The amplified signals (Kistler Kiag Swiss 5001) are then recorded by an oscilloscope. Temperature and pressure behind the reflected shock wave are calculated from the velocity of the incident shock wave and the initial conditions in the driven section based on standard ideal-gas shock-wave relations [113]. The post-shock conditions can be varied between post-reflected-shock temperatures (T_5) of 550–2500 K and pressures (p_5) of 0.9–3.7 bar. Figure 11 shows the schematics of the shock-tube facility.

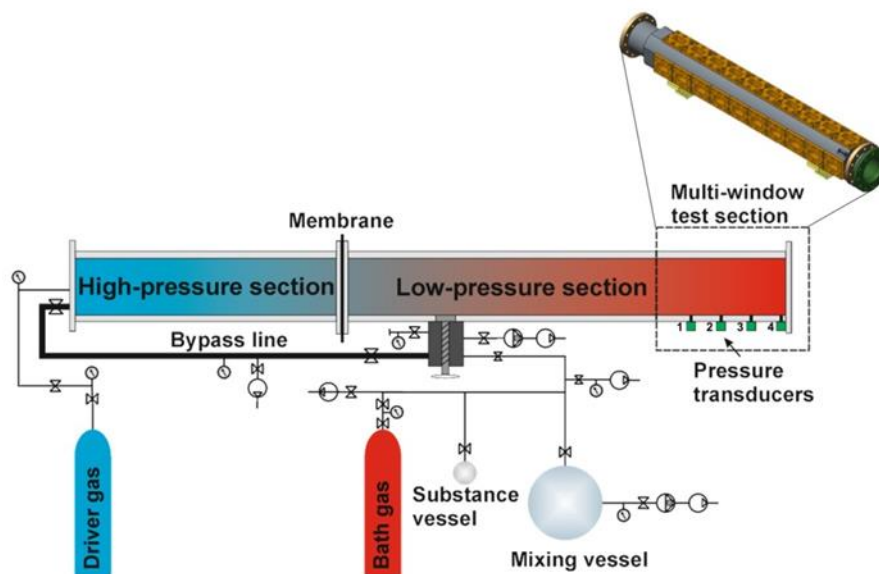


Fig. 11: Schematics of the shock-tube facility [114].

4.1.1. Multi-window test section

The measurement section of the shock-tube facility described here has been modified specifically to allow simultaneous measurements of RTR-LIF (see Sec. 6) at variable locations and absorption. Drawings of the test section are shown in Fig. 12. The top and side walls provide nine ports for rectangular windows in three groups along the length (1 m) of the test section. Each window has a width of 25 mm and length of 45 mm. Four circular windows (10 mm diameter) are arranged diagonally across the tube near the end flange.

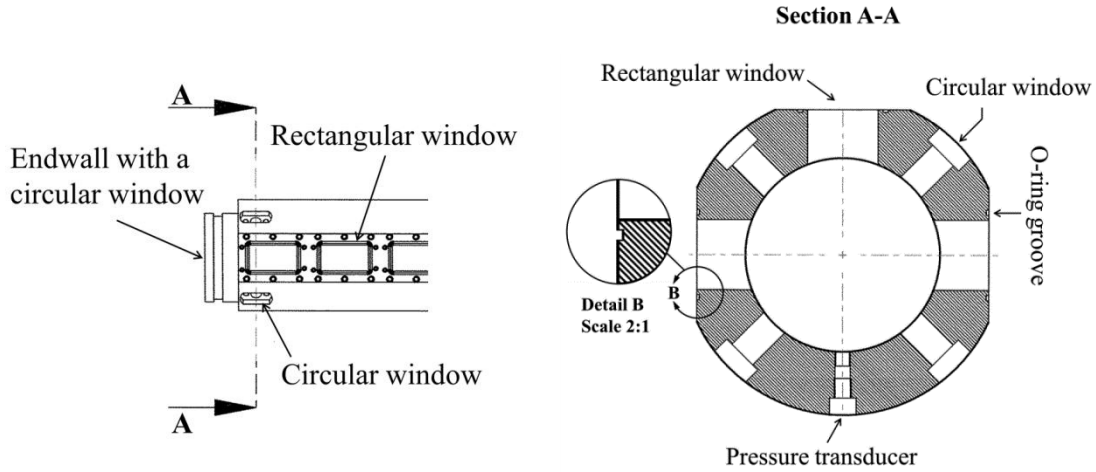


Fig. 12: Drawings of the test section [114].

Top and side windows are mounted at wall ports with O-ring seals (Viton). To prevent perturbation of the shock wave, the inner face of the rectangular windows followed the shape of the tube curvature. To minimize optical distortion, the windows were designed like concave-convex (meniscus) lenses and the relative curvatures of the two surfaces were calculated from the lensmaker's equation to obtain zero optical power ($P = 1/f = 0$).

$$\frac{1}{f} = (n - 1) \left[\frac{1}{R_1} - \frac{1}{R_2} + \frac{(n - 1)d}{nR_1R_2} \right] \quad (26)$$

Where f is the focal length, n is the refractive index of the UV-grade fused-silica window, R_1 and R_2 are the radii of curvatures of the windows and d is their thickness. A cross-section of the rectangular window is shown in Fig. 13 ($R_1 = 40$ mm, $R_2 = 44$ mm, $d = 12$ mm). The end-wall of the tube contains a flat-surfaced circular window with a diameter of 50 mm.

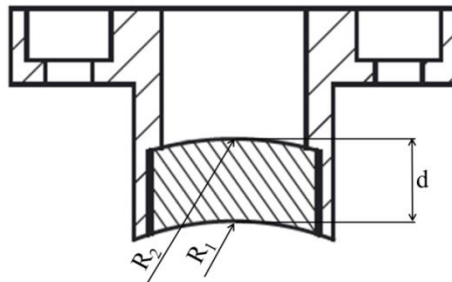


Fig. 13: Drawing of the rectangular side windows [114].

4.2. Excitation source and detection systems

4.2.1. Nd:YAG laser

For the electronic excitation of tracer molecules, lasers are required that emit laser light in the relevant UV range (typically below 400 nm). The Nd:YAG laser is a powerful solid-state laser that – due to its high pulse energy and short pulse time – is commonly used for instantaneous imaging of combustion processes within the desired short detection times. The active medium of these lasers is a neodymium-doped YAG (yttrium-aluminum garnet) rod of specific crystallization form in which about 1% of the yttrium ions are replaced by neodymium ions. The neodymium has an ideal four-level system. Figure 14 shows four-level laser system of a Nd:YAG laser. Generally, xenon flash lamps are used as a pump source. The Nd^{3+} ions of the upper pump state ${}^4\text{F}_{5/2}$ quickly relax with high yield into the laser output level ${}^4\text{F}_{3/2}$. The technically most energetic laser transition (1064 nm) occurs in the ${}^4\text{I}_{11/2}$ state, which is almost unoccupied in thermal equilibrium. From this state the Nd^{3+} ions relax again into the ground state ${}^4\text{I}_{9/2}$ until the pumping process starts again.

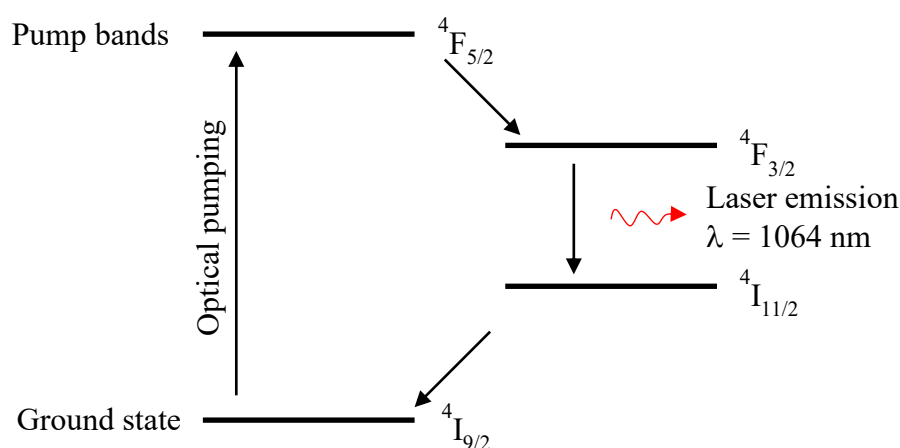


Fig. 14: The important energy levels of the Nd^{3+} ion in Nd:YAG laser process.

Typical pulse rates of such laser systems range from a few Hz to several kHz. To form short pulses with very high peak power, the laser has a Q-switch, which is implemented by a Pockels cell and polarizer. The Pockels effect causes a change when a voltage is applied to a suitable crystal by its birefringence properties, which rotates the polarization of the laser beam that passes through. Thus, the laser resonator can be alternately switched to low or high Q (quality factor). As long as the resonator is set to low Q , an increasing population inversion can build up in the cavity. If it is switched to high Q , the laser beam runs in the resonator, a part of the laser intensity is decoupled from the resonator through a semi-transparent mirror. Thus, a pulse with a length up to about 10 ns can be formed. With the aid of optically uniaxial double-refraction crystals (e.g., beta-barium borate, BBO), higher harmonics can be generated from the fundamental wavelength at 1064 nm [115]. Using a second harmonic generator (SHG), the initial wavelength of the laser light can be halved from 1064 nm to 532 nm. These crystals are temperature stabilized to ensure stable operation, the efficiency of frequency conversion is usually about 50%. By frequency mixing of this green (SHG) beam with the fun-

damental in another crystal third harmonic (355 nm) or fourth harmonic (266 nm) can be generated. The latter is the most common used wavelength in LIF measurements. The obtainable pulse energies in this case (266 nm) depend on the design and repetition rate of the laser and are usually 1–100 mJ/pulse.

4.2.2. Spectrometer

Spectrometers are important optical tools for the investigation of light spectra. For this purpose, the light typically enters the spectrometer via an entrance slit or a pinhole. This light is then collimated by a lens or a curved mirror and hits a dispersive element. Subsequently, the spectrum of light is refocused on a detector (CCD array) using a second lens or a second curved mirror. Optical spectrometers can be divided into two groups depending on the dispersive element, prisms or diffraction gratings. A grating as a dispersive element allows for looking closely at a small wavelength range, i.e., higher spectral resolution. Grating spectrometers can be also more easily adapted to the required spectral ranges. However, in grating spectrometer the intensity is divided into several diffraction orders which reduce the intensity of the measured radiation. This problem can be reduced with the help of blazed gratings. Reflection gratings have a stepped structure that promotes the diffraction in a certain direction, and are optimized for specified orders of diffraction. Thus, the intensity yield in the used diffraction order can be increased, but still the intensity is emitted in the unused diffraction orders and therefore lost for detection. Grating spectrometers with reflection gratings and mirrors are further recommended due to their compact designs. In contrast to prism spectrometers, in grating spectrometers no linear arrangement is required and the length of the overall setup is essentially given by the largest used focal length. In the simplest construction the grating is in the focus of a mirror and the entrance slit and the detector are symmetrically adjacent to the grating in the focal plane. The spectrometer usually allows to install additional gratings or exchange gratings and the central wavelength of the grating can be adjusted via a stepper motor. The general grating equation is usually written as:

$$n\lambda = d(\sin \alpha + \sin \alpha') \quad (27)$$

where n is the order of diffraction, λ is the diffracted wavelength, d is the grating constant (the distance between grooves), α is the angle of incidence measured from the grating normal and α' is the angle of diffraction measured from the grating normal. For a specific diffracted order and angle of incidence, different wavelengths will have different diffraction angles. A blazed grating therefore acts as a wavelength-selective mirror. Figure 15 illustrates grating angles (left) and terms and the schematic structure of a grating spectrometer (right). The incident radiation of the light source is focused on the entrance slit S of the spectrometer using a collecting lens L. The entrance slit is placed in the focal plane of a spherical mirror M_1 . The parallel light from M_1 is reflected by a diffraction grating G where due to diffraction on the reflection grating the image of the slit is laterally separated for the different wavelengths. Finally, the mirror M_2 images the S onto the detector D.

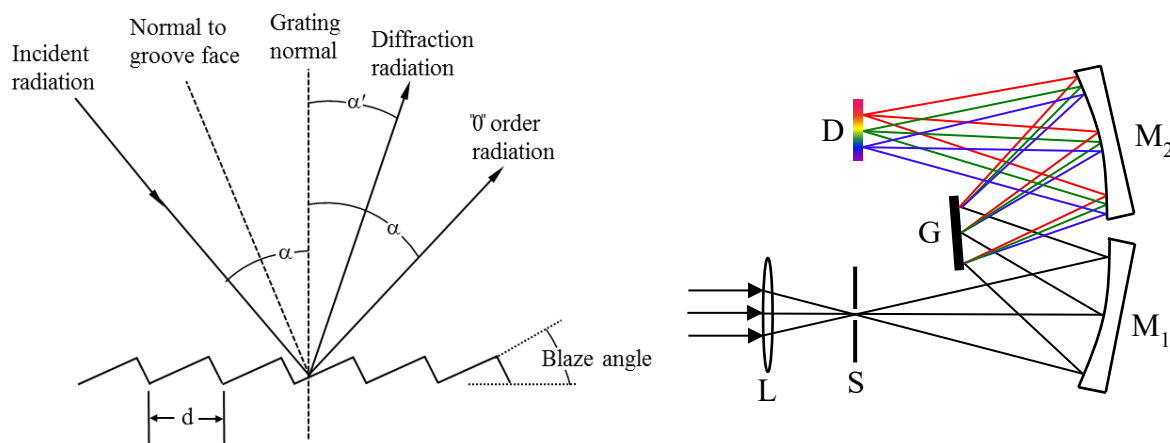


Fig. 15: Left: Illustration of the grating angles and terms [116]. Right: Schematic drawing of grating spectrometer principles [115]. L: Collecting lens; S: entrance slit; M₁ and M₂: Concave mirrors; G: diffraction grating; D: Detector (CCD array).

In spectrally-resolved LIF measurements, the detection system consists of an imaging spectrometer that is coupled to an intensified charge-coupled device (ICCD) camera at the exit port. The imaging spectrometer is perpendicular to the laser line and the entrance slit is parallel to the laser line. This means that the one axis represents the spatial coordinate along the laser line and the other axis transforms into the wavelength coordinate. In absorption measurements, however, a combination of an imaging spectrometer and an electron-multiplying charge coupled device (EMCCD) camera with kinetic mode option allows for spectrally and temporally-resolved absorption measurements (cf. Sec. 4.3.1).

4.2.3. ICCD camera

To detect the fluorescence signal in LIF measurements, an ICCD camera was used. The ICCD camera enables a two-dimensionally resolved detection of very low signal intensities, down to the single photon detection from the UV to the near-IR spectral range. Image intensifiers realize very short gate times (nanoseconds) in ICCD cameras compared to the conventional CCD cameras. They aid to increase significantly the signal of the camera to their readout noise by amplifying the low light. They also make it possible to change and improve the spectral sensitivity of the detection system in the UV by choosing an appropriate UV-sensitive photocathode for LIF measurements. The high signal sensitivity in presented measurements in this work is enabled by the image intensifier (LaVision Intensified Relay Optics (IRO)) lens-coupled to the CCD camera (Imager Intense, LaVision). In combination with a spectrograph, ICCD camera allows for spatially- (one-dimensional) and spectrally-resolved emission spectra. Figure 16 illustrates the optical part of an intensified CCD camera. The outgoing light of the observation volume from the spectrograph is projected on the entry window of the ICCD camera. The image intensifier is mounted in the optical beam path in front of the CCD camera for visualizing weak light events and converting UV light to the visible that can be detected with a standard CCD. An image intensifier consists of a photocathode that allows the conversion of the incident signal of photons in photoelectrons. These electrons are amplified in a micro-channel plate (MCP) according to the principle of an electron multiplier [117]. The emerging electrons

are accelerated to a phosphor layer and cause phosphorescence in the green spectral range. The phosphorescence light is imaged onto a CCD chip by an optimized lens coupling (tandem lens system). The CCD chip consists of multiple arrays of light-sensitive semiconductor elements, in which the incident photons cause a charge transfer. At the end of the image recording, the charges are read line by line and converted into image information using an Analog-to-Digital (A/D) converter. On the CCD chip, charges accumulate even without incident photons. This creates a certain thermal background of the images. It can be reduced by cooling the chip, however. For this purpose, a Peltier element is integrated in the camera and the chip can be cooled down to $-12\text{ }^{\circ}\text{C}$.

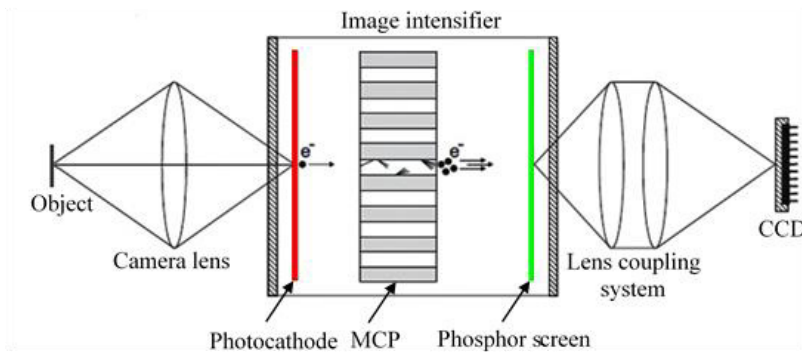


Fig. 16: Schematic cross-section of the optical part of an image-intensified CCD camera [118].

4.2.4. EMCCD camera

To detect the time-resolved absorption spectra, a single-photon-sensitive EMCCD camera (Andor Technologies, iXon) was used. Similar to conventional CCD cameras, electrons are released by the incidence of photons on a silicon semiconductor chip. The resulting charge in each pixel is shifted after a certain exposure time vertically to the next dark pixel, row by row and read out into an A/D converter (Fig. 17). The vertical shift speed (line-shift time) and the vertical clock voltage (amplitude) can be adjusted. For example, to reduce vertical smearing over several pixels, a fast vertical shift speed might be applied and for short line shift times ($< 1\mu\text{s}$) the amplitude can be increased to avoid signal smearing during the frame transfer [119]. The iXon EMCCD model has a back-illuminated CCD chip with UV-sensitizer coating that achieves high quantum yields (up to 90% quantum efficiency in the visible and 32% in the UV). The photo-active area of the chip has a square detection array consisting of 512×512 pixels (the size of each pixel is $16 \times 16\ \mu\text{m}^2$) and is read out by the frame transfer method. The signal is digitized with a conversion rate of 10 MHz and a depth of 14 bits.

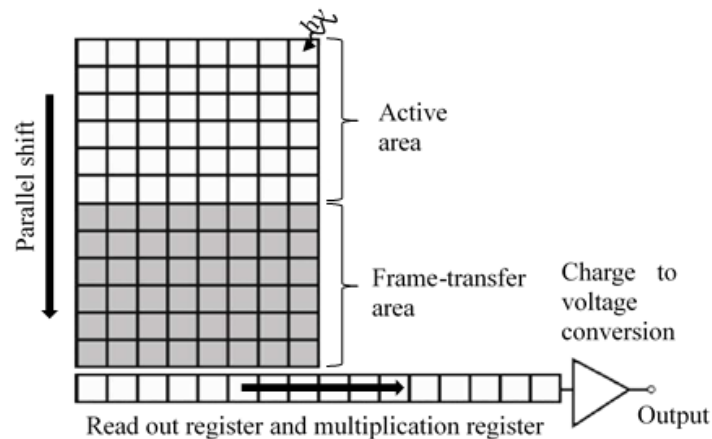


Fig. 17: Schematics of an EMCCD detector with frame transfer technology [119].

There are three dominant sources of read-out noise in EMCCD cameras, namely the dark noise, the spurious noise (Clock-Induced Charge, CIC) and the readout noise of the A/D converter. Thermally-generated electrons during the period of exposure are wrongly represented as a photon in the gain register. This effect can be reduced by cooling the sensor. In addition, single electrons are released during the vertical charge shift (CIC) from the sensor into the readout circuit and contribute to the noise. This restricts the vertical clock voltage for a faster vertical shift speed. In conventional CCD cameras under low-light conditions, the noise contributions are dominated by the readout noise. A weak signal (a small number of photons) cannot be detected against the read noise. The EMCCD technology reduces this problem by amplifying the signal. For this purpose, the charge is shifted at high voltage into a multiplication (gain) register, where additional electrons are generated by impact ionization. The amplification factor of this process can be adjusted by the shift voltage applied in the gain register. With a high gain of the signal before the readout, it is possible to detect single photons. At unity gain, an EMCCD behaves like a “regular” CCD.

4.2.4.1. Kinetic readout mode

The kinetic mode of the EMCCD camera is a specific readout mode in which only the first few lines of the CCD are illuminated while the rest of the active area is optically masked and used for storage a series of sub-frames prior to readout. This mode is useful for capturing transient events at high temporal resolution (microseconds). This is achieved by rapidly shifting each sub-frame exposure to the shielded area before reading it out. This continues until the whole frame-transfer area is filled. At the end of the exposure shift process, the entire frame can be read out. Typically, in spectroscopy the detector is coupled with an imaging spectrometer and the optically masked portion of the CCD is best obtained by limiting the height of the entrance slit of the spectrometer. In most of the applications, to achieve better time resolution as few rows as possible are illuminated. In our experiment, the illuminate range is seven rows high and no mechanical shutter is applied in front of the chip, therefore, good contrast at the exit of the spectrometer is required.

4.3. Experimental procedure

4.3.1. Time-resolved absorption measurements

The transmitted light that carries the absorption information from the species inside the shock tube was recorded temporally and spectrally resolved using the setup shown in Fig. 18. A deuterium lamp (30 W, Heraeus D200 F-HV) was used as a broadband UV light source. After collimation, the light passed through quartz windows mounted in the sidewall of the shock tube located 30 mm upstream of the endwall. After passing the exit window, the transmitted light was focused by an $f = 50$ mm quartz lens onto the entrance slit of an imaging spectrometer (Acton SP 2300i, Princeton Instruments, 300 g/mm grating, slit width: 300 μm leading to 3–7 nm spectral resolution). The spectrograph was coupled to a UV-sensitive back-illuminated EMCCD camera (Ixon, Andor, EM gain: 210, pre amplifier: 1 \times), which was operated in kinetic mode (cf. Sec. 4.2.4.1): After triggering the camera with the signal from pressure transducer #3 that recorded the passage of the incident shock wave, the collected charges on the CCD were shifted to the adjacent pixel rows perpendicular to the wavelength axis once every 3.2 μs . The focused transmitted light by far overfills the 170 \times 120 μm^2 entrance slit of the spectrograph. Using this rectangular opening, only the uppermost seven pixel rows of the CCD chip were illuminated resulting in a series of absorption spectra with a fundamental time resolution of ~ 20 μs covering a test time during the shock tube experiment of up to 1.6 ms (note that the observed time resolution was about 20–70 μs under operating conditions). Before each experiment a dark image was taken and subtracted from the measured image. Data acquisition was synchronized with a delay generator (DG535, Stanford Research Systems) using the signal of the pressure transducer #3 as trigger input. The wavelength scale of the spectrometer was calibrated using a low-pressure mercury discharge lamp.

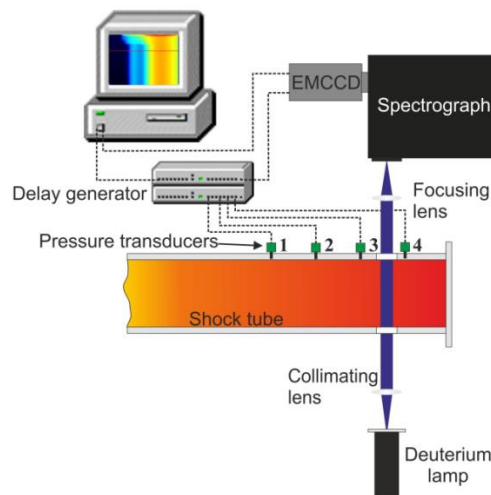


Fig. 18: Experimental arrangement for spectrally- and temporally-resolved UV absorption measurements in shock tube.

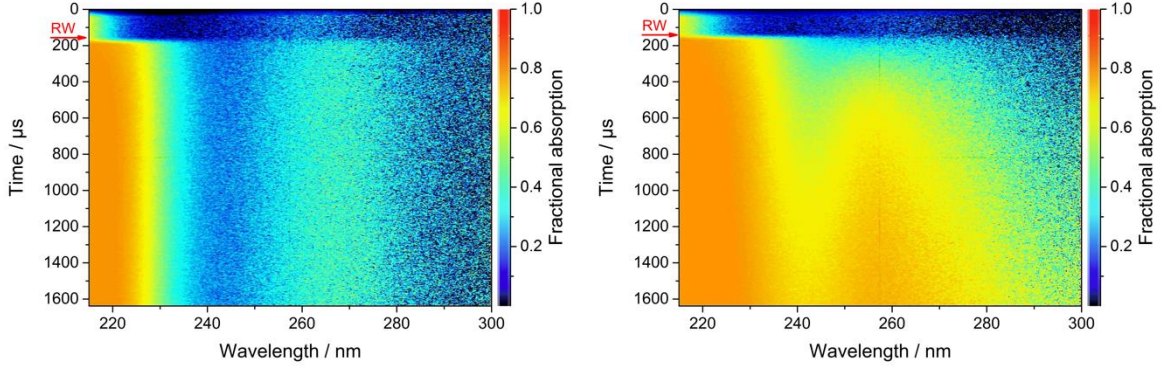


Fig. 19: Temporally- and spectrally-resolved fractional absorption of the shock-heated mixture of toluene in Ar. The arrival of the reflected shock wave at the detection volume is marked by “RW”. Post-reflected-shock conditions: Left: $T = 1140$ K, $p = 1.5$ bar, 2% toluene in Ar, right: $T = 1550$ K, $p = 2.1$ bar, 0.2% toluene in Ar.

Changes in the transmitted light intensity and hence the absorption spectra at various times were investigated by determining the fractional absorption $F(\lambda, t)$.

$$F(\lambda, t) = \frac{I_0(\lambda) - I(\lambda, t)}{I_0(\lambda)} \quad (28)$$

Here $I_0(\lambda)$ is the wavelength-dependent incident light intensity (signal averaged over 300 images with an empty shock tube) and $I(\lambda, t)$ is the time- and wavelength-dependent transmitted light intensity. The fractional absorption was calculated for specific wavelength ranges from both the incident and transmitted light by binning corresponding pixels on the wavelength axis as a function of time. Figure 19 shows typical examples of fractional absorption of the shock-heated tracer mixtures (here toluene in argon) as a function of time (y-axis) and wavelength (x-axis) for two different post-shock conditions. Because of the increase in density of the absorbing species behind the reflected shock wave, the light transmission decreases immediately and hence the fractional absorption increases. The left panel of Fig. 19 shows results from an experiment at 1140 K, where toluene is stable on the experimental time scale. As a consequence, the absorption spectrum remains constant during the constant high-temperature conditions behind the reflected shock wave. In contrast, the absorption spectrum at 1550 K changes as a function of reaction time, reflecting decomposition of toluene on the experimental time scale.

At low temperatures, where tracer pyrolysis is expected to be insignificant on the experimental time scale, data sets can be averaged in the time domain to optimize the signal-to-noise ratio. The absorption cross-section $\sigma(\lambda)$ of the tracer can be determined according to the Beer-Lambert law (Eq. 4) using the transmitted and incident light intensities $I(\lambda)$ and $I_0(\lambda)$, respectively, the known number density n of the tracer molecules after the reflected shock wave, and the path length l (i.e., the inner diameter of the shock tube). The absolute concentration of tracer behind the reflected shock wave is calculated from shock wave equations [120] based on the known mole fraction of tracer in the gas mixture and using the initial pressure (both total pressure and partial pressure of tracer) and temperature in the driven section

(T_1 and p_1) and the measured velocity of the incident shock wave. $I(\lambda)$ represents the time-integrated light intensity after passage of the reflected shock wave.

At temperatures where pyrolysis of the tracer cannot be neglected, it is possible to derive an effective absorption cross-section $\sigma_{\text{eff}}(\lambda, t)$ that is based on the initial tracer number density n_0 behind the reflected shock and accounts for tracer as well as its products.

$$\sigma_{\text{eff}}(\lambda, t) = -\frac{\ln(I(\lambda, t)/I_0(\lambda))}{n_0 l} \quad (29)$$

4.3.2. LIF measurements

The shock tube was alternatively equipped with a system for spectrally-resolved measurements of LIF at selected reaction times (Fig. 20). The gas mixture behind the reflected shock wave was excited by a pulsed frequency-quadrupled Nd:YAG laser (Quanta-Ray, Lab-150) at 266 nm with a pulse duration of ~ 6 ns. The laser beam diameter was reduced by a Galilei telescope to ~ 7 mm (fluence $\sim 10\text{--}35$ mJ/cm²) and directed through quartz windows in the side-wall of the shock tube 40 mm upstream of the endwall. The laser energy was measured using a power meter (LabMax-TOP, Coherent) during each experiment to assess and correct for laser pulse energy fluctuations. In the single-shot operation of the Nd:YAG laser, fluctuations were typically $\leq \pm 9\%$. The emitted fluorescence was collected perpendicular to the laser beam through a quartz window in the endwall of the shock tube and was focused on the entrance slit of a spectrograph (Acton SP 2150i, Princeton Instruments, 150 g/mm grating, 500 μm slit width resulting in a 10 nm spectral resolution) using two fused silica lenses ($f = 160$ and 90 mm). The spectrally-resolved light was recorded by an ICCD camera (Imager Intense, LaVision, 300 ns gate time).

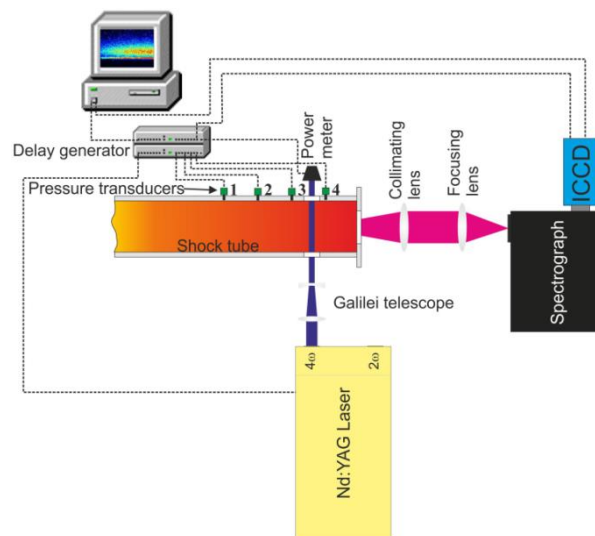


Fig. 20: Experimental setup for the LIF measurements.

The wavelength axis of the spectrometer was calibrated using a low-pressure mercury discharge lamp. The emission spectra of a deuterium (for $\lambda < 400$ nm) and a tungsten lamp (for λ

> 350 nm), respectively, with known spectral radiance were used to correct for the wavelength-dependent throughput and camera sensitivity.

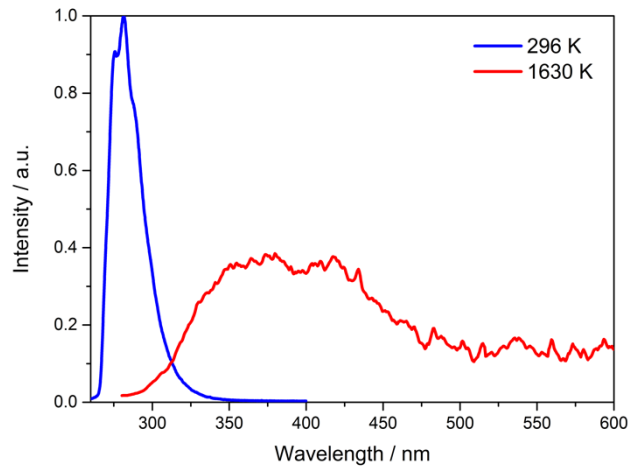


Fig. 21: Single-shot LIF spectra for an experiment with 1% toluene in Ar. Blue line: 296 K, 75 mbar, before the arrival of the shock wave; red line: 1630 K, 2.9 bar, 160 μ s after passage of the reflected shock wave.

Laser and camera were synchronized with the shock wave using a delay generator (DG535, Stanford Research Systems) using the signal of the incident wave recorded by the pressure transducer #4 as trigger input. For each shock-tube experiment, a single LIF measurement was taken at a selected time after the arrival of the reflected shock wave. The slit of the spectrometer was oriented parallel to the laser beam and thus in principle provided one-dimensional spatial resolution. However, since with the conventional LIF arrangement no spatial variation of the signal is expected for this coordinate, the fluorescence signal of the recorded image was integrated along the slit direction to improve the signal-to-noise ratio. A dark image taken before each experiment was subtracted from the measured image. Figure 21 shows two examples of LIF spectra, one recorded for toluene at room temperature, and the other for its reacting mixture at 1630 K, 160 μ s after the reflected shock wave.

As mentioned in section 2.1.4.1, the total detected LIF signal intensity of the tracer S_{fl} at a fixed excitation wavelength λ_{ex} and temperature T is proportional to the number density of tracer n , the absorption cross-section σ , and the fluorescence quantum yield ϕ_{fl} :

$$S_{\text{fl}} \propto n\sigma(\lambda_{\text{ex}}, T)\phi_{\text{fl}}(\lambda_{\text{ex}}, T) \quad (30)$$

For detailed information about LIF signal intensity refer to section 2.1.4.1.

4.3.3. Mass spectrometry measurements

Mass spectrometry (MS) is a powerful analytical technique that allows to determine molecular masses within a sample. It can be used together with spectral databases to identify unknown substances, their concentration and structural information. Mass spectrometry exploits the fact that ions can be deflected in the magnetic and electric field and thus separated by their

mass-to-charge ratio (m/z). In this work, multispecies concentration–time profiles of anisole and its decomposition products (see Sec. 5.2.2) were measured with a high-repetition-rate time-of-flight mass spectrometer (HRR-TOF-MS) coupled to the shock tube via a conical nozzle in the center of the end flange of a shock tube. It is equipped with an electron ion source with two-stage ion extraction, a two-stage reflectron, and a microchannel plate (MCP) detector. That enables repetitive measurements of mass spectra during the test time of the shock-tube experiment with repetition rates up to 150 kHz. This technique is explained briefly below. For details of the experiment i.e., shock-tube and HRR-TOF-MS with the corresponding modular sampling unit for measuring species concentrations, see Ref. [121].

Time-of-flight mass spectrometer with electron ionization

The process of mass spectrometry in an experiment has four phases which are test gas supply, ionization, mass separation, and ion detection. In this technique the gaseous sample is inserted through a valve or nozzle into the high vacuum ionization chamber of the mass spectrometer. The gas Inlet (e.g., a nozzle) is usually adapted for the intended experiment (here the shock tube). The modified inlet is directly connected to the ionization chamber. From the inlet nozzle a molecular cloud flows into the ion source. In mass spectrometry various ionization methods are used to generate gaseous ions that are transferred to an analyzer [117]. The TOF-MS used in this work is equipped with an electron ionization (EI) source. In the ion source, the incoming ions are bombarded with high kinetic energy electrons that are produced by a hot cathode (filament) and accelerated in an electric field. To avoid collisions of the ions with surrounding molecules (e.g., N_2 and O_2) ion production, mass separation and detection occur in high vacuum (typically $p < 10^{-5}$ mbar) conditions. Figure 22 shows a common structure of an EI source featured in a mass spectrometer as ionization method.

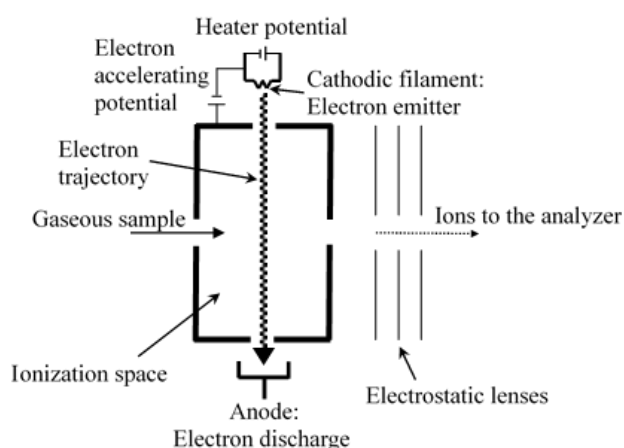
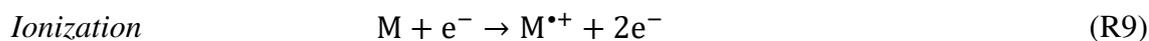


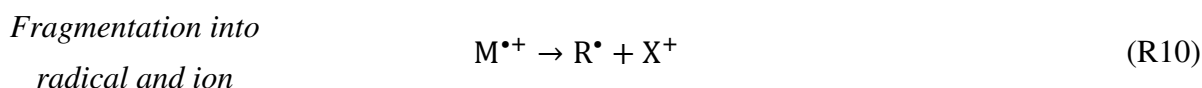
Fig. 22: Schematics of an electron-ionization source [122].

The voltage difference between the filament and the associated anode is typically variable between 5 and 85 V, i.e., the electrons can have energies up to 85 eV. Because molecules can fragment due to excess energy, usually the selected electron acceleration energy is set to below 70 eV. If an electron collides with a test molecule M , the impact energy is absorbed and

during the collision typically one electron (not very often two or even three electrons) is released from the molecule. This results the formation of a positively-charged molecular radical ion $M^{\bullet+}$ (cation):



The ionization energy of most organic molecules lies between 6 and 13 eV (e.g., toluene 8.8 eV and naphthalene 8.1 eV [123]). Therefore, the electrons with 70 eV have a large excess energy. It can therefore happen that the molecular ion ($M^{\bullet+}$) dissociates into a radical and an ion or into a neutral fragment (molecule) and an ion.



Since the fragment ions are highly excited, they can react further inside the ion source. The resulting charged and neutral fragments can contribute to the structural clarification, because they indicate possible structural motifs in the molecule.

In TOF-MS, the potential energy difference between ion source and analyzer field accelerates the produced ions and pulls them out from the ion source. An ion pulse is sent through the field free flight tube and the mass to charge ratio is determined by measuring the flight time t_f of the ions. All ions from each ion pulse receive the same kinetic energy and begin their travel at the same time; the heavier ions are therefore slower and arrive later at the detector than lighter ones. Depending on the type of the device, different acceleration voltages (U) can be used. During the acceleration, the potential energy of the ions is completely converted into kinetic energy; accordingly, the velocity of the ions follows:

$$E_p = E_k \quad (31)$$

$$zeU = \frac{1}{2}mv^2 \quad (32)$$

$$v = \sqrt{\frac{2zeU}{m}} \quad (33)$$

Therefore, the velocity v of the ions at a given acceleration voltage U obviously depends on their mass m and their number of charges z . Here, E_p is the potential energy, E_k is the kinetic energy and e is the electron charge. If the ions fly over a sufficiently long distance d in the field-free flight tube, they hit the detector after the flight time t_f . The heavier ones reach the detector later than the lighter ones, as a transformation of Eq. 33 shows.

$$t_f = \frac{d}{v} \quad (34)$$

$$t_f = \frac{d}{\sqrt{2eU}} \sqrt{\frac{m}{z}} \quad (35)$$

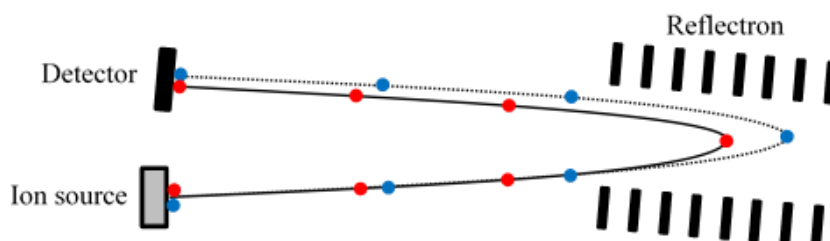


Fig. 23: Schematics of a reflectron TOF-MS [121, 122]. Blue: ions of a given mass with correct kinetic energy; red: ions of the same mass but with lower kinetic energy (because of ionization at a different location in the ion source). With the reflectron, ions with the same mass but different kinetic energy (velocity) arrive at the detector simultaneously because of the different compensating time they spend in the reflectron.

With this method, all generated ions are detected, therefore, the detection sensitivity is very high. The resolution, however, is generally moderate with the linear TOF-MS arrangement of ionization source, detector, acceleration, and drift path. The resolution can be increased with an additional reflectron (an electrostatic reflector), which is situated at the end of the flight tube opposed to the ion source (Fig. 23). The reflectron is applied as an ion mirror and extends thus the flight distance of the ions by deflecting the ions and sending them back through the flight tube. The reflectron also focusses the trajectories of the ions into one pulse. In addition, it corrects the energy dispersion of ions with the same m/z since ions with more kinetic energy (higher velocity) penetrate further down into the reflectron and require therefore more time to leave the reflectron. Consequently, faster ions, i.e., ions with higher kinetic energies travel a longer flight path and will arrive at the detector at the same time than slower (less energetic) ions with the same m/z .

In this work, for kinetic measurements of anisole and its reaction products behind shock waves, a HRR-TOF-MS (Kaesdorf) was used. Figure 24 illustrates the geometry of the TOF-MS connected to the shock tube. Coupling of a TOF-MS to a shock tube requires a very high repetition rate in order to record entire mass spectrum over the mass range of interest within a few microseconds. The TOF-MS was operated in reflectron mode (see above) with the flight path of 40 cm. It has an electron ionization source that can be operated at a maximum pulse repetition frequency of 150 kHz. Within the scope of the present work, the measurements were carried out with a pulse frequency of 100 kHz that results in a fundamental time resolution of 10 μ s for measuring one individual mass spectrum. The maximum time resolution generally results from the flight time of the heaviest species that are detectable to avoid overlap with the light species of the subsequent experiment.

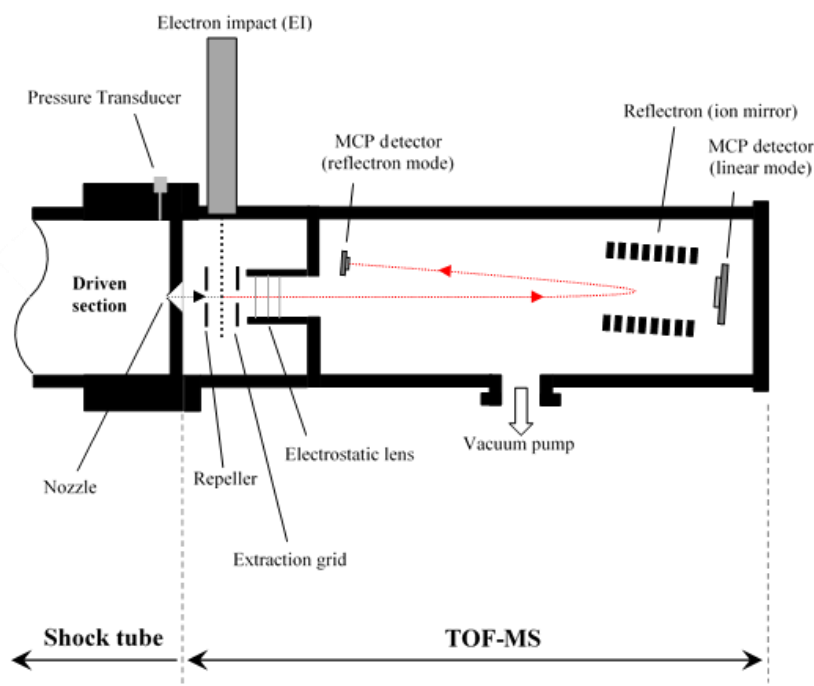


Fig. 24: Schematics of the TOF-MS at the shock tube [121].

The vacuum chamber of the ion source is connected to the drift tube of the mass spectrometer via a circular pinhole (3 mm diameter). The ion source and mass spectrometer are vacuumed using turbomolecular pumps to the pressures better than 4×10^{-7} mbar. The extent of fragmentation rises with increasing electron energy in the ion source. However, in this case the number of the formed ions and thus the sensitivity also increases and therefore an appropriate compromise between sensitivity and fragmentation should be found for the measurements. In this construction, a nozzle (45 or 60 μm) is placed at the end plate of the shock tube (TOF-MS inlet) to form a free gas jet in the direction of the mass spectrometer. The sampling process through a nozzle in interaction with a shock wave strongly depends on the geometry of the nozzle, the pressure in the driven section of the shock tube, and the pressure in the vacuum chamber of mass spectrometer. The detected signals also depend on the structure of the TOF-MS, namely volume, distance of the nozzle and ion source, angle of the gas jet and mass spectrometer and also the thermal boundary layer. Molecular-beam sampling (MBS) has previously been investigated by several studies [124-126]. Timing and triggering during each experiment are achieved by a pulse delay generator PC card (BME03). Synchronization of the TOF operation, its shut-off system, and the data acquisition is accomplished using a combination of a control device and a TTL pulse generator (model TGP 110) with the shock event at the last pressure transducer near the end flange. Complete and detailed description about the calibration and the data acquisition system can be found in Ref. [121].

5. Results and Discussion: Characterization of Selected Tracers

This chapter mainly represents the contents of the peer-reviewed publications on toluene, anisole and acetylene (cf. references 1, 2 and 3 in section 9 list of own publications). In addition, results on optical properties and pyrolysis of p-XL and 1,2,4-TMB are described.

5.1. Toluene

UV absorption spectra of toluene and its decomposition products were measured as a function of reaction time behind reflected shock waves. These measurements were compared to and interpreted based on simulations using two reaction kinetics models for toluene pyrolysis – the mechanism of Oehlschlaeger et al. [66] and the recently published mechanism of Yuan et al. [127, 128] – and high-temperature absorption cross-sections of reaction products and intermediates from Ref. [66]. In addition, the fluorescence properties of toluene and of the reacting mixture using 266 nm laser excitation was investigated during pyrolysis at selected reaction times and various temperatures.

5.1.1. Absorption measurements

Temperature dependence of the absorption cross-section

Time-resolved UV absorption spectra of shock-heated toluene diluted in argon were measured for temperatures between 810 and 1755 K at pressures of 1.5 and 2.1 bar. Absorption spectra were acquired in the 220–300 nm wavelength range with a spectral resolution of 5 nm. Figure 25 shows absorption spectra at elevated temperatures between 298 and 1140 K, where decomposition of toluene is negligible on the experimental time scale [129]. At room temperature, the spectrum peaks at ~258 nm with $\sigma_{258\text{ nm}}(298\text{ K}) = 4.3 \times 10^{-19}\text{ cm}^2$ and a full width at half maximum (FWHM) of ~25 nm. This spectral feature is caused by the $S_0 \rightarrow S_1$ transition. The room-temperature absorption measurements (taken at 150 mbar) agree well with results from previous studies [12, 130]. The strong $S_0 \rightarrow S_2$ transition on the blue side of the spectrum at room temperature indicates a significant red shift with temperature and overlaps with the $S_0 - S_1$ transition at high temperatures [12]. The entire spectra (230–300 nm) also show a red shift with increasing temperature, plus an increase in the total absorption.

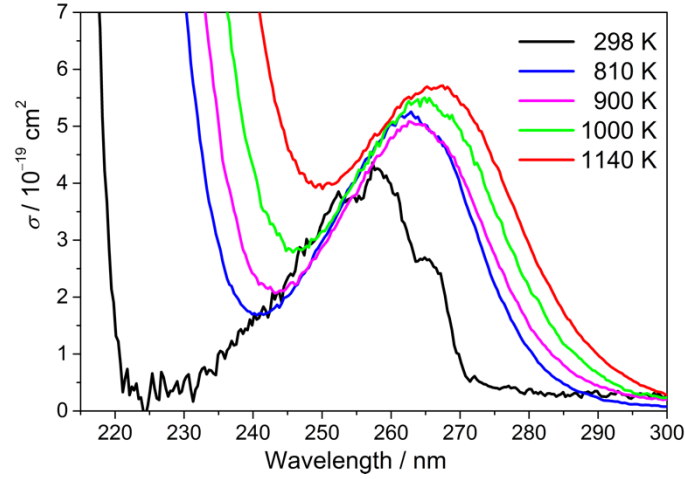


Fig. 25: Absorption spectra of a 2% mixture of toluene in Ar at room temperature (150 mbar) and at higher temperatures (1.2 bar) according to Eq. 4.

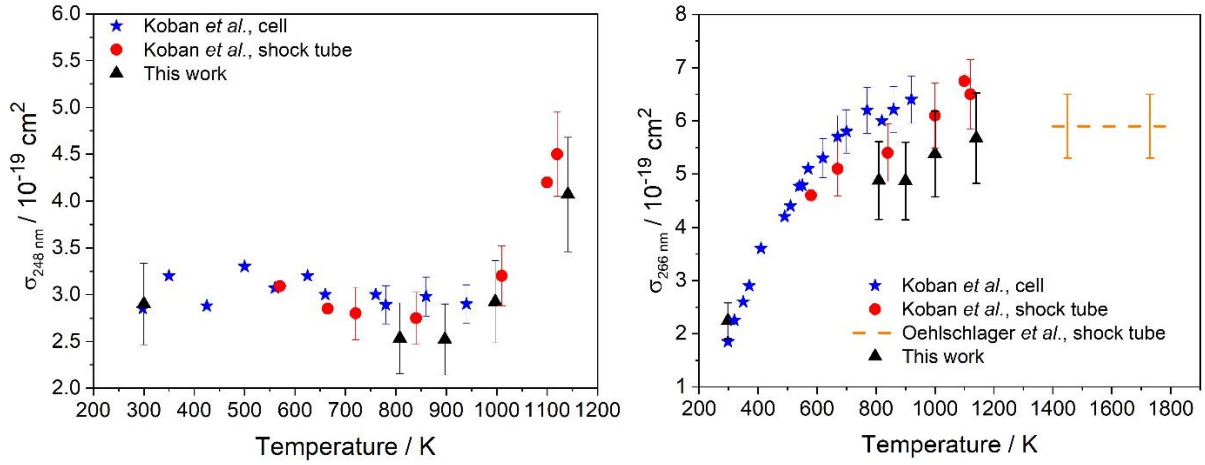


Fig. 26: Absorption cross-sections of toluene at 248 nm (left panel) and 266 nm (right panel) as a function of temperature compared to literature values of Koban et al. [12] and Oehlschlaeger et al. [66]. The determined uncertainty of 15% is shown as error bars.

Because fluorescence is often excited with standard UV laser sources such as excimer or frequency-quadrupled Nd:YAG lasers, the absorption cross-sections are plotted at 248 and 266 nm as a function of temperature in Fig. 26. At 248 nm, the absorption cross-section is approximately independent of temperature up to 1000 K and is mostly due to the $S_0 \rightarrow S_1$ transition. Above this temperature, the absorption cross-section at 248 nm increases with temperature. This growth can be explained by an additional contribution of the $S_0 \rightarrow S_2$ absorption feature [12], which is accessible due to the increased thermal population of higher vibrational levels in the ground state from where absorption starts. In contrast, the absorption cross-section at 266 nm (right plot in Fig. 26) increases monotonically with temperature up to ~ 1100 K. The absorption cross-section at 266 nm is $\sigma_{266 \text{ nm}} = (5.7 \pm 0.9) \times 10^{-19} \text{ cm}^2$. This is the upper limit of the determination range, before the onset of toluene decomposition. This value is consistent with observations from Oehlschlaeger et al. [66] at higher temperatures. They found a temperature-independent value $\sigma_{266 \text{ nm}} = (5.9 \pm 0.6) \times 10^{-19} \text{ cm}^2$ between 1400 and 1780 K. Considering the spectral resolution of ~ 5 nm in this study, the obtained cross-sections

are globally somewhat lower but in reasonable agreement with existing literature values (squares and circles) in the same temperature range [12].

Interference of the pyrolysis on absorption

Figure 27 shows the effective absorption cross-sections σ_{eff} at 266 nm at various reaction times after the arrival of the reflected shock wave. σ_{eff} is defined as the cross-section of the mixture based on the initial concentration of toluene and the intermediates and products formed after arrival of the reflected shock wave (see Eq. 29). Below ~ 1200 K, σ_{eff} is constant during the reaction time and can be assigned to toluene [131]. At 1300 K and above, σ_{eff} increases with reaction time. Because the absorption cross-section of toluene at 266 nm is independent of temperature between 1400–1700 K (as measured immediately after the shock arrival before the onset of pyrolysis in Ref. [66]), this result indicates that pyrolysis of toluene becomes significant and that the products formed are stronger absorbers than toluene. These measurements represent a benchmark for how much the apparent absorption cross-section can change in a temperature range not investigated so far.

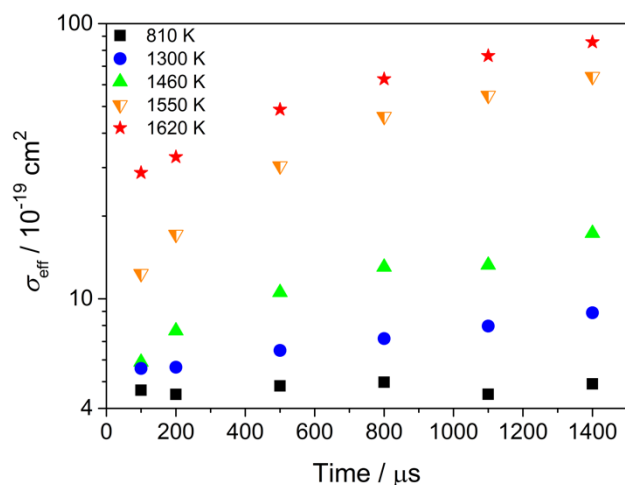


Fig. 27: Measured effective absorption cross-sections σ_{eff} of toluene and its decomposition products at 266 nm as a function of time after arrival of the reflected shock wave.

To gain a better understanding, which reaction products are responsible for the increase of the (time-dependent) effective absorption at temperature above, simulations of the chemical kinetics are accomplished for 1550 K (0.1% toluene, 2.0 bar), 1620 K (0.1% toluene, 2.1 bar), and 1755 K (0.2% toluene, 2.1 bar) under adiabatic conditions. Firstly, the mechanism of Oehlschlaeger et al. [66] is applied. Under their experimental conditions (employing a factor of 5–10 lower toluene concentrations than in this work), Oehlschlaeger et al. could successfully simulate their observed fractional absorption at 266 nm at early reaction times considering time-dependent contributions of toluene, benzyl radicals, and decomposition products of the benzyl radicals (denoted as C_7H_6). Using the absorption cross-sections and the simulated time-dependent concentrations of these respective species, fractional absorption can be derived as follows:

$$\frac{I_0(\lambda) - I(\lambda, t)}{I_0(\lambda)} = 1 - (\exp(-l(\sigma_{\text{toluene}}c_{\text{toluene}} + \sigma_{\text{benzyl}}c_{\text{benzyl}} + \sigma_{\text{C}_7\text{H}_6}c_{\text{C}_7\text{H}_6}))) \quad (36)$$

To analyze the fractional absorption in this study, the absorption caused by these species was subsequently considered and temperature-independent absorption cross-sections at 266 nm from Ref. [66] were used i.e., $\sigma_{\text{toluene}} = 5.9 \times 10^{-19} \text{ cm}^2$, $\sigma_{\text{benzyl}} = 1.9 \times 10^{-17} \text{ cm}^2$, and $\sigma_{\text{C}_7\text{H}_6} = 3.4 \times 10^{-18} \text{ cm}^2$. Derudi et al. [64] found that benzyl decomposes to o-benzyne (o-C₆H₄) + CH₃ and fulvenallene (C₇H₆) + H with a ~ 1:1 branching ratio, both fulvenallene and o-benzyne likely contribute to the absorption from (a) product(s) of benzyl decomposition observed by Oehlschlaeger et al.

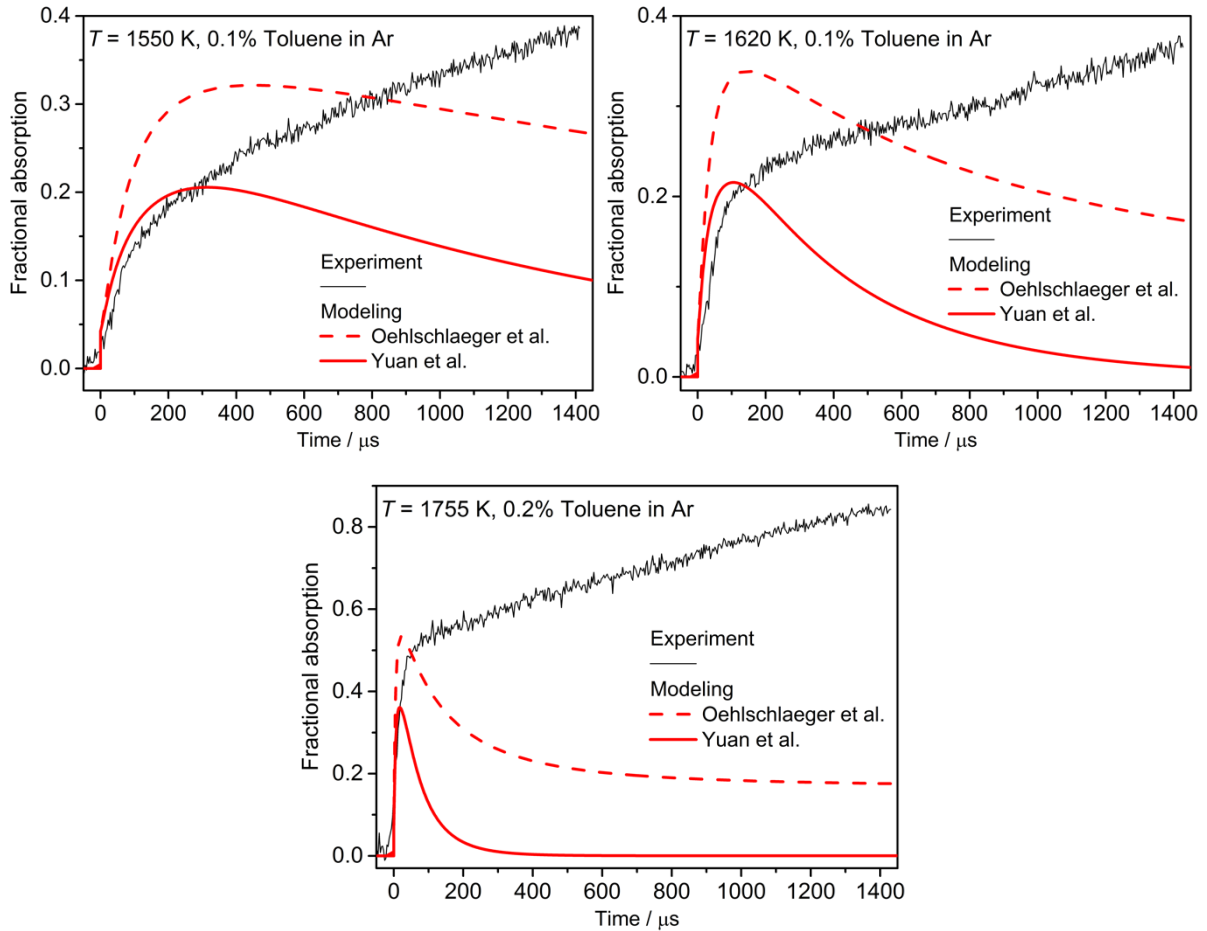


Fig. 28: Comparison of the measured fractional absorption with model predictions based on the mechanisms of Oehlschlaeger et al. [66] and Yuan et al. [127, 128] considering contributions to the absorption from toluene, benzyl, and C₇H₆ according to Eq. 36.

The results are shown in Fig. 28. Before arrival of the reflected shock wave (i.e., at $t < 0$), absorption by toluene is negligible compared to the absorption after the shock wave (also because of the lower total gas density at that time). Benzyl has a strong broadband absorption in the 245–275 nm range [132, 133] and a factor of ~ 30 higher cross-section at 266 nm than toluene in the given temperature range. Due to the formation of benzyl radicals after the passage of the reflected shock wave, the absorption increases more strongly. The mechanism of Oehlschlaeger et al. qualitatively describes the experimentally observed initial rise in the frac-

tional absorption, but it overpredicts the experimental results after the steep initial rise. This overestimation indicates a too high benzyl concentration predicted by their model. The model predicts a decreasing fractional absorption towards later times due to consumption of benzyl radicals, whereas the experimental absorption keeps increasing. This discrepancy is a strong indication of absorption of additional intermediates and/or products formed during toluene pyrolysis forming later in the reaction process, which are not considered in Eq. 36. In our context, this initial phase that hints towards decomposition of the tracer and initially formed products is also considered more relevant for the practical spectroscopic application than later reactions that presumably lead towards the build-up of larger reaction products and ultimately, soot.

The fractional absorption experiments were additionally simulated based on the recently published toluene pyrolysis and oxidation mechanism of Yuan et al. [127, 128]. The latter contains a more comprehensive set of secondary reactions and has been validated towards a wide variety of experimental targets, overall showing remarkable performance. At all three temperatures considered the magnitude of the initial rise predicted by the mechanism of Yuan et al. is consistent with the experimental results (cf. Fig. 28). Similar to the simulations of Oehlschlaeger et al., the absorption simulated based on the mechanism of Yuan et al. underpredicts the measured profiles at later reaction times, which, again, is an indication of absorption of additional species not considered in Eq. 36. Note that the intention of this study is to clarify the initial step of the decomposition which is highly relevant for diagnostics applications. Secondary reactions that cause an additional increase of absorption through the formation of larger molecules and finally soot are not in the focus. The faster decrease in the model of Yuan et al. compared to the model of Oehlschlaeger et al. is caused by a more rapid consumption of benzyl radicals. At all three temperatures, both models show a faster rise than is observed experimentally. This effect might be caused by the limited time resolution of the detection system ($\sim 20\text{--}40\ \mu\text{s}$ under operating conditions).

Figure 29 shows the predicted time temporal concentration profiles at three considered temperatures based on the mechanism of Yuan et al. For clarity, only species with a maximum concentration of 3% relative to the initial toluene concentration are plotted. At all three temperatures, the peak concentration of phenyl radicals is more than an order of magnitude less than that of benzyl, although at higher temperatures both radicals are formed in similar amounts (with a preference for benzyl with branching ratio 90:10 at 1000 K and 60:40 at 2000 K [64]) from the initial unimolecular decomposition of toluene via R4 and R5 [65, 66] (cf. Sec. 2.1). This result is consistent with phenyl radicals being more reactive than benzyl radicals and justifies that phenyl has not been considered in Eq. 36. Due to the small absorption cross-section of benzene ($\sim 2 \times 10^{-20}\ \text{cm}^2$ at 266 nm [66]), neglecting its contributions to the observed fractional absorption is justified as well.

According to Fig. 29, the model predicts substantial formation of acetylene (C_2H_2) and polyacetylenes (C_4H_2 and C_6H_2), the formation of the latter becoming more prominent with in-

creasing temperature. However, the UV absorption cross-sections of polyacetylenes at high temperature have not been reported in literature. Whereas C_2H_2 does not absorb at 266 nm at room temperature, it absorbs at 266 nm at temperatures higher than 900 K (cf. Sec. 5.4.1). Similar to benzene, contributions of C_2H_2 to the overall observed fractional absorption is insignificant. C_4H_2 and C_6H_2 absorb at 266 nm already at room temperature ($\sigma_{C_4H_2}(293\text{ K}) \sim 2 \times 10^{-20} \text{ cm}^2$ [134] (using the value reported at 264 nm, the upper wavelength range of their study) and $\sigma_{C_6H_2}(293\text{ K}) = 2.1 \times 10^{-19} \text{ cm}^2$ [135]) and might show even stronger absorption at higher temperature, assuming a red-shift of the absorption band located at lower wavelength (264 nm) [134, 135] with increasing temperature.

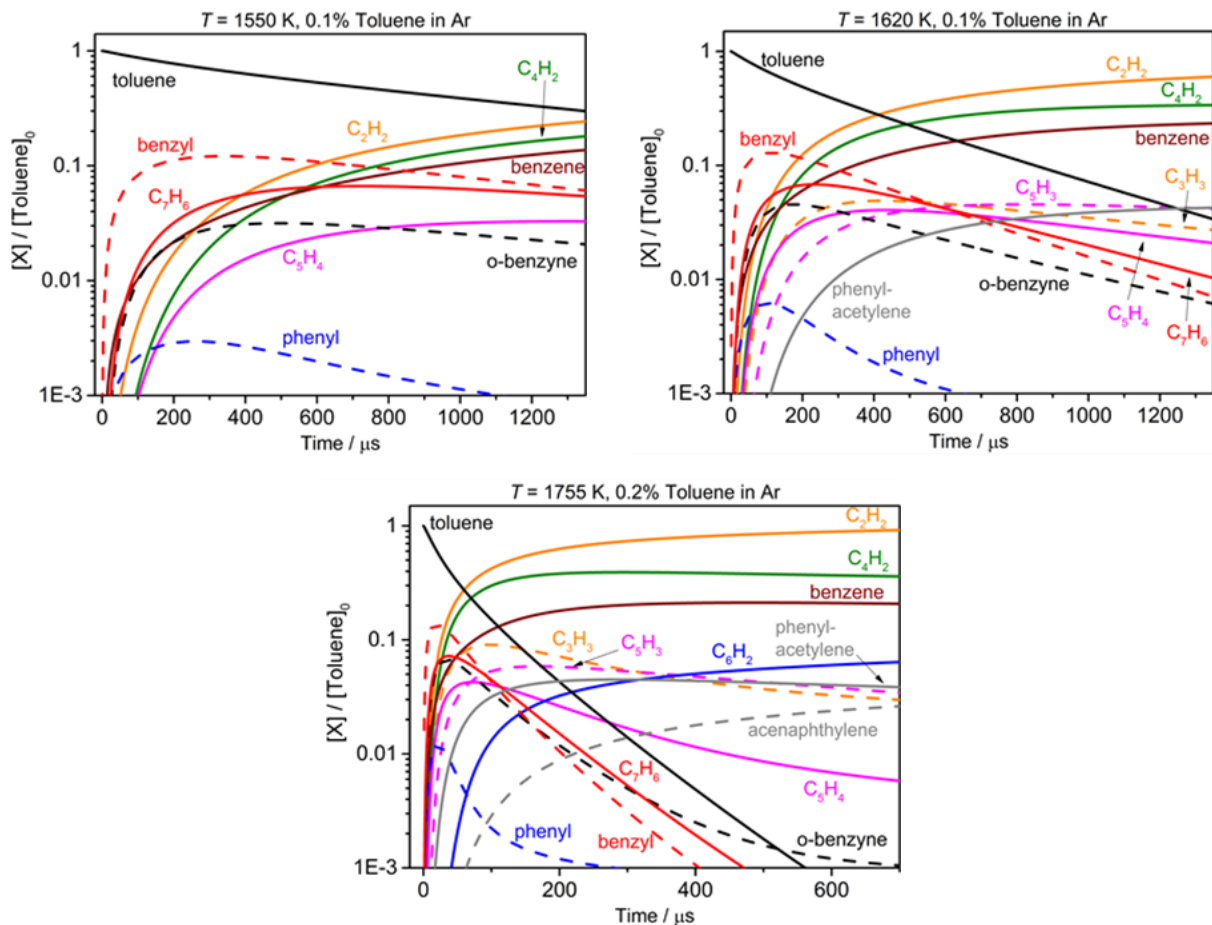


Fig. 29: Simulated concentration-time profiles for the three experiments shown in Fig. 28, based on the mechanism of Yuan et al. [127, 128]. Only species with a maximum concentration above 3% relative to the initial toluene concentration at $t = 0$ are shown for clarity. H_2 , CH_3 , and CH_4 are also not plotted for clarity, although, except for CH_3 at 1550 K, their concentrations exceed 3%. C_7H_6 represents fulvenallene.

Previous studies have investigated the decomposition pathways of toluene and the growth of polycyclic aromatics using mass spectroscopy and gas chromatography [129, 136, 137]. These studies disclosed the formation of various aromatic species, e.g., benzene, naphthalene, indene, phenylacetylene, biphenyl, dibenzyl, acenaphthylene, and fluorene. Simulations based on the mechanism of Yuan et al. [127, 128] predicts formation of phenylacetylene and acenaphthylene in significant amounts towards the higher temperature end.

In order to adequately describe the fractional absorption during toluene decomposition at high temperature, the absorption of polyacetylenes, substituted and polycyclic aromatics, and potentially of soot formed via subsequent reactions would also need to be considered. Spectroscopic information of these species at high temperature is mostly not available or limited to conditions near room temperature [138-140]. Studying the subsequent reactions toward soot, however, is not in the scope of this study that aims to understand the decomposition of tracers and the initial formation of spectrally interfering species.

5.1.2. LIF measurements

Temperature dependence of LIF spectra

LIF spectra of toluene were measured as a function of temperature (865–1750 K) upon 266 nm excitation at total pressures near 1 and 3 bar in a bath gas of argon. Figure 30 shows LIF spectra recorded at 110 μ s after passage of the reflected shock wave as a function of temperature. At 865 K, toluene exhibits LIF signal in the 270–320 nm wavelength range with a peak at around 290 nm. With increasing temperature, the LIF spectrum of toluene shifts to the red and becomes spectrally broader. Moreover, the fluorescence intensity decreases rapidly as a result of the decreasing fluorescence quantum yield.

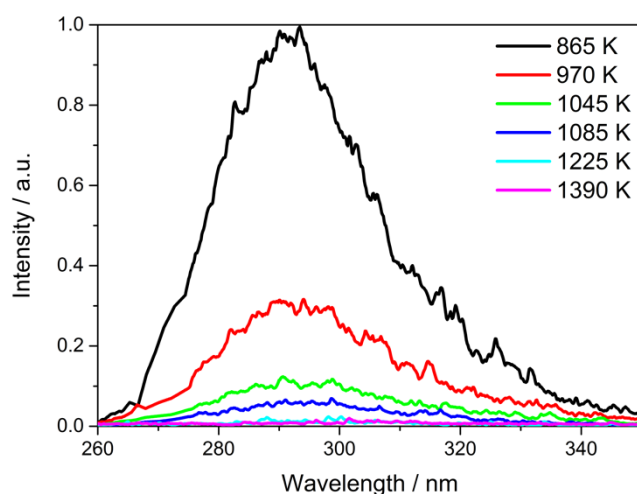


Fig. 30: Single-shot LIF emission spectra of toluene after excitation at 266 nm as a function of temperature at a pressure of 1.2 bar measured at 110 μ s after the arrival of the reflected shock wave.

Between 865 and 1225 K, the fluorescence maximum shows a slight red-shift of about 2 nm per 100 K that follows the trend for lower temperatures reported earlier [11, 12]. The results are shown in Fig. 31. To better visualize the spectral variation of the LIF of toluene and of possible decomposition products towards higher temperature, the spectra were smoothed by an FFT filter [141] with a window size of 7 nm and normalized to their respective peak intensities. A significant red-shift of the spectra occurs between 1225 and 1390 K indicating that newly formed pyrolysis products contribute to the observed LIF. This observation is qualitatively consistent with increase in the effective absorption cross-section at 266 nm (Fig. 27).

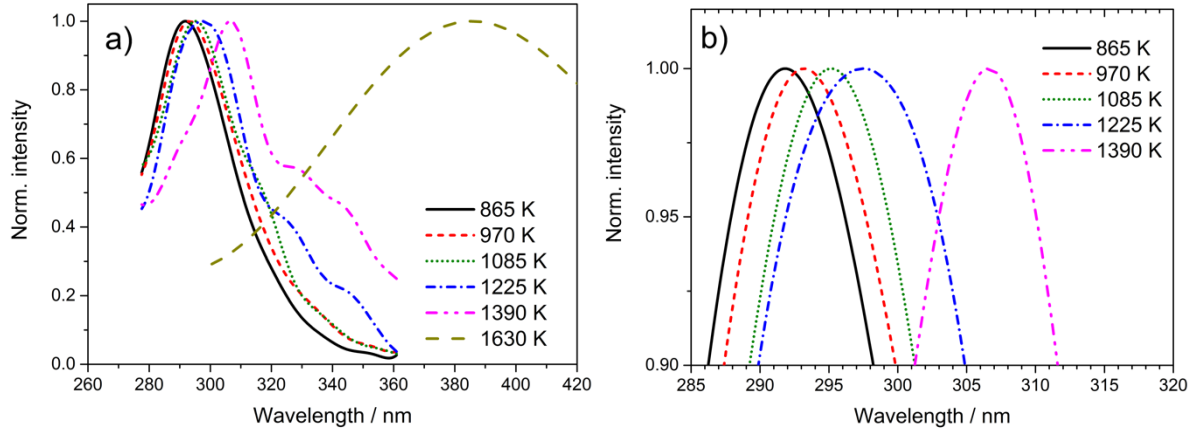


Fig. 31: Smoothed and normalized LIF emission spectra after excitation at 266 nm (see text for details on the smoothing procedure). The spectra from 865–1390 K are the smoothed versions of the data from Fig. 30, taken after excitation at 110 μ s after arrival of the reflected shock wave. The spectrum at 1630 K was taken after excitation at 160 μ s after the reflected shock wave (cf. Fig. 35). a) full spectra, b) zoomed-in version of the 865–1390 K spectra highlighting the red shift in the peak maxima.

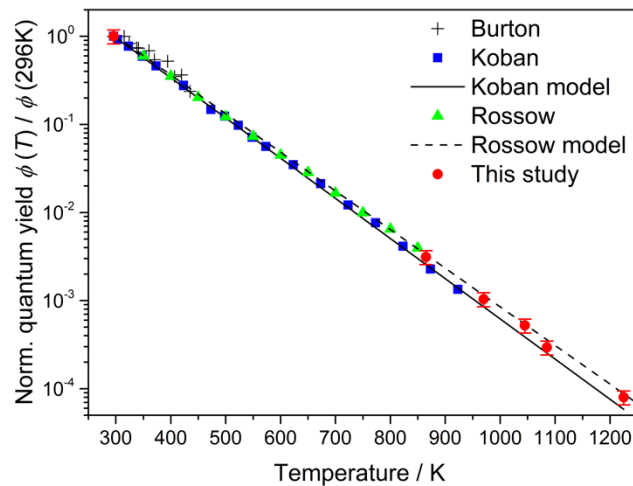


Fig. 32: Relative fluorescence quantum yield of toluene as a function of temperature. Results from the present work (red symbols) are compared with previous data from Burton et al. [130], Koban et al. [12], and Rossow [40].

Relative fluorescence quantum yield

Figure 32 shows the relative fluorescence quantum yield of toluene calculated from the measured fluorescence intensities and the absorption cross-sections from Fig. 25 (cf. Sec. 2.1.4.1). These data extend the temperature range experimentally studied so far and can aid the development of parametric models to predict the fluorescence quantum yield. The model of Koban et al. [12] was developed from data obtained in flow-cell experiments in a bath of N_2 at total pressures of 1 bar. According to this model, the fluorescence quantum yield of toluene decreases by three orders of magnitude when increasing the temperature from room temperature up to about 950 K. Extrapolations to higher temperatures based on this model underpredict the measured absolute values by $\sim 20\%$. In contrast, extrapolations based on the single exponen-

tial fluorescence decay approximation by Rossow [40] overestimate the measured data by $\sim 10\%$. Considering the determined error of $\pm 18\%$ of the fluorescence quantum yield, both models are in satisfactory agreement with the results presented here.

Interference of the pyrolysis on LIF signal

As has been shown above, both the shape of the spectra and the position of the emission maximum change significantly with decomposition of toluene (Fig. 31). Figure 33 shows LIF spectra from experiments at 1630 and 1750 K. The emission spectrum of pure toluene (1225 K) disappears completely and new spectral features appear far red-shifted compared to the original toluene spectrum as a result of the built-up of new species. The LIF emission spectrum at $T > 1600$ K exhibits peak intensities comparable to the LIF intensity of toluene at lower temperature. At 1630 K the first strong detectable signal of pyrolysis products shows broadband emission with a peak around 420 nm and a FWHM of 140 nm. At 1750 K, presumably additional pyrolysis products contribute to the LIF signal, whereas at this temperature, the relative signal intensity at lower wavelength decreases due to reaction progress and/or change in the fluorescence quantum yield.

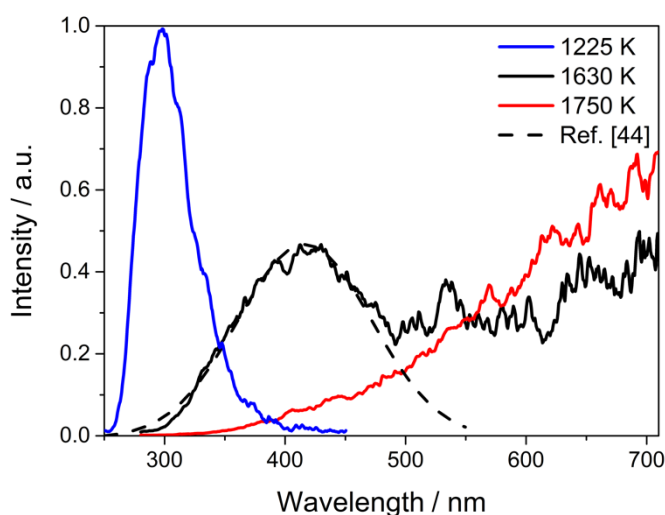


Fig. 33: LIF emission spectra of a mixture of initially 1% toluene in argon at a pressure of 2.9 bar taken after 266 nm laser excitation at 260 μ s after the passage of the reflected shock wave. The dashed line shows a normalized LIF emission spectrum from Sirignano et al. [142].

Sirignano et al. [142] investigated the formation of aromatic species and soot in an atmospheric-pressure counter-flow diffusion flame of ethylene using spectrally- and time-resolved LIF and laser-induced incandescence (LII) measurements employing 266 nm laser light. They found different types of high-molecular mass aromatic compounds. Figure 33 illustrates the fitted LIF emission spectra from Ref. [142] near the stagnation plane where benzene and PAHs have their maximum concentrations. The spectrum shows broad fluorescence emission between 290 and 550 nm which was assigned to both small clusters of PAHs and the formation of higher molecular weight aromatic compounds. For comparison, fluorescence signals of Sirignano et al. [142] and of this study were normalized to their respective peak val-

ues. The good agreement of the spectral shapes suggests the presence of similar species in both studies at the respective conditions.

To identify to which extent phenyl radicals or products from their reactions might contribute to the observed fluorescence signal during toluene pyrolysis at high temperatures, additional experiments were performed using iodobenzene (C_6H_5I). It is known as a clean high-temperature source of phenyl radicals [143, 144]. The black line in Fig. 34 shows the recorded LIF spectrum after decomposition of iodobenzene at 1630 K in comparison with the fluorescence signal during toluene decomposition under comparable conditions. The sharp peak in the iodobenzene spectrum around 340 nm originates from iodine atoms [145], and its width reflects the spectral instrument function. Interestingly, the spectra from both toluene and iodobenzene decomposition show a similar broadband emission feature between ~ 300 – 500 nm. In contrast, the emission at wavelengths above ~ 500 nm observed in the toluene experiment cannot be reproduced in the iodobenzene experiment.

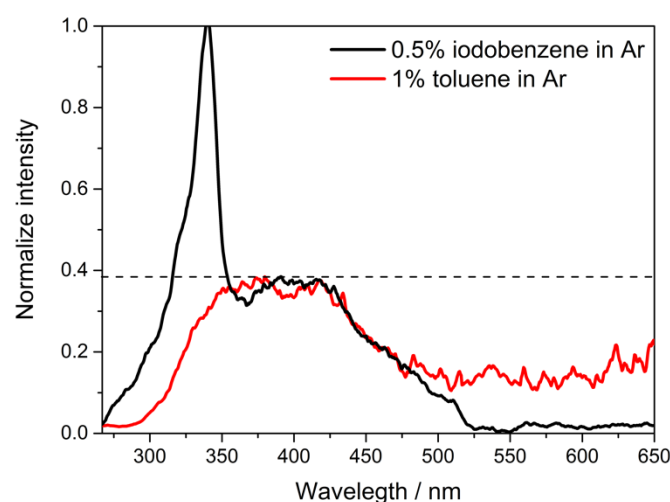


Fig. 34: Comparison of the LIF emission spectra from pyrolysis of iodobenzene and toluene at 1630 K, 160 μs after the passage of the reflected shock wave with 266-nm laser excitation. Total pressures were 1.2 bar (iodobenzene) and 2.9 bar (toluene). For better comparison both spectra are normalized to the maximum of the broadband emission feature.

Further experiments have been done to determine the influence of toluene decomposition and formation of pyrolysis products on the LIF signal at a constant temperature (1630 K) and different reaction times (160, 260, 560, and 860 μs) after the reflected shock wave. The results are shown in Fig. 35. At 160 μs , emission was observed with a peak around 375 nm and a FWHM of 135 nm. At 260 μs , the emission shifts to the red, and broadens towards longer reaction times (560 and 860 μs). This behavior suggests that the fluorescence emission is a superposition from several species, such as various single- or polyaromatic hydrocarbons. It may be speculated that this signal is mostly caused by larger PAH molecules. The shape of the spectrum taken at 860 μs suggests that at least a part of the emission is caused by black-body radiation originating from incandescence of soot particles. Sirignano et al. [142] verified that at longer wavelengths (>500 nm) their spectrum maximizes due to the incandescence emission of solid particles. It should be kept in mind that some of the aromatic molecules like

indene and phenylacetylene discussed above (Sec. 5.1.1) are soot precursors [129]. These species are formed behind reflected shock waves, according to the mechanism published by Zhang et al. [146] and Matsugi et al. [63], and as predicted by simulations based on the mechanism of Yuan et al. [127, 128].

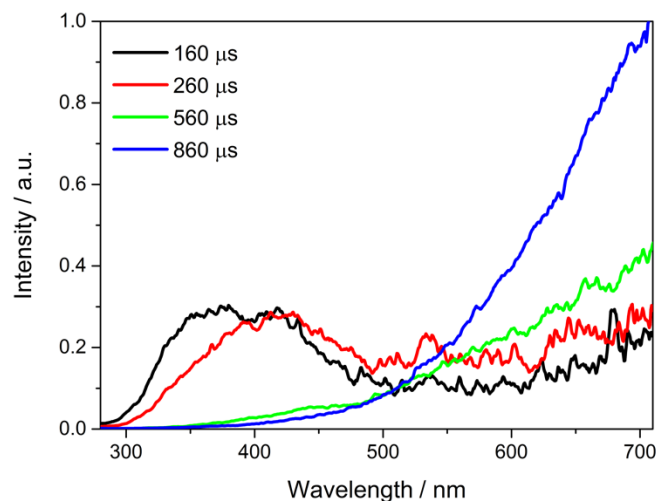


Fig. 35: Laser-induced emission spectra of pyrolysis products after thermal decomposition of 1% toluene in Ar at 1630 K and a total pressure of 2.9 bar and various delay times after the passage of the reflected shock wave with 266-nm excitation.

5.1.3. Conclusions

Time-resolved UV-absorption and single-shot LIF spectra of toluene and its decomposition products were recorded behind reflected shock waves over a wide temperature range (810–1755 K) and near atmospheric pressures (1.2–2.9 bar). In the absorption experiments up to 1140 K, where toluene is stable within the test time, the width of the absorption spectrum increased and showed a slight red-shift as a function of temperature. Because of rapid formation of benzyl radicals from decomposition of toluene at higher temperatures combined with their large UV absorption cross-section, a pronounced early-time increase in the fractional absorption was observed. Modeling using chemical kinetics mechanisms for toluene pyrolysis from the literature [66, 127, 128] and the high-temperature absorption cross-sections of toluene, benzyl, and C_7H_6 as a product from benzyl decomposition predicted the early-time increase reasonably well but significantly underestimated the experimental absorption towards later times. This discrepancy suggests additional absorption of intermediates and products under pyrolytic conditions.

The LIF emission spectra upon 266-nm excitation taken between 865 and 1225 K showed a red-shift of the peak signal of ~ 2 nm per 100 K and a decreasing intensity with temperature. This decrease is caused by a decreasing fluorescence quantum yield of toluene with temperature. Relative fluorescence quantum yields were determined between 865 and 1225 K, increasing the upper temperature limit by ~ 300 K compared to literature measurements. Measurements show that the dependence of the fluorescence quantum yield on temperature remains single-exponential up to at least 1225 K. This result is consistent with literature measurements

taken at lower temperature and confirms predictions of parametric models [12, 40]. Above 1300 K, the LIF spectra showed a significant red shift. Above 1600 K a strong signal increase was observed, with the signal being orders of magnitude stronger than the nascent toluene fluorescence expected in the same temperature range by extrapolation of the temperature-dependent fluorescence cross-section. Both effects are presumably from contribution of species of the pyrolysis process.

5.2. Anisole

Temporally- and spectrally-resolved UV absorption measurements were performed before and during anisole pyrolysis behind reflected shock waves. Additionally, fluorescence spectra of anisole and its pyrolysis products are measured at various temperatures with 266-nm laser excitation. To provide a better insight into the stability and pyrolysis kinetics of anisole and to identify relevant decomposition products, time-resolved multispecies measurements using HRR-TOF-MS behind reflected shock waves were additionally carried out and compared with the results of two detailed kinetics models. The work in this section has been published in peer-reviewed publication 2 (cf. list of own publications).

5.2.1. Absorption measurements

Temperature dependence of absorption cross-section

UV absorption spectra of anisole were measured behind reflected shock waves at temperatures between 565 and 1450 K at pressures of 1.5 and 2.9 bar. Room-temperature spectra were measured prior to arrival of the shock wave at 120 mbar. At $T < 1000$ K, where decomposition of anisole is not expected on the experimental timescale (1.2 ms), absorption spectra were integrated over the entire test time and absorption cross-section of anisole was determined from Eq. 4.

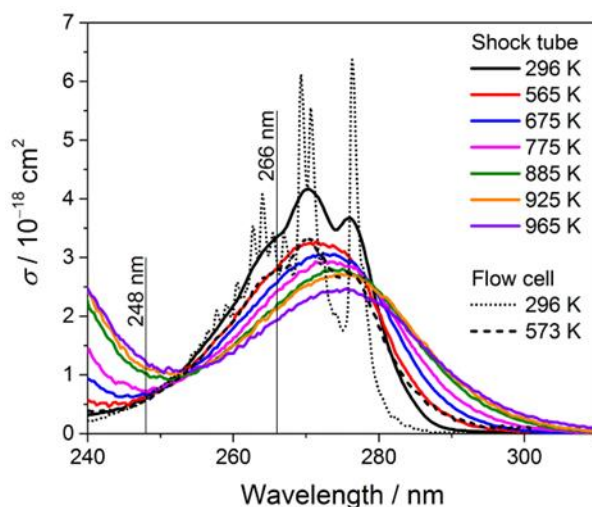


Fig. 36: Absorption cross-section of anisole measured in a mixture of 0.5% anisole in Ar at room temperature at (120 mbar) and at higher temperatures (1.5 bar), with a spectral resolution of ~ 7 nm; Dotted and dashed lines: Anisole (0.33% in Ar) absorption spectra measured with high spectral resolution (~ 0.2 nm) in a flow cell at 296 and 573 K.

Figure 36 shows absorption cross-sections of anisole at 240–310 nm as a function of temperature. Absorption centered at ~ 270 nm is observed resulting from a $\pi\text{-}\pi^*$ ($S_0\text{-}S_1$) transition. With increasing temperature, the absorption peak red-shifts and the spectra broaden. As is the case for toluene [12], the absorption spectra of anisole at room temperature show a fine structure that disappears at higher temperatures. This fine structure is under-resolved (spectral resolution ~ 7 nm) in the low-temperature shock-tube measurements which becomes apparent

from the comparison with highly spectrally-resolved measurements from a flow cell (0.2 nm resolution, dashed and dotted lines in Fig. 36). Comparison of measurements at 573 K in shock tube and flow cell shows that starting from this temperature, the 7-nm resolution is sufficient and that the absolute values of both data sets are in good agreement.

Tran et al. [14] reported $\sigma_{573\text{ K}}$ values of anisole in CO₂ a factor of three lower than here presented results. This discrepancy is attributed to the fact that they generated their mixtures by evaporation and apparently assumed an erroneous room-temperature vapor pressure that is three times above the correct value – thus assuming a threefold number density in their data analysis. Ambrose et al. [147] reported a vapor pressure of 4.72 mbar at 298 K (Faust et al. [13] reported a vapor pressure of 3.6 mbar at 293 K for anisole derived from analogy assumptions being unaware of Ref. [147] that has, however, not influenced their results). In this work, measured room-temperature absorption cross-sections are verified in two independent experiments that did not rely on the saturation vapor pressure. These measurements were carried out (i) under pre-shock conditions in the shock tube (where the mixture is prepared based on the measured partial pressure after evaporation of anisole) and in (ii) flow-cell experiments where the mixture is controlled by mass-flow controllers (such as in Ref. [13]). The good agreement of two independent measurements (Fig. 36) ensures that the values reported here are correct.

Interference of the pyrolysis on absorption

At higher temperatures, the nascent products of anisole decomposition lead to additional absorption. Figure 37 shows the temporal behavior of the effective absorption cross-section (Eq. 29) at ~266 nm for 960–1450 K. If anisole is stable on the experimental time scale, a constant σ_{eff} would result after the arrival of the reflected shock wave at $t = 0$. This is the case for the experiment at 960 K. In the temperature range investigated, increasing the pressure from 1.5 to 2.9 bar has no effect on the broadband absorption spectra.

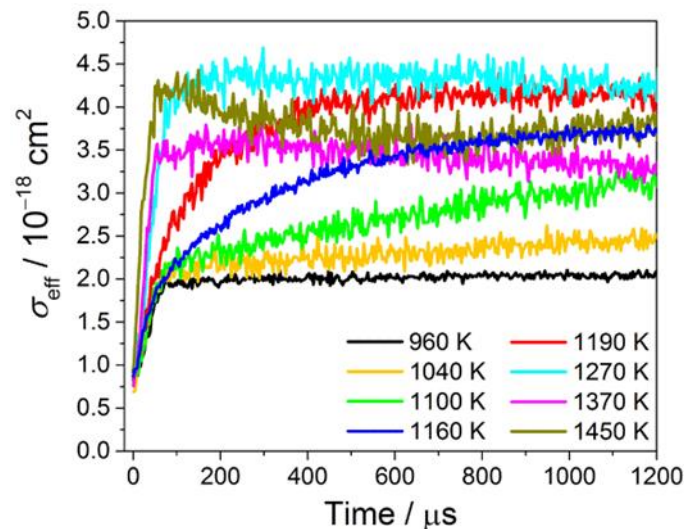


Fig. 37: Effective absorption cross-section σ_{eff} at 266 nm of a mixture initially containing 0.25% anisole in Ar for various temperatures at 2.9 bar as a function of reaction time.

$\sigma_{\text{eff}, 266 \text{ nm}}$ strongly increases with temperature, indicating that the decomposition products absorb UV light more strongly than anisole. This can be clearly seen at 1190 K, where a slow increase in $\sigma_{\text{eff}, 266 \text{ nm}}$ occurs for $\sim 400 \mu\text{s}$. The increase in signal and hence the rate of formation of pyrolysis products becomes larger with increasing temperature. $\sigma_{\text{eff}, 266 \text{ nm}}$, however, seems to reach a plateau at higher temperature and longer reaction times. This behavior suggests that at high temperature and longer reaction time, the apparent signal is a superposition from several species (such as various single- or polyaromatic hydrocarbons) which after the fast and complete decomposition of anisole reach a state with little change in total absorption.

5.2.2. HRR-TOF-MS measurements

HRR-TOF-MS experiments were performed to aid the interpretations in absorption and LIF experiments and to confirm the onset temperature and time of anisole decomposition as well as to validate the intermediate and product formation predicted by detailed kinetics mechanism of Nowakowska et al. [72]. Measurements were carried out at 930–1530 K at 0.88 to 1.67 bar with a mixture of 0.5% anisole and 1% Ar in Ne.

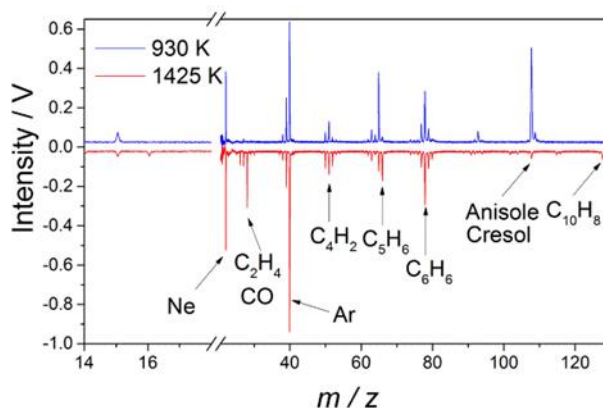


Fig. 38: Mass spectra of anisole pyrolysis integrated over reaction time between 1 and 1.5 ms. Mixtures consisted of 0.5% anisole and 1% Ar in Ne.

Figure 38 shows mass spectra from anisole at 930 K and 1.18 bar, where anisole is stable, and from anisole pyrolysis at 1425 K and 1.6 bar, where most of the anisole is already decomposed. The pattern measured at 930 K shows the fragmentation of anisole through electron ionization generating $\text{C}_6\text{H}_5\text{O}^+$ ($m/z = 93$), C_6H_6^+ ($m/z = 78$), C_5H_5^+ ($m/z = 65$), C_4H_3^+ ($m/z = 51$), and C_3H_3^+ ($m/z = 39$). At 1425 K, the weak signal at $m/z = 108$ (anisole + cresol) indicates that most of the anisole is decomposed after 1 ms. The new masses and the signal increase found on the fragments therefore corresponds to pyrolysis products.

Scheer et al. [73] observed benzene (C_6H_6) and naphthalene (C_{10}H_8) as products from anisole pyrolysis which is consistent with the signals at $m/z = 78$ (C_6H_6) and 128 (C_{10}H_8) in this measurement. While fragmentation from ionization of naphthalene at 70 eV is minor [148], fragmentation of ionized C_6H_6 yields product signals at $m/z = 39, 50, 51, \text{ and } 52$. The signal at $m/z = 66$ (C_5H_6) detected at 1425 K might indicate the formation of cyclopentadiene. The

main species observed during pyrolysis are thus anisole, CO, C₅H₆, C₆H₆, and C₁₀H₈. Due to the limited mass resolution of the TOF-MS, the signal at $m/z = 28$ is the combined signal intensity of C₂H₄ and CO. In these experiments, both have almost the same calibration factor that is required to calculate the concentration from the signal intensity. Therefore, the combined concentration of CO + C₂H₄ can be derived directly from the peak intensity at $m/z = 28$.

Figure 39 shows normalized concentration-time profiles of anisole as a function of temperature. At 930 K, anisole is stable on the experimental timescale. At 1050 K, about 20% decomposes within the test time of 1.4 ms, and at 1530 K, anisole completely decomposes within 200 μ s. These observations are in qualitative agreement with the rate coefficient ($k = 1.2 \times 10^{16} \exp(-275 \text{ kJ/mol}/RT) \text{ s}^{-1}$) reported in Ref. [71] for anisole decomposition at 1000–1580 K resulting in anisole lifetimes of 20 ms at 1000 K and 0.3 μ s at 1500 K. These results corroborate the observation that decomposition of anisole can be neglected in shock-tube experiments below \sim 950 K. Nevertheless, for longer residence times such as in flow cells, decomposition already needs to be accounted for at this temperature.

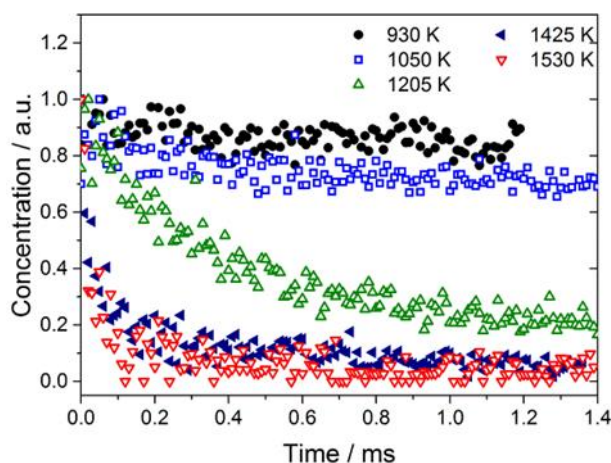


Fig. 39: Concentration-time profiles during anisole pyrolysis (0.5% anisole and 1% Ar in Ne) for selected temperatures.

Simulation of anisole decomposition

Figure 40 shows measured and simulated concentration–time histories of anisole + cresol, C₆H₆, and CO + C₂H₄ based on the mechanisms of Nowakowska et al. [72] and Ranzi et al. [149]. Mole fraction profiles of C₆H₆ were corrected by considering fragmentation of anisole in the ion source of mass spectrometer. Nowakowska et al. studied the detailed kinetics of pyrolysis and stoichiometric oxidation of anisole based on their experiments in a jet-stirred reactor coupled with gas chromatography and mass spectrometry, whereas Ranzi et al. developed a comprehensive kinetics model for hydrocarbon and oxygenated fuels which contains a hierarchical detailed kinetics schemes of anisole pyrolysis and oxidation [70]. Ranzi et al. compared their model predictions with previous measurements in an atmospheric-pressure flow reactor [150]. The profiles of CO+C₂H₄, C₆H₆, and anisole + cresol at 1425 K are well predicted by the Nowakowska mechanism but the Ranzi mechanism does not match the

measurements for $\text{CO}+\text{C}_2\text{H}_4$ and C_6H_6 at this temperature. At 1530 K, the agreement for $\text{CO}+\text{C}_2\text{H}_4$ and C_6H_6 improves and both models correspond closely to the measurements.

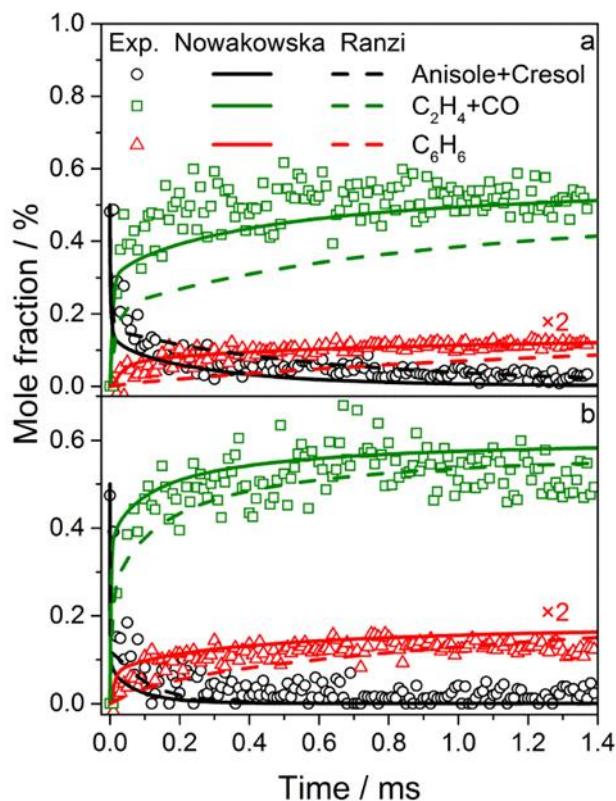


Fig. 40: Measured (symbols) and simulated (lines) concentration–time profiles of some main species during pyrolysis of anisole for a mixture of 0.5% anisole and 1% Ar, in Ne and at two different conditions; (a): $T_5 = 1425 \text{ K}$, $p_5 = 1.60 \text{ bar}$ and (b): $T_5 = 1530 \text{ K}$, $p_5 = 1.47 \text{ bar}$. Simulations based on the models from [72] and [149].

The model of Nowakowska mechanism [72] provides valuable information about stability of anisole under realistic conditions. Figure 41 shows the reaction times needed (as a function of temperature) until 1, 5, and 50% of anisole decompose.

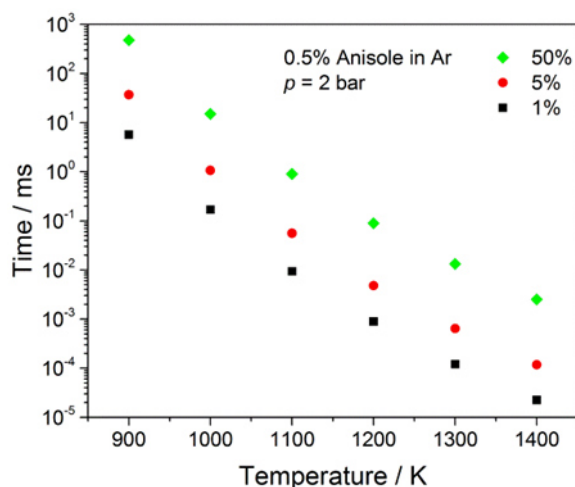


Fig. 41: Time until a certain fraction (1, 5, 50%) of the initial anisole decomposes as a function of temperature.

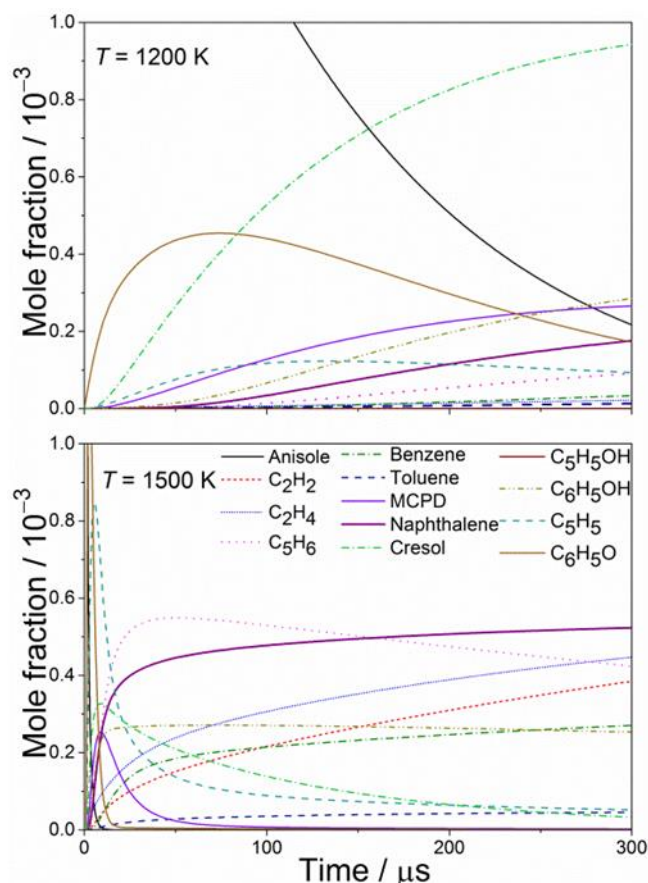


Fig. 42: Species formed from anisole pyrolysis as a function of time at 1200 K and 1500 K for pressure of 1.5 bar.

Figure 42 shows the species formed as a function of time at 1200 and 1500 K. At 1200 K, anisole decomposes within a few microseconds and the model predicts substantial formation of C_6H_5O and cresol, the formation of the latter becoming more prominent at longer reaction time. However, the amount of cresol drops off dramatically at higher temperatures. At 1500 K, almost 25% of the anisole initially present is transformed into naphthalene within less than 100 μs . On the basis of this simulation, effective absorption cross-sections could be calculated if the respective high-temperature absorption cross-sections of the respective species were available. As far as is known, however, this is not the case.

Table 2 summarizes room-temperature 266-nm absorption cross-sections of some of the relevant species only and compares them to the respective value of anisole. These data show that several potential species can contribute to absorption and the rapid rise in effective absorption cross-section (cf. Fig. 37) cannot be attributed to a single species, although the strong absorption cross-section of naphthalene suggests that naphthalene might have a dominant role in the observed increase $\sigma_{\text{eff}, 266 \text{ nm}}$ at higher temperature and longer reaction time. For fluorescence, however, it can be assumed that naphthalene will be a main contributor because (i) the large mole fraction in the product mixture and (ii) the large effective fluorescence yield that at room temperature has been shown to be 40 times higher than that of anisole per molecule [39].

Table 2: Room-temperature absorption cross-sections (266 nm) of some aromatics forming during pyrolysis of anisole.

Compound	Absorption cross-section /cm ²
Anisole	3.35×10^{-18}
Phenoxy radical	2.8×10^{-18} [151]
Phenol	2.49×10^{-18} [152]
<i>o</i> -Cresol	3.92×10^{-18} [153]
<i>p</i> -Cresol	1.91×10^{-18} [153]
<i>m</i> -Cresol	3.03×10^{-18} [153]
Benzene	2.0×10^{-20} [66]
Naphthalene	1.42×10^{-17} [152]

5.2.3. LIF measurements

Temperature dependence of LIF spectra

LIF emission spectra of anisole were measured at 160 μ s after shock heating with 266-nm laser excitation. Figure 43 shows the measured LIF spectra at 575–980 K and 1.5 bar. The LIF intensity decreases by three orders of magnitude between 296 and 980 K. Anisole LIF at room temperature appears in the 270–360-nm wavelength range with a peak at around 290 nm. With increasing temperature, the LIF spectrum broadens and red-shifts by ~ 2.8 nm/100 K which is consistent with previous data at lower temperature (~ 3 nm/100 K in N₂ [13], 2.5 nm/100 K in CO₂ [14]).

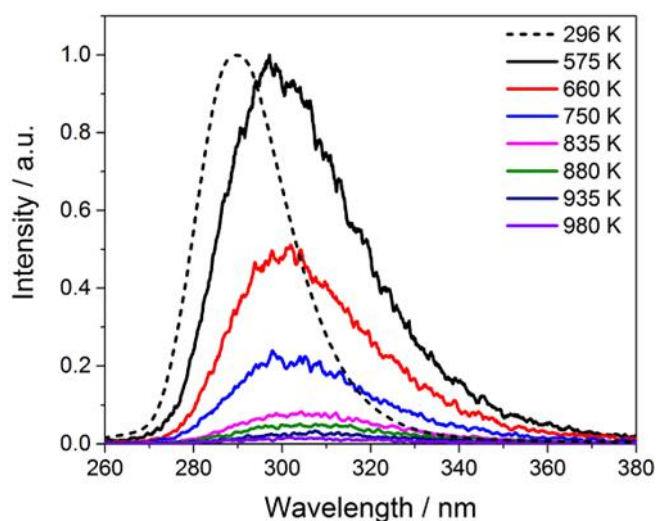


Fig. 43: LIF spectra of anisole (at 1.5 bar, 266-nm excitation, 160 μ s after shock-heating). The spectra for shock-heated gases at $T > 575$ K are normalized to the peak value of the measurement at 575 K. The dashed line (296 K) shows measurements in the shock tube filled under static conditions. Its intensity is divided by a factor

of 18 for better comparison. Signal intensities are corrected for the temperature dependence of the density and therefore represent signals per unit number density.

Relative fluorescence quantum yield

Since the absorption cross-section of anisole at 266 nm only decreases by a factor of two from room temperature to 980 K (Fig. 36), the strong decrease in the LIF intensity is mainly attributed to the T -dependence of the fluorescence quantum yield $\phi_{fl}(T)$ (Fig. 44b). The LIF signals were integrated at 270–360 nm and the relative ϕ_{fl} was calculated from Eq. 7. Figure 44b shows that ϕ_{fl} decreases roughly exponentially by a factor of ~ 450 from 296–980 K which is consistent with previous data [13, 14] also shown in this figure. The values of Ref. [14] were normalized to value at 573 K of this study leading to good overall agreement. While at $T < 773$ K, here presented data agree well with Ref. [13] (normalized to values at 296 K), at higher temperatures ϕ_{fl} are significantly higher than those reported. This discrepancy is attributed to signal interference from pyrolysis products in the flow cell in [13] while these reactions are prevented due to the short residence times in the shock tube. This is consistent with the observation of a significant change in LIF spectra at temperatures above 850 K due to fluorescence from pyrolysis products in [13].

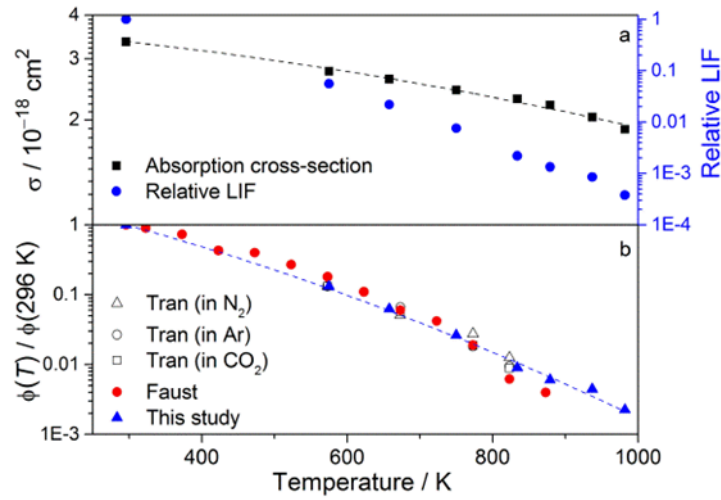


Fig. 44: a: Measured absorption cross-section at 266 nm and relative LIF of anisole as a function of temperature. The dashed line shows the fitted $\sigma_{266 \text{ nm}}(T)$ based on Eq. 37. b: Relative fluorescence quantum yield $\phi_{fl}(T)$ of anisole as a function of temperature compared to data from Faust et al. [13] for N_2 as bath gas at 1 bar and Tran et al. [14] for bath gases N_2 , Ar, and CO_2 at 4 bar. The dashed line shows the fitted $\phi_{fl}(T)$ based on Eq. 38.

The T -dependence of $\sigma_{266 \text{ nm}}(T)$ and $\phi_{fl}(T)$ measured in this work for anisole can be described for temperatures between 296 and 980 K by a polynomial and an exponential function of T in K, respectively.

$$\frac{\sigma(\lambda)_{266 \text{ nm}}}{10^{-18} \text{ cm}^2} = 3.92 - T/538.5 - T^2/(6.1 \times 10^6) \quad (37)$$

$$\left. \frac{\phi_{fl}(T)}{\phi_{fl}(296 \text{ K})} \right|_{266 \text{ nm}} = \exp(1.64 - T/222 - T^2/(2.86 \times 10^5)) \quad (38)$$

Interference of the pyrolysis on LIF signal

Additional LIF experiments were performed between 1255 and 1620 K at a reaction time of 260 μs , where according to Figs. 37 and 39, pyrolysis is significant. As shown in Fig. 45, the spectra at higher temperature differ significantly from the ones at lower temperatures with the appearance of new spectral features far red-shifted compared to the original anisole-LIF spectrum. The LIF intensities shown in this figure are comparable to each other, showing that the trend observed at lower temperature of strongly decaying LIF intensity with temperature no longer persists at higher temperature. This result can qualitatively be explained by the formation of higher molecular weight species (e.g., naphthalene) with different LIF properties than anisole itself. The new spectra agree well with naphthalene spectra from Ref. [11].

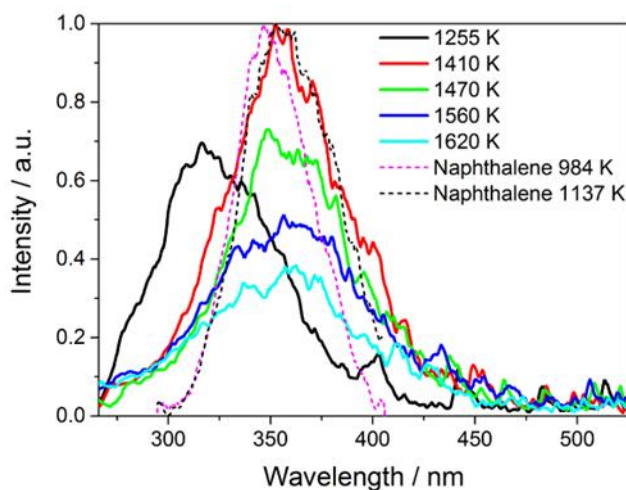


Fig. 45: LIF-emission spectra during pyrolysis of anisole as a function of temperature at 1.3 bar after excitation at 266 nm and at 260 μs after the arrival of the reflected shock wave. For comparison, high-temperature naphthalene-LIF spectra are shown [11].

5.2.4. Conclusions

Spectrally- and temporally-resolved UV absorption of anisole was studied at 565–1450 K. At temperatures up to 965 K, the absorption cross-section $\sigma(\lambda, T)$ of anisole between 240 and 310 nm was determined. A broadening and red-shift of $\sigma_{266\text{ nm}}(T)$ was observed with increasing temperature. These data extend the temperature range investigated so far.

The temporal behavior of the absorption was interpreted using information about decomposition products determined by HRR-TOF-MS. These experiments showed that under laboratory conditions, anisole is stable up to ~ 950 K. With increased temperature, naphthalene, benzene, cyclopentadiene, and CO were identified as main pyrolysis products. According to the experiments, where an increase in the absorption signals was seen, the detected species with mass spectrometry contribute to the absorption change. The concentration variations well match simulations based on a detailed kinetics model by Nowakowska et al. [72].

LIF spectra were measured at 296–1620 K using 266-nm excitation. Below 1000 K, the signal intensity of anisole-LIF decreases dramatically with increasing temperature mostly due to the

decrease of the fluorescence quantum yield $\phi_{fl}(T)$. Relative $\phi_{fl}(T)$ were measured for anisole at 296–980 K at pressures of 1.5 bar for excitation at 266 nm. Within this T -range, $\phi_{fl}(T)$ decreases by a factor of ~ 450 with increasing T . Above 1400 K, the LIF spectra show a more significant red-shift and discontinuity in the strong signal decrease found at lower temperature, which implies contributions from decomposition products. There are strong indications from the simulation of the reaction progress and the spectral analysis that the main contributor to this signal is naphthalene.

Anisole decomposes at lower temperature than some other tracers (e.g., toluene). The limiting temperature of ~ 950 K for a reaction time of several milliseconds is usually sufficient to cover the temperatures that occur in many practical conditions such as in IC engines, unless conditions with super-charging and very high compression ratio around TDC are addressed. On the other hand, anisole is preferable below this temperature limit because of its higher expected signal which especially is an advantage for ratio-based measurements used for temperature or oxygen-concentration imaging.

5.3. p-xylene and 1,2,4-trimethylbenzene

UV absorption and fluorescence emission spectra of p-XL and 1,2,4-TMB were measured at elevated temperatures behind reflected shock waves. In addition, time-resolved UV absorption measurements of their decomposition products were performed and the thermal stability of p-XL and 1,2,4-TMB were studied at high temperatures. The experimental data were compared to simulations using two kinetics models [75, 77] and absorption cross-sections for the respectively formed species from literature.

5.3.1. Absorption measurements

Effect of methyl substitution

The absorption cross-sections of o-XL, p-XL, 1,3,5-TMB, and 1,2,4-TMB at room temperature were determined and shown in Fig. 46.

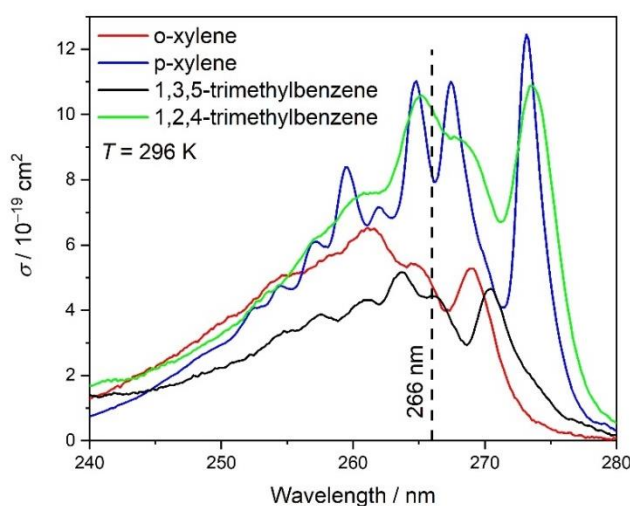


Fig. 46: Room-temperature UV absorption spectra of o-XL, p-XL, 1,3,5-TMB, and 1,2,4-TMB.

The UV absorption of the XL and TMB isomers is attributed to the $S_0 (^1A_{1g}) \rightarrow S_1 (^1B_{2u})$ electronic transition. As already discussed in theory section, many terms such as temperature can affect characterizations of both absorption and fluorescence spectra. One known effective phenomenon is localization of π -electron. The shape, intensity, and position of peaks are characteristic for absorption and fluorescence spectra that change with molecular structure and symmetry. Generally, any substituent shifts the absorption spectrum of the primary molecules (e.g., benzene) to longer wavelengths. Electron releasing and electron withdrawing through substituents and functional groups have different effects on intensity and position of absorption and fluorescence spectra. Because weak substituents reduce symmetry and enhance the number of vibrational possibilities, the weak transitions become intensified [154]. The addition of methyl groups into the benzene ring causes a small red shift of absorption and fluorescence spectra. It is known that introduction of electron releasing groups (e.g., CH_3 , OCH_3) leading to induction effect to the benzene ring increases the $S_0 - S_1$ absorption band intensity and wavelength [155]. The same effect has been observed with introduction of two

and three substituents to a benzene ring [156]. Typically in di-substituted benzene rings, para-isomers show transitions that are stronger and the absorption is at longer wavelength, whereas the effect of hyperconjugation in ortho-isomers is reduced because of steric interaction between the substituents [26]. Also with two of its three methyl groups in para position, 1,2,4-TMB exhibits a greater red-shift and more absorption than 1,3,5-TMB. Good agreement exists between the spectra shown in Fig. 46 and data of Bolovinos et al. [157] and Etzkorn et al. [153] (not shown in the figure). However, they only reported values at room temperature. Etzkorn et al. [153] experiments were carried out with a higher spectral resolution (0.15 nm) than in this work (~ 3 nm) and therefore the maximum absorption cross-sections in their study are somewhat higher (1.5×10^{-18} cm² (1,2,4-TMB) at 274 nm, 7.02×10^{-19} cm² at (1,3,5-TMB) 271 nm, 7.71×10^{-19} cm² (o-XL) 262 nm, 2.69×10^{-18} cm² (p-XL) 272 nm).

Temperature-dependence of absorption cross-section

Absorption spectra of p-XL and 1,2,4-TMB were measured as a function of temperature in the range from 296 to 1165 K at pressure of ~ 1.5 bar where p-XL and 1,2,4-TMB are stable over the reaction time behind the reflected shock wave. The results are shown in Fig. 47.

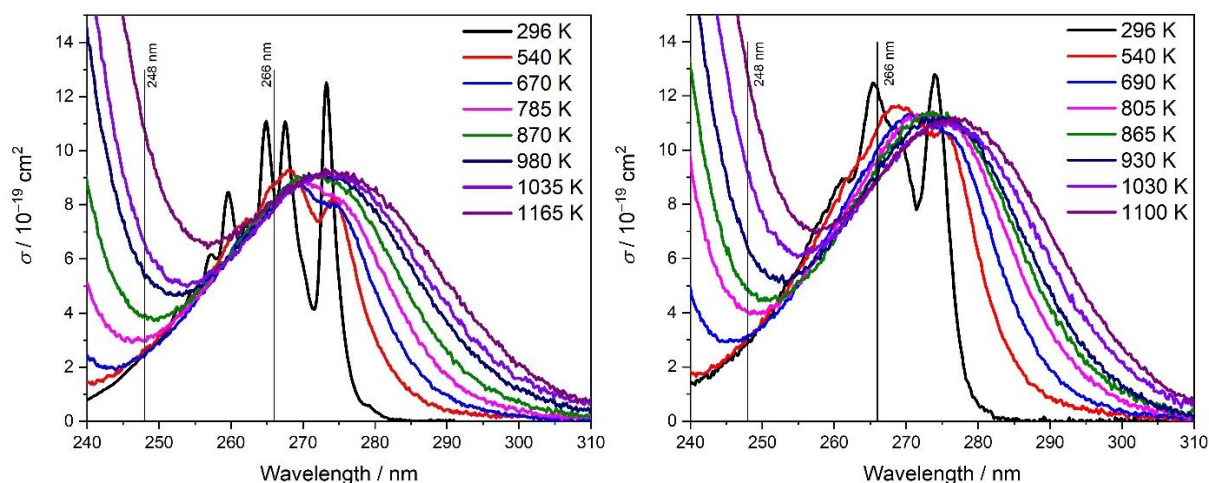


Fig. 47: Temperature effect on the absorption cross-section of p-XL (left panel) and 1,2,4-TMB (right panel).

The broad absorption feature is composed of a large number of individual lines; each of those lines having its particular temperature dependence as described by the Boltzmann population. The absorption spectra of p-XL and 1,2,4-TMB at room temperature show several sharp absorption features. Typically, the net effect of an increase in temperature is a shift and broadening in the structures. The absorption features in both diagrams broaden, which is due to the thermal population of vibrationally-excited ground state levels. With increasing temperature from 540 K, cross-section values at absorption peaks (273 nm for p-XL and 274 nm for 1,2,4-TMB) slightly increase, however at shorter wavelength, the values at peaks positions for p-XL (259, 264 and 267 nm) almost remain constant and for 1,2,4-TMB (265 nm) they decrease. The cross-sections at wavelengths greater than 275 nm increase with increasing tem-

perature. Below 260 nm, absorption spectra of p-XL and 1,2,4-TMB are strongly influenced by the S_0 – S_2 transition (with a very pronounced increase with temperature). In the case of aromatics, the absorption spectra generally shift to longer wavelengths with increasing temperature [12, 40]. The absorption maxima also shift with increasing temperature and are found at 275 nm at 1165 K for p-XL and at 276 nm at 1100 K for 1,2,4-TMB. Wang et al. [74] reported the measured the temperature dependence of the absorption cross-section of p-XL in the 423 to 623 K range in N_2 . Similar to the present study at 540 K, they identified two absorption peaks approximately at 265 nm and 275 nm at their lowest temperature of 423 K. However, the maximum absorption reported by Wang et al. is about a factor of two smaller than the measured absorption in this work.

Figure 48 shows trends in the absorption cross-section for 248 and 266 nm with respect to the temperature. The selected wavelengths correspond to the commonly used excimer and Nd:YAG lasers for LIF. There are clear differences considering changes of the absorption cross-sections for 248 and 266 nm. For both p-XL and 1,2,4-TMB, the temperature-dependence of the absorption cross-sections at 248 nm are more pronounced than at 266 nm, where the increase at 248 nm is considerably steeper than at 266 nm at higher temperatures. Below 700 K, the absorption cross-sections at 248 nm in both diagrams remain constant with temperature whereas above at this temperature, a rapid increase in absorption due to the crossing between absorption features of $S_0 \rightarrow S_1$ and $S_0 \rightarrow S_2$ occurs. The absorption cross-section of p-XL at 266 nm almost remains constant with increasing temperature, with a mean value equal to $(8.3 \pm 0.27) \times 10^{-18} \text{ cm}^2$. By comparison, at the same wavelength, the absorption cross-section of 1,2,4-TMB decreases continuously from $1.18 \times 10^{-17} \text{ cm}^2$ at room temperature to $9.06 \times 10^{-18} \text{ cm}^2$ at 1100 K.

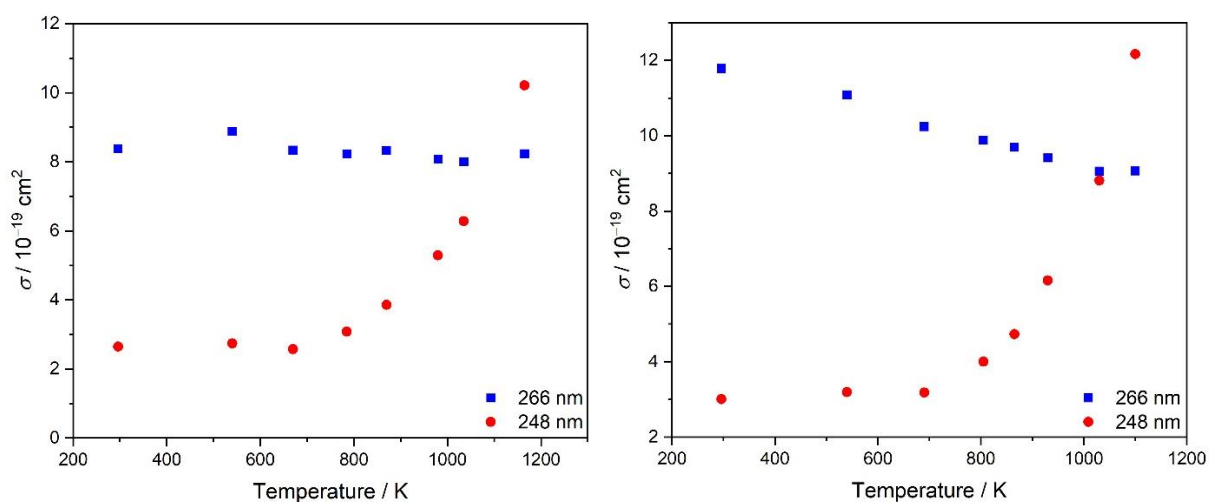


Fig. 48: Evolution of the absorption cross-sections of p-XL (left) and 1,2,4-TMB (right) at 248 and 266 nm as a function of the temperature.

Effect of pyrolysis on the effective absorption of p-XL and 1,2,4-TMB

In the temperature range shown in Fig. 47, thermal decomposition of p-XL and 1,2,4-TMB does not occur. The time-resolved absorption measurements aid in investigations of the chemical stability of the tracers at elevated temperatures and on the experimental timescale. Pyrolysis of p-XL and 1,2,4-TMB and consequently the effective absorption cross-sections σ_{eff} of the reaction product mixture strongly depend on temperature. Variations in absorption at a particular wavelength over the test time indicate the decomposition of p-XL and 1,2,4-TMB and formation of their products during pyrolysis. Fig. 49 shows the measured σ_{eff} at 266 nm (Eq. 29) during decomposition of p-XL and 1,2,4-TMB at temperatures up to 1605 K. Decomposition introduces new absorbing species with absorption characteristics different from those of the parent molecules.

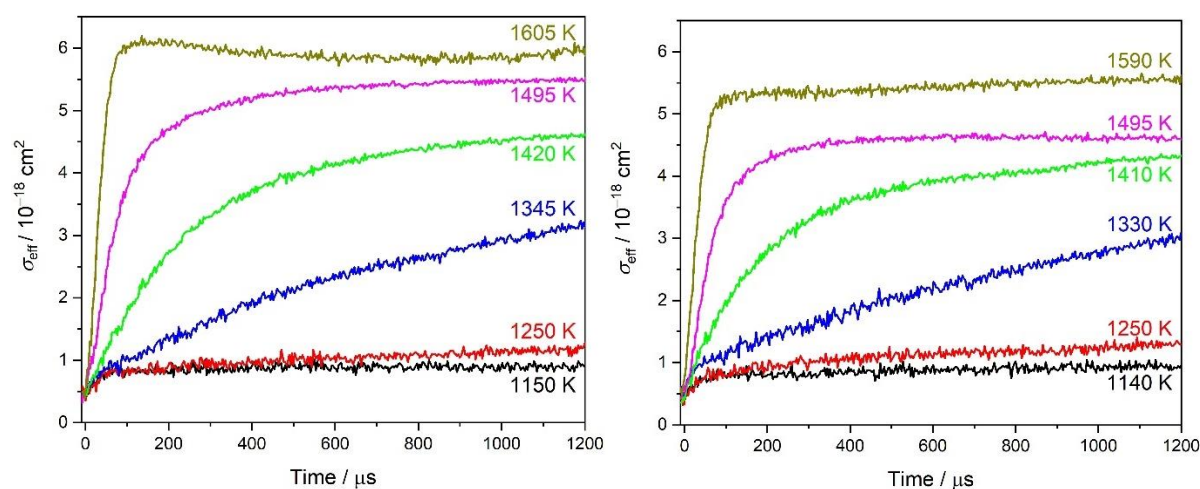


Fig. 49: Effective absorption cross-section of p-XL (left) and 1,2,4-TMB (right) at 266 nm of test mixtures originally containing 0.5% of tracer in Ar at 1.5 bar as a function of reaction time.

Similar to toluene (Sec. 5.1.1), enhanced formation of various radicals and molecules from p-XL and 1,2,4-TMB decomposition clearly lead to additional absorption at higher temperatures. Note, the slope of the increase and hence the velocity of formation of pyrolysis products is also temperature-dependent meaning that at high temperatures, decomposition of p-XL and 1,2,4-TMB and consequently formation of decomposition products takes place on a shorter timescale. Both tracers are stable over the reaction time at temperatures below 1150 K and σ_{eff} remains unchanged with temperature variations. Both p-XL and 1,2,4-TMB exhibit very similar stability over the experimental reaction time. However, from the difference between slopes of the effective absorption experiments at 1250 and 1150 K at shorter reaction times (e.g., at 300 μs), it can be assessed that 1,2,4-TMB is slightly more reactive than p-XL. This observation is consistent with the suggestion of Roubaud et al. [79] that separated the alkylbenzenes into two groups. The first group contains compounds that only ignited at temperatures above 900 K and 16 bar in their experiments in a rapid compression machine, i.e., toluene, p-XL, and 1,3,5-TMB and the second group includes compounds with higher reactivity that ignited at much lower temperature and pressure by the availability of ortho-alkyl groups, i.e., o-XL and 1,2,4-TMB.

Simulation of p-XL and 1,2,4-TMB decomposition

It is clear how complicate is the kinetics modelling of the alkylbenzenes. Only a few kinetics studies of p-XL and 1,2,4-TMB pyrolysis and oxidation have been reported in the literature. Therefore, there is still large uncertainty associated with the rate coefficients of several key reactions. The development of previously published mechanisms for p-XL [75] and 1,2,4-TMB [77] have been largely based on that of toluene. However, the rates of similar reactions have been adapted in a way to justify for reactivity of p-XL and 1,2,4-TMB against toluene. In both cases the initial reaction is easy, as a resonance stabilized benzyl-type radical is produced. The main unimolecular reaction channels of p-XL and 1,2,4-TMB are C–H bond fission forming an H atom and the p-methylbenzyl (p-xylyl) radical in R12 and dimethylbenzyl radicals in R13, respectively.



The products of R12 and R13 can undergo subsequent reactions, which need to be accounted for in the kinetics modeling of p-XL and 1,2,4-TMB pyrolysis.

Similar to the competition between the formation of benzyl and phenyl radicals in the initial decomposition reactions of toluene [66], p-methylphenyl (p-tolyl) radicals (C_7H_7) form in competition with p-methylbenzyl radicals as intermediates in the thermal decomposition of p-XL via a the loss of a methyl group. A branching ratio of about 90% was determined for the C–H bond fission by Troe et al. [158]. It is likely that the p-methylphenyl products (mainly toluene) increase in importance with increasing temperature. The second main step in p-XL pyrolysis is the H-atom abstraction from the methyl group of p-methylbenzyl. This results in two electronic structures a quinoid and a biradical form of $\text{p-CH}_2\text{C}_6\text{H}_4\text{CH}_2$. The quinoid form is typically more stable than the biradical form [159] and therefore, p-methylbenzyl radicals decompose mainly to p-xylylene (p-quinodimethane) and H atoms with a bond dissociation energy of 257.3 kJ/mol [160]. An alternative route in the decomposition of p-methylbenzyl radicals is via fulvenallene and methyl radicals. Fulvenallene formation might increase in importance with increasing temperature. However, da Silva et al. [160] estimated that this product only accounts for about 2–5% of the total p-methylbenzyl decomposition at relevant temperatures. The left panel of Fig. 50 illustrates the contributions from the main absorbing species in p-XL decomposition at 1415 K based on the mechanism of Battin-Leclerc [75].

From decomposition of 1,2,4-TMB, three isomers (i.e., 2,4-dimethyl-, 2,5-dimethyl-, and 3,4-dimethylbenzyl radicals) can be generated by abstracting an H atom from different positions within the methyl groups. Bikas [76] suggested that the most dominant product during the initial decomposition of 1,2,4-TMB is the 3,4-dimethylbenzyl radical formed by abstracting an H atom from the methyl group at the 4-position. The decomposition pathways of dimethylbenzyl radicals (C_9H_{11}) mainly leads to the formation of methylbenzyl radicals (C_8H_9) and

xylene isomers (C_8H_{10}). Secondary reactions can lead to complicated mechanisms at longer reaction times. A species-selective interpretation of the absorption at longer times is not the focus of this work (and not feasible under the conditions studied here because of secondary reactions). For 1,2,4-TMB, the kinetics model was taken as that developed for representing the kerosene surrogate from Honnet et al. [77]. This model includes a semi-detailed description of the 1,2,4-TMB decomposition kinetics. Predicted concentration–time profiles of 1,2,4-TMB and its main initial intermediate species at 1415 K are shown in Fig. 50 (right) based on the mechanism of Honnet et al.

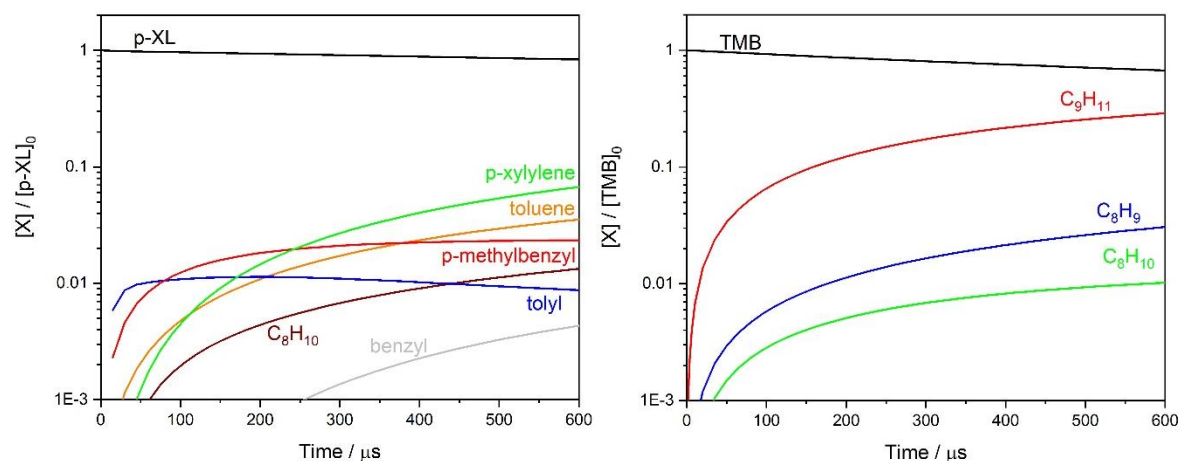


Fig. 50: Simulated concentration–time profiles for exemplary studied temperature at 1415 K based on the mechanism of Battin-Leclerc et al. [75] for p-XL (left) and Honnet et al. [77] for 1,2,4-TMB (right). For clarity, only species which have a maximum concentration above 2 % relative to the initial p-XL and 1,2,4-TMB concentrations at $t = 0$ are shown.

Using the results of the reaction mechanisms and the measured absorption cross-sections, species were then chosen to obtain deeper insight into which products might contribute to the increased absorption after decomposition of p-XL and 1,2,4-TMB and to which extent they do so. Therefore, the fractional absorption was simulated using the kinetics models in conjunction with absorption data of the corresponding species (Fig. 51). The pyrolysis of p-XL and 1,2,4-TMB was simulated using the mechanisms published by Battin-Leclerc et al. [75] and Honnet et al. [77], respectively. The comparison of numerical simulations and the corresponding measured fractional absorption can also help to check the prediction of existing kinetics models especially in the initial phase of the decomposition. The simulated fractional absorption is calculated via Eq. 36 with respect to the absorption by p-XL, p-methylbenzyl radicals, p-xylene, and toluene for p-XL decomposition and dimethylbenzyl radicals, methylbenzyl radicals, and xylenes for 1,2,4-TMB decomposition.

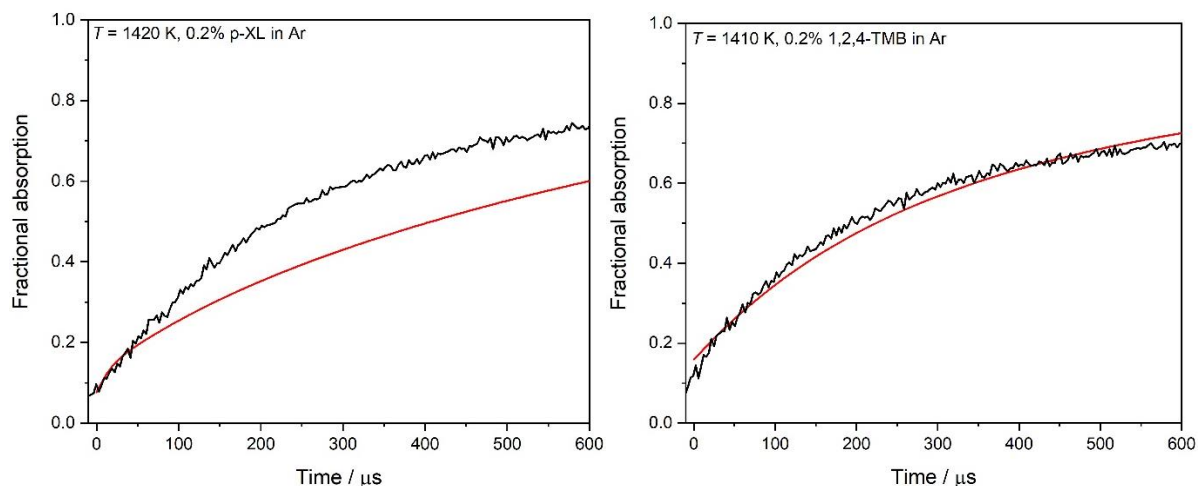


Fig. 51: Variation of the fractional absorption (black solid lines) and model predictions (red dashed lines) of p-XL and 1,2,4-TMB at 266 nm over the reaction time of 600 μs after the arrival of the reflected shock wave.

The measured absorption cross-sections of p-XL and 1,2,4-TMB in the present study were $\sigma_{\text{p-XL}} = 8.3 \times 10^{-19} \text{ cm}^2$ and $\sigma_{1,2,4\text{-TMB}} = 9.1 \times 10^{-19} \text{ cm}^2$. The absorption cross-section of toluene was previously determined from the time-zero absorbance prior to toluene decomposition $\sigma_{\text{toluene}} = 5.9 \times 10^{-19} \text{ cm}^2$ [66]. Brand et al. [161] reported the absorption cross-section of p-methylbenzyl ($\sigma_{\text{p-methylbenzyl}} = 2.9 \times 10^{-17} \text{ cm}^2$) at 266 nm and for $1550 \pm 150 \text{ K}$. Astholz et al. [37] determined a strong broadband absorption for p-methylbenzyl in the range 230–340 nm with $\sigma_{\text{p-methylbenzyl}} = 1.3 \times 10^{-17} \text{ cm}^2$ at 266 nm and 1650 K behind reflected shock waves. Lee [162] found the broadband absorption of p-methylbenzyl radicals at 300 K and $\sigma_{\text{p-methylbenzyl}} = 2.2 \times 10^{-17} \text{ cm}^2$ at 266 nm, where p-methylbenzyl was generated by laser flash photolysis of Cl_2 at 308 nm and the subsequent reaction of Cl atoms with excess p-XL. These results are in good agreement with the estimation of temperature-independent absorption cross-sections for benzyl-type radicals, which has been previously observed in the case of toluene (cf. Sec. 5.1.1 and Ref. [66]). Thermal decomposition of the p-methylbenzyl radicals has also been studied by Hippler et al. [163] using time-resolved UV-absorption spectroscopy at 265 nm and p-methylbenzyl iodide as a precursor. They attributed the measured absorption to the immediately formed p-methylbenzyl radicals. However, Fernandes et al. [164] showed later that the UV-absorption reported in [163] has been misinterpreted. They re-evaluated the old experiments and found that the observed absorption must be attributed to the product of p-methylbenzyl decomposition, i.e., p-xylylene with $\sigma_{\text{p-xylylene}} = 1.25 \times 10^{-17} \text{ cm}^2$.

In literature, no direct study of the absorption band of dimethylbenzyl radicals in the UV region is available. However, the absorption and the spectral features of dimethylbenzyl radicals in the UV region should not be so different from those of benzyl ($\sigma_{\text{benzyl}} = 1.9 \times 10^{-17} \text{ cm}^2$ [66] at 266 nm) and methylbenzyl radicals ($\sigma_{\text{m-methylbenzyl}} = 1.0 \times 10^{-17} \text{ cm}^2$ at 260 nm [161]). Thus, for dimethylbenzyl, an analogous absorption cross-section to methylbenzyl was used.

Before the arrival of the shock wave (time zero), absorption by p-XL and 1,2,4-TMB is weak and negligible compared to the absorption after the shock wave. At higher temperatures, the following gradual change is due to chemical processes induced by the sudden increase in

temperature. As already mentioned, the observed fractional absorption strongly depends on temperature. With increasing temperature, the rate of product formation and the total fractional absorption significantly increase.

The comparison between simulations and experiments confirms that at short reaction times, the absorption behind the reflected shock wave is mainly dominated by the products of H atom abstraction from one methyl group of p-XL and 1,2,4-TMB. After the passage of the reflected shock wave the fast dissociation of p-XL and 1,2,4-TMB at high temperatures quickly provides methylbenzyl and dimethylbenzyl radicals respectively and thus contributes to strongly increased absorption. Absorption caused by other species like phenyl-type radicals was considered negligible due to their low concentrations during the observation time of the present experiments. The agreement between simulations based on the mechanism of Honnet et al. [77] and experiments in the case of 1,2,4-TMB is reasonable over the investigated reaction time. The model of Battin-Leclerc et al. [75] is able to reproduce the experimental trends, especially at short times ($<100 \mu\text{s}$) where the primary dissociation channels are the only sensitive reaction. On a longer timescale (i.e., $>100 \mu\text{s}$), however, the deviation gets more pronounced because of the additional contribution of secondary reaction products in the measurement that are not considered by the present model. Similar to toluene (cf. Sec. 5.1.1), the additional fractional absorption at longer reaction times is probably caused by formation of aromatic radicals and the following PAHs pyrolysis products.

5.3.2. LIF measurements

Temperature dependence of LIF spectra

LIF spectra of p-XL and 1,2,4-TMB were measured as a function of temperature between room temperature and 1165 K at a pressure about 1.5 bar using a mixture of 0.5% of the respective species diluted in argon. Figure 52 shows the recorded LIF spectra behind the reflected shock wave as a function of temperature. Similar to other mono-cyclic aromatic hydrocarbons (i.e., toluene and anisole) the fluorescence intensities drastically decrease with increasing temperature, which is slightly more pronounced for 1,2,4-TMB. For a better comparison, fluorescence signals at different temperatures were normalized to their fluorescence signals at 540 K. The LIF spectra of p-XL and 1,2,4-TMB slightly red-shift with increasing temperature and become broader. As discussed in the previous section, increasing the substitution number is known to slightly shift the absorption and fluorescence spectra towards longer wavelengths [155, 156]. At room temperature, the LIF spectra peak of p-XL and 1,2,4-TMB occurs at 286 and 290 nm, respectively. The maximum of the fluorescence spectrum of p-XL shifts by $\sim 2.2 \text{ nm}$ per 100 K to longer wavelengths and the fluorescence spectrum of 1,2,4-TMB exhibits a red-shift about 2.6 nm per 100 K. The behavior of the fluorescence spectra of 1,2,4-TMB agrees well with the results of Benzler et al. [42], who reported a red-shift of the fluorescence spectrum around $2.5 \text{ nm}/100 \text{ K}$ with increasing temperature from 300 to 1025 K.

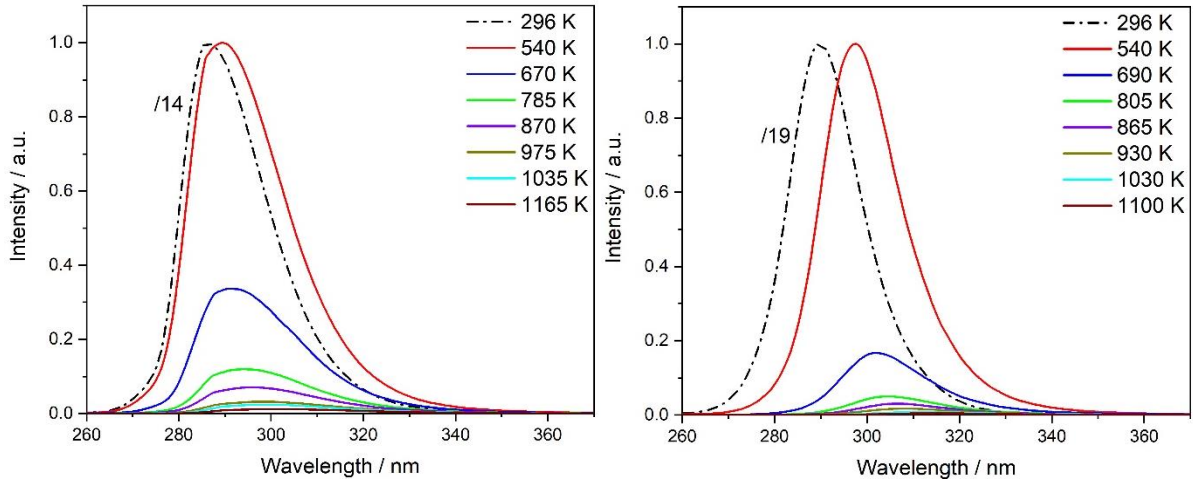


Fig. 52: LIF emission spectra of p-XL (left) and 1,2,4-TMB (right) upon 266-nm excitation at 1.5 bar. The spectra for shock-heated gases are normalized to the peak values of the measurements at 540 K. The dashed line (296 K) shows measurements in the shock tube under static conditions. For comparison, their intensities are divided by a factor of 14 and 19 for p-XL and 1,2,4-TMB, respectively.

Relative fluorescence quantum yield

The temperature dependence of the fluorescence signal of p-XL and 1,2,4-TMB is results from the changes in the absorption cross-section and relative fluorescence quantum yield for a given excitation wavelength with the respective temperature $S_{fl} \propto n_{fl}\sigma(\lambda_{ex}, T)\phi_{fl}(\lambda_{ex}, T)$. This gives a global understanding of the evolution of the LIF signals with increasing temperature. The relative dependence of the fluorescence quantum yield on the temperature is shown in Fig. 53. The calculation is based on Eq. 7 (Sec. 2.1.4.1). The fluorescence quantum yield of p-XL and 1,2,4-TMB decreases by about three orders of magnitude with increasing temperature from room temperature up to 1000 K. However, the fluorescence quantum yield of 1,2,4-TMB at 266 nm excitation shows a slightly steeper exponential decrease than p-XL with increasing temperature. This may be attributed to the effect of non-radiative deactivation processes that vary from one species to the other. The results of 1,2,4-TMB are consistent with recently published studies in flow cells upon excitation at 266 nm [40, 42]. Benzler et al. [42] observed a similar decrease in fluorescence life time of 1,2,4-TMB with increasing temperature. The temperature-dependent relative FQYs for 1,2,4-TMB in this work correlate well with the data calculated from effective fluorescence lifetimes from Benzler et al. [42] measured at 296–1066 K and normalized to the FQY value at 296 K (Fig. 53). The suggested single exponential decays value by Rossow [40] is slightly lower than the here presented results. Exponential fits for p-XL and 1,2,4-TMB fluorescence quantum yields were provided over a wide range of temperatures for further development of photo-physical models.

$$\text{p-XL} \quad \frac{\phi_{fl}(T)}{\phi_{fl}(296 \text{ K})} \Big|_{266 \text{ nm}} = \exp(3.72 - T/73 + T^2/(2.61 \times 10^5)) \quad (39)$$

$$\text{1,2,4-TMB} \quad \frac{\phi_{fl}(T)}{\phi_{fl}(296 \text{ K})} \Big|_{266 \text{ nm}} = \exp(4.37 - T/61.31 + T^2/(1.93 \times 10^5)) \quad (40)$$

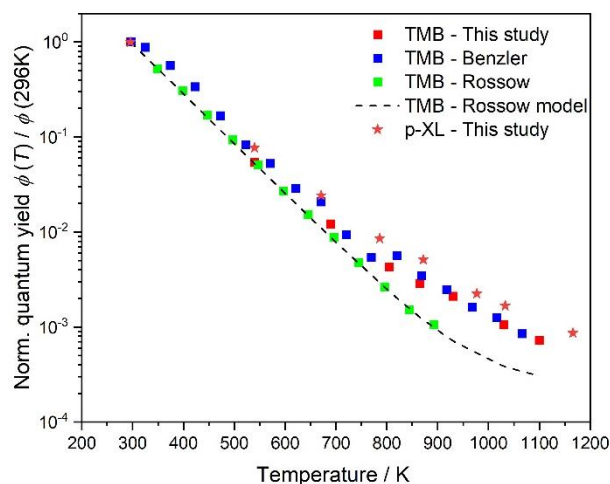


Fig. 53: Relative fluorescence quantum yield of p-XL and 1,2,4-TMB as a function of temperature. Results from this work are compared with previous data from Rossow [40] and Benzler et al. [42].

5.3.3. Conclusions

A series of UV-absorption and LIF spectra of p-XL and 1,2,4-TMB diluted in argon was measured at elevated temperatures and a pressure about 1.5 bar behind reflected shock waves. Absorption cross-sections of p-XL, o-XL, 1,3,5-TMB, and 1,2,4-TMB have been determined and compared at room temperature. UV-absorption spectra of p-XL and 1,2,4-TMB were obtained at temperatures up to 1165 K and in the range of 240 to 310 nm. With increasing temperature, the absorption cross-sections increase and the spectra slightly red-shift. Additionally, the effective absorption cross-sections at 266 nm during pyrolysis of p-XL and 1,2,4-TMB have been examined with respect to the reaction time behind reflected shock waves. The fractional absorption of p-XL and 1,2,4-TMB at 1415 K was compared to simulations, based on the mechanisms of Battin-Leclerc et al. [75] and Honnet et al. [77], respectively. In addition, the effect of temperature on the fluorescence spectra was investigated. The fluorescence signal intensities significantly decrease with increasing temperature. The LIF spectra of p-XL and 1,2,4-TMB red-shift and broaden with increasing temperature. The fluorescence quantum yield decreases for both species with increasing temperature by about three orders of magnitude from room temperature to 1000 K. There is good agreement between the measured fluorescence quantum yield and the literature data.

5.4. Acetylene

This section presents results of absorption spectroscopy of acetylene (C_2H_2) behind reflected shock waves. Absorption cross-sections of C_2H_2 were measured before the pyrolysis occurs. Time-resolved measurements allow to observe the onset of C_2H_2 decomposition and thus ensure that the measurements are not affected by high-temperature reactions. Laser-induced fluorescence measurements were performed using 266-nm excitation and the temperature dependence of the relative fluorescence quantum yield is determined from the data of absorption cross-sections and relative fluorescence intensities. The work in this section has been published in peer-reviewed publication 2 (cf. list of own publications).

5.4.1. Absorption measurements

UV absorption spectra of shock-heated acetylene diluted in argon were measured for 565–1500 K at 2.5 bar. Figure 54 shows the detected absorption spectra in the 200–300 nm range with a spectral resolution of 7 nm. At room temperature, the measured absorption band (at 500 mbar) was consistent with literature [112]. This band is attributed to a $S_0(\tilde{X}^1\Sigma_g^+) \rightarrow S_1(\tilde{A}^1A_u)$ transition. For temperatures up to 1500 K, where no decomposition of C_2H_2 is expected [165, 166], absorption cross-sections were determined using the Beer-Lambert law (Eq. 4). The $\tilde{X} \rightarrow \tilde{A}$ transition below 240 nm shows a significant increase with temperature. At 930 K, the spectrum exhibits an absorption cross-section of $\sigma = (7.4 \pm 0.9) \times 10^{-20} \text{ cm}^2$ at its maximum ($\sim 205 \text{ nm}$). The entire spectra red-shift and broaden (between 200 and 300 nm) with increasing temperature. Consequently, the maximum of the absorption cross-section at 1500 K increases to $\sigma = (3.97 \pm 0.5) \times 10^{-19} \text{ cm}^2$ and shifts to $\sim 218 \text{ nm}$.

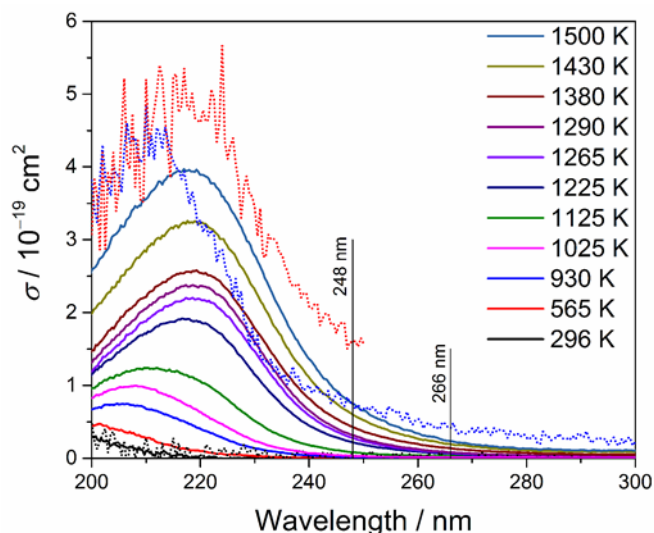


Fig. 54: Absorption cross-sections of C_2H_2 from room temperature to 1500 K measured with 5% C_2H_2 in Ar. Total pressure at room temperature: 500 mbar, at elevated temperatures: 2.5 bar. The dotted lines show absorption spectra from Vattulainen et al. [112]: black dotted line: 296 K, blue dotted line: 873 K, and red dotted line: 1073 K.

Figure 54 also shows previously published data on temperature-dependence of C_2H_2 absorption cross-sections. The comparison shows a good match of the corresponding wavelength

range and absolute trend of C_2H_2 absorption cross-sections at various temperatures, but the data presented here significantly expands the investigated temperature range and therefore provides data that can be relevant for many optical measurements in the UV in combustion systems.

The absorption cross-sections of C_2H_2 in the range of 230–280 nm and 930–1500 K were fitted to experimental data using a semi-empirical function: $\ln \sigma_{C_2H_2}(\lambda, T) = a + b\lambda + c\lambda^2$ (cf. Fig. 55), where $a = d_1 + d_2T + d_3/T$, $b = e_1 + e_2T + e_3/T$ and $c = f_1 + f_2T + f_3/T$. The respective parameters are listed in Table 3.

Table 3: Fit coefficients used in the expression to semi-empirical fit function.

i	1	2	3
d_i	-419.09034	0.12907	406705.93713
e_i	3.52772	-0.00107	-3335.33186
f_i	-0.00726	2.19766×10^{-6}	6.64674

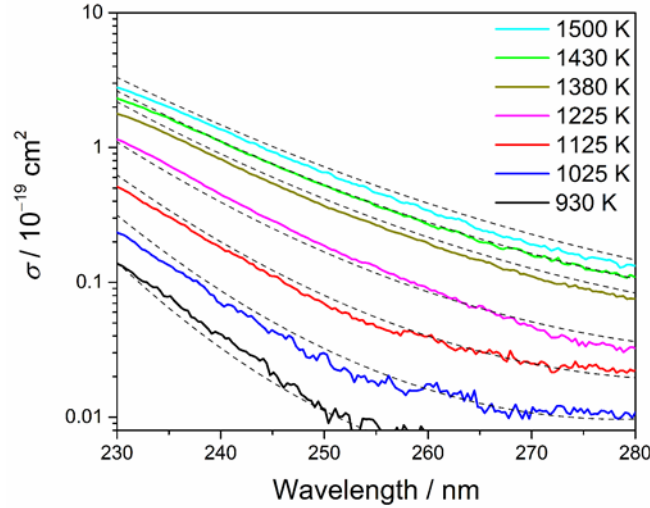


Fig. 55: Absorption cross-sections of C_2H_2 as a function of temperature between 230–280 nm at 2.5 bar. Solid lines: experimental data, dashed lines: calculated data from the semi-empirical function.

The uncertainties in the absorption measurements vary with the magnitude of the absorption cross-sections from ± 12 to $\pm 30\%$. The uncertainties are derived from an error propagation taking into account the error in baseline intensity (I_0) and transmitted light intensity (I) as well as errors in temperature, pressure, and initial gas concentration. Figure 56 shows the absorption cross-sections from Fig. 54 at 248 and 266 nm as a function of temperature. At both wavelengths, C_2H_2 is essentially transparent below 900 K. At higher temperatures, the absorption cross-section strongly increases with temperature.

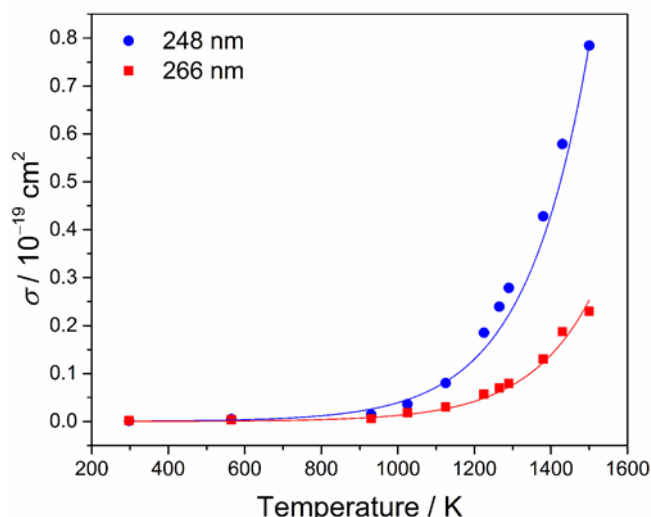


Fig. 56: Absorption cross-sections of C_2H_2 at 248 and 266 nm as a function of temperature. Symbols: measurements, lines: single-exponential fit (see text).

The temperature dependence of the absorption cross-sections of C_2H_2 at 248 and 266 nm can be fitted as a single-exponential function of temperature.

$$\frac{\sigma(\lambda)_{248 \text{ nm}}}{10^{-19} \text{ cm}^2} = 9.70 \times 10^{-5} \times \exp(0.006 \text{ K}^{-1} \times T) \quad (41)$$

$$\frac{\sigma(\lambda)_{266 \text{ nm}}}{10^{-19} \text{ cm}^2} = 3.12 \times 10^{-5} \times \exp(0.006 \text{ K}^{-1} \times T) \quad (42)$$

When exceeding the temperature range beyond 1500 K, even in the initial phase after shock heating, the measured absorption spectra are affected by absorbing intermediates from C_2H_2 decomposition. For higher temperatures and long reaction times, polyacetylenes and aromatics are formed and strongly contribute to the overall absorption preventing the interpretation of time-dependent absorption spectra. Therefore, measurements can no longer deliver reliable absorption data for certain species. For the temperatures below 1500 K the fractional absorption is constant and can be attributed to acetylene. At longer residence times such as in heated cells, the limiting temperature can be significantly lower. In the measurements of Vattulainen et al. [112] that so far presented the highest temperature data for C_2H_2 absorption cross-sections, measurements at room temperature are in good agreement with the here presented data. At 873 and 1073 K, however, their reported cross-sections are higher by a factor of ~ 5 at the maximum (cf. Fig. 56). The measurements in [112] might be affected by decomposition products due to long residence times and contact of the gas to hot surfaces. C_2H_2 decomposes on the order of seconds at 1000 K [94, 167]. In a recently published kinetics model, the formation of intermediates and polyacetylenes up to C_8H_2 was described [166]. The main primary pyrolysis product of acetylene is C_4H_2 with $\sigma_{260 \text{ nm}} = 2.725 \times 10^{-20} \text{ cm}^2$ at 295 K and $\sigma_{260 \text{ nm}} = 3.001 \times 10^{-20} \text{ cm}^2$ at 333 K [168]. These data show again an increase of absorption cross-sections with temperature at longer wavelength. Due to the $C \equiv C$ triple bonds in polyacetylenes and their similar molecular geometry, a similar temperature dependence of the absorp-

tion cross-section is expected at longer wavelength. Additionally, intermediates formed during C_2H_2 pyrolysis such as C_2H radicals might be strong absorbers that also contribute to the overall absorption at higher temperatures. The C_2H radical is a broadband absorber in the 235–248 nm range with a maximum absorption at ~ 243.5 nm ($\sigma_{243.5 \text{ nm}} = (7.5 \pm 0.9) \times 10^{-19} \text{ cm}^2$ at room temperature [169]). Condensation products formed from fragments also absorb in the UV. Therefore, the presence of interfering absorbing species in previously published high-temperature absorption data of C_2H_2 is not entirely unexpected.

5.4.2. LIF measurements

Temperature dependence of LIF spectra

LIF experiments are carried out in the 935–1500 K range. Figure 57 shows LIF spectra at a fixed detection time of 360 μs after the arrival of the reflected shock wave as a function of temperature. As expected from the absorption measurements, no signal is observed upon excitation at 266 nm at temperatures below 900 K. Starting from 935 K, C_2H_2 LIF is detected in the 280–490 nm wavelength range with a maximum at around 350 nm. With increasing temperature, the LIF spectra broaden, but no shift of the fluorescence maximum is observed.

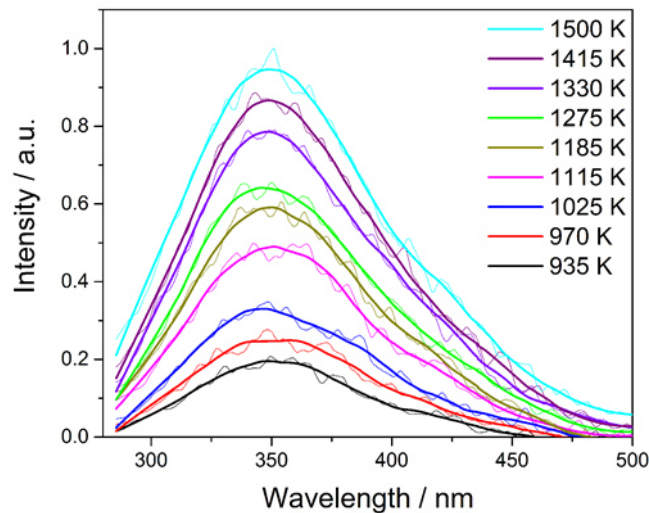


Fig. 57: Single-shot LIF emission spectra of acetylene after excitation at 266 nm as a function of temperature at a pressure of 2.5 bar, measured at 360 μs after the arrival of the reflected shock wave. Bold lines are smoothed while fine lines show the signal variability in the underlying single-shot images.

In order to analyze the photophysical behavior of the fluorescing species, the fluorescence intensities are presented on a per-molecule basis, i.e., the total fluorescence signal per volume is divided by the species number density [39]. Figure 58 shows the normalized temperature dependence of the effective C_2H_2 fluorescence per molecule S_{fl}^* between 935 and 1500 K using excitation at 266 nm relative to the value at 935 K. The C_2H_2 fluorescence increases almost linearly with increasing temperature according to $\left. \frac{S_{fl}^*(T)}{S_{fl}^*(935 \text{ K})} \right|_{266 \text{ nm}} = -10.22 + 0.012 T/\text{K}$ for 935–1500 K (cf. Fig. 58). Uncertainties in the fluorescence intensity measurements are estimated at about $\pm 9\%$.

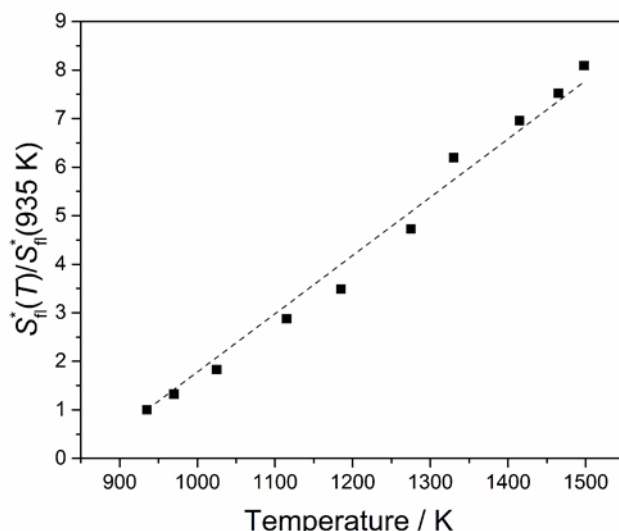


Fig. 58: Relative acetylene fluorescence signal per molecule after excitation at 266 nm as a function of temperature at a pressure of 2.5 bar. The dashed line represents a linear fit to the data.

Relative fluorescence quantum yield

In fluorescing organic molecules (e.g., toluene and acetone) the total LIF intensity usually decreases with increasing temperature because non-radiative decay rates of the excited state increase with thermal excitation (see Sec. 2.1.3). In case of aromatic molecules the temperature-dependent decay is especially strong (previous sections and Refs. [12, 13]). In these cases, the total signal is determined by the temperature dependence of the fluorescence quantum yield and changes in absorption cross-sections have a minor influence only. In contrast, the LIF intensity of C_2H_2 increases with temperature because of the strong increase of the absorption cross-section with temperature. This effect over-compensates the expected temperature-dependent decrease in fluorescence quantum yield shown in Fig. 59. The calculation of the relative effective fluorescence quantum yield is explained in detail in Sec. 2.1.4.1. Because of the absence of absorption and fluorescence at room temperature, the ϕ_{fl} data are normalized to the fluorescence quantum yield to 935 K. A single-exponential fit is shown on the plot according to:

$$\left. \frac{\phi_{fl}(T)}{\phi_{fl}(935 K)} \right|_{266 nm} = 14.24 \times \exp(-T/352 K) \quad (43)$$

As expected, ϕ_{fl} decreases with increasing temperature which is attributed to increasing non-radiative rates with higher vibrational excitation.

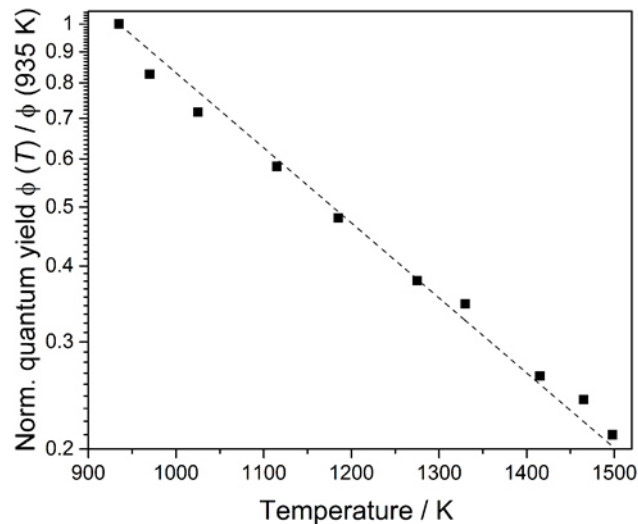


Fig. 59: Relative effective fluorescence quantum yield of C_2H_2 as a function of temperature in Ar after 266 nm laser excitation. The data are normalized to the value at 935 K. Symbols: measurements, line: single-exponential fit (see text).

5.4.3. Conclusions

UV absorption cross-sections of acetylene have been studied over a wide temperature range (565–1500 K) behind reflected shock waves at 2.5 bar. With increasing temperature, the absorption spectra show a strong increase in absorption cross-sections leading to a red-shift of the long-wavelength tail of the absorption feature. The absorption cross-sections have been described by a semi-empirical model for the 230–280 nm range. At 248 and 266 nm, the absorption cross-sections are negligible below 900 K but then strongly increase with increasing temperature. Within the time resolution of the shock tube experiment, measurements were possible up to 1500 K without interference from decomposition products.

Laser-induced fluorescence of C_2H_2 was also studied upon 266-nm excitation. Above 900 K, broadband fluorescence in the 280–500 nm range was observed. With increasing temperature, the total fluorescence intensity increases and the emission spectra broaden while the peak wavelength remains at 350 nm. The fluorescence quantum yield decreases with increasing temperature for 266-nm excitation. The effective LIF-signal intensity per molecule increases almost linearly with temperature, making C_2H_2 a potential target molecule for temperature measurements in homogeneous non-reactive systems at high temperature beyond the temperature limit of conventional fluorescence tracers.

Because C_2H_2 is formed in many combustion systems as a decomposition product of hydrocarbon fuels, C_2H_2 must be considered as a potential source of interference at high-temperature laser-based diagnostics in combustion processes. However, the fluorescence signal of acetylene might open up new opportunities for diagnostics for high-temperature mixing or combustion processes where common organic fluorescence tracers are not stable any more.

6. A novel methodology for reaction-time-resolved LIF (RTR-LIF) measurements in shock tubes

This chapter mainly represents the contents of the peer-reviewed publication 4 (cf. list of own publications). It presents details about the new RTR-LIF measurement strategy using a new optically accessible test section with multiple rectangular and circular optical ports on side walls and the endwall of the shock tube that allow for performing RTR-LIF and absorption measurements simultaneously.

6.1. Motivation: Collecting more LIF data from each single shock-tube experiment

Shock tubes are well established to study ultra-fast gas-phase reactions at high temperatures [170]. The reaction is initiated by a shock wave and reactions are observed over the initial test time of few hundred microseconds to few milliseconds often behind reflected shock waves. Typical kinetics studies cover a wide range of test gas conditions. One operational difficulty of conventional shock tubes is the low repetition rate of the experiments where only few experiments can be carried out per hour. Recently, new types of shock tubes (e.g., diaphragm-less shock tubes [171]) have been presented that permit to run shock tubes with repetition rates of around one per minute. Generally, it is desired to gain as much information from each single experiment as possible. Measurement strategies are typically selected that allow for time-resolved detection after the arrival of the shock wave with a typical temporal resolution of a few microseconds. Some examples are light emission measurements with high temporal resolution [172, 173], laser absorption methods through multiplication of equipment [45, 46]) and intracavity absorption spectroscopy (ICAS) [174]. All these measurements generate continuous signal traces during the test time of the shock-tube experiment. Fluorescence measurements are typically not carried out because they require pulsed-laser excitation and therefore only generate a single data point.

As mentioned in the previous sections, understanding the decomposition kinetics of fluorescence tracer species [45, 46, 66] is of interest (e.g., in gas mixing and temperature measurements in IC engine [5]) because it could cause severe misinterpretation of the practical measurement if the adopted tracer is changing in concentration or is reacting to additional species that also fluoresce and interfere with the desired quantities.

While the latter effects have mostly been studied by absorption, LIF measurements are required to provide additional information about the variation of fluorescence as a function of temperature and tracer decomposition. Because of the low concentrations and the high desired time resolution, intense lasers are required for the measurement. These are in almost all cases pulsed lasers. Usually, the laser crosses the shock tube through two side windows close to the endplate, and the signal is detected either through an additional side window or through a large window in the endplate that allows detection with a large solid angle (cf. Sec. 4.3.2 and Ref. [12]). With single-shot excitation in conventional arrangement, a single data point in time can be gained from each shock tube experiment only [12, 91]. The delay between the

arrival of the shock wave and the laser experiment can be pre-set, but measuring a sequence of single fluorescence spectra as a function of time after shock arrival is not only extremely time consuming, it is also hampered by the fact that the post-shock conditions in subsequent experiments cannot be exactly reproduced and individual data points need to be corrected for the individual pressure and temperature values. Accordingly, there is a continuing need to achieve more information from one single laser shot.

Reaction-time-resolved laser-induced fluorescence (RTR-LIF) that covers several reaction times in a single shock-tube experiment is possible with the same optical arrangement described above with continuous wave lasers or with high-repetition pulsed lasers. Note that to clearly distinguish the present experimental approach against time-resolved laser-induced fluorescence measurements (TR-LIF) that is usually adopted for studying the photophysics during the laser event, the presented method here is referred to as reaction-time-resolved laser-induced fluorescence with the acronym RTR-LIF. The pulse repetition rate even of modern high-repetition-rate diode-pumped solid-state lasers is in the ten kHz regime, however, is not sufficient to detect reaction-time-resolved information within a single shock-tube experiment. Pulse-burst lasers [175, 176] allow higher repetition rates but are costly. CW lasers on the other side provide comparably low fluences within the desired short detection times and hence insufficient signal, and are usually not tunable.

In an attempt to realize RTR-LIF in a much simpler way using a single pulsed laser, a new test section was designed and built (cf. Sec. 4.1.1) that enables LIF measurements at variable reaction times with unconventional detection arrangement that described thoroughly in Sec. 6.2. Owing to its relevance as fluorescence tracer and its favorable fluorescence properties, anisole was chosen to demonstrate the feasibility of the RTR-LIF method.

6.2. New design to realize RTR-LIF

RTR-LIF experiment

Signals with the RTR-LIF method were recorded using the setup illustrated in Fig. 60. The gas mixture is excited along the center of the shock tube by the pulsed frequency-quadrupled Nd:YAG laser at 266 nm (fluence ~ 10 mJ/cm²). The laser beam is formed into a vertical light sheet (~ 0.5 mm wide, ~ 5 mm high) with a combination of spherical and cylindrical lenses. It is guided parallel to the measurement section towards the center of the endwall of the driven section and directed perpendicular to the endwall using highly-reflective turning mirrors. Via a beam splitter, 20% of the laser beam is directed to the power meter to measure and correct for laser pulse energy fluctuations during subsequent experiments.

The fluorescence signal was collected perpendicularly to the direction of laser propagation through the top window from the center of the shock tube and focused with a $f = 105$ mm achromatic UV-transparent lens ($f/4.5$, CoastalOpt) on the entrance slit of the spectrograph (150 g/mm grating) coupled to the intensified CCD camera (300 ns gate time). An image is

then recorded by the 1024×1024 pixel ICCD camera with one spatial and one spectral coordinate. The spatial axis covered a range of 45 mm with a projected pixel size of $\sim 44 \mu\text{m}/\text{pixel}$. The spatial resolution of the imaging system is $\sim 300 \mu\text{m}$ as measured by a USAF resolution target. The spectral axis covered the range from 200–790 nm as calibrated by reference lines of a low-pressure Hg(Ar) pen-ray lamp with a spectral resolution of 10 nm FWHM.

To reduce the dark noise, the CCD was Peltier-cooled to -12°C . All raw images were corrected for dark current contribution and flat-field using an average over 60 images prior to the shock loading. Flat-field correction was carried out using the same optical setup as for experiments with a homogeneously seeded tracer mixture at room temperature with seeding concentrations for which laser beam attenuation over the spatial dimension could be neglected. The signal variation along the spatial coordinate was used to correct the measured data. A long-pass edge filter (Semrock, edge wavelength 268.6 nm) was used in front of the UV lens to cut off elastically-scattered laser radiation and other parasitic light. Laser and camera were synchronized with the passage of the shock wave using the delay generator triggered by the signal of the incident wave recorded by the third pressure transducer (cf. Fig. 11). The desired times to release a laser pulse are calculated from the incident and reflected shock-wave velocities and the intrinsic delay of the trigger system.

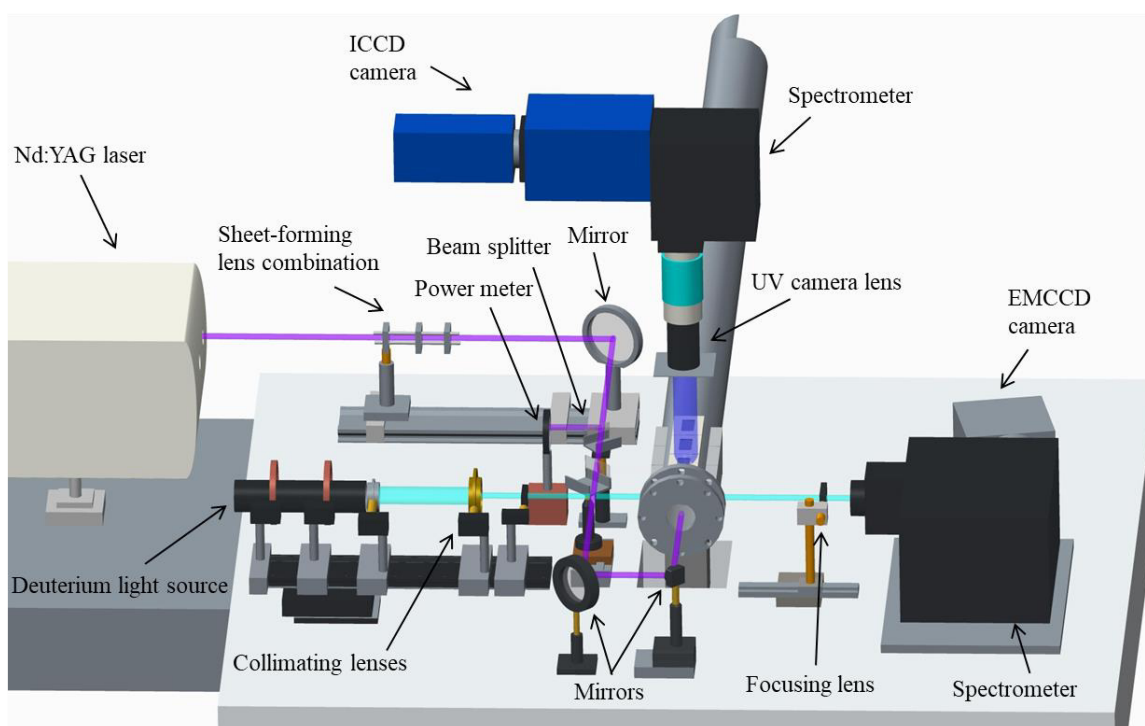


Fig. 60: Experimental arrangement for spectrally- and reaction-time-resolved LIF and simultaneous time-resolved UV-absorption measurements.

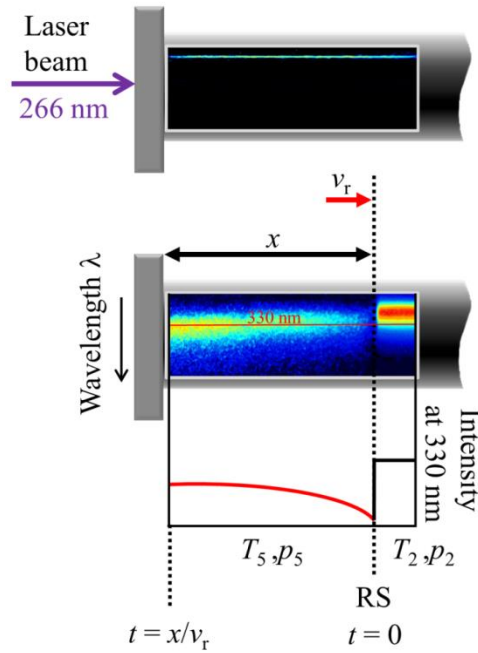


Fig. 61: Typical measurements with the RTR-LIF setup. Top: Elastic scattering of laser light at 266 nm with the shock tube filled with N_2 (detected without long-pass filter). Bottom: Fluorescence signal of anisole at $T_2 = 750$ K, $p_2 = 0.7$ bar and $T_5 = 1350$ K, $p_5 = 2.5$ bar (with long-pass filter). RS: Reflected shock wave v_r : reflected shock velocity.

Figure 61 shows examples for spatially- and spectrally resolved measurements with the RTR-LIF setup. The horizontal coordinate represents time t , the vertical coordinate is the wavelength of the fluorescence signal λ . The upper case in Fig. 61 illustrates the laser position in a measurement in nitrogen without the long-pass filter where Rayleigh scattering is detected only at 266 nm. The lower case shows the fluorescence signal of anisole at $T_5 = 1350$ K over the reaction time. If the arrival time of the reflected shock wave at the distance x from the endwall is set as time zero, x/v_r represents the time elapsed for the reactive mixture behind the reflected shock wave at the endwall, where v_r is the velocity of the reflected shock wave. After passage of the reflected shock wave, the temperature of the gas mixture suddenly increases and chemical reactions might be initiated. Both change the fluorescence signal intensity which is detected for every individual wavelength (for example at 330 nm).

x - t transformation in RTR-LIF measurements

The analysis of the RTR-LIF measurements requires both translation of the measured location in reaction times based on the shock-wave velocity and intensity corrections because both the laser beam and the signal light can experience attenuation on their ways through the reacting gas mixture. The latter effects are time (and thus) location dependent. As the simultaneous absorption measurements encompass broad-band absorption spectra over the whole test time, the absolute absorption/transmission for both laser beam attenuation and LIF signal attenuation can be directly obtained from those measurements (cf. Sec. 6.3).

Transforming the axial location of the LIF measurements into time after passage of the reflected shock wave requires information about the velocity of the reflected shock wave v_r and

the location x of the reflected shock wave at the time of the measurement. v_r depends on the initial conditions, i.e., temperature, pressure, and the gas mixture composition. v_r typically assumes values between 200 and 600 m/s for post-reflected-shock temperatures (T_5) between 550 and 2500 K. Figure 62 shows calculated times of the shock arrival as a function of the distance from the endwall for a selection of shock velocities (assumed constant) for typical initial conditions. In this case, there is a linear relationship between x and t , which simplifies the location-to-time transformation of the raw images. Following this procedure, it is possible to transform the time-coordinate into a spatial coordinate, and vice versa. In the same way the fractional absorption images (Fig. 63) can be transformed from the temporal to the spatial scale (e.g., in Fig. 65). It should be noted that due to gas-dynamic effects, the reflected shock velocity is not exactly constant which can lead to minor errors of the location-to-time transformation for longer test times. In the presented experiment, the velocity of the reflected wave was reduced by 3–6% over the first 500 mm as measured with multiple pressure transducers along the test section. Since these measurements, however, were limited to the first 50 mm, the resulting effect is negligible. It should be considered in more detail if the method is applied to locations far away from the end flange.

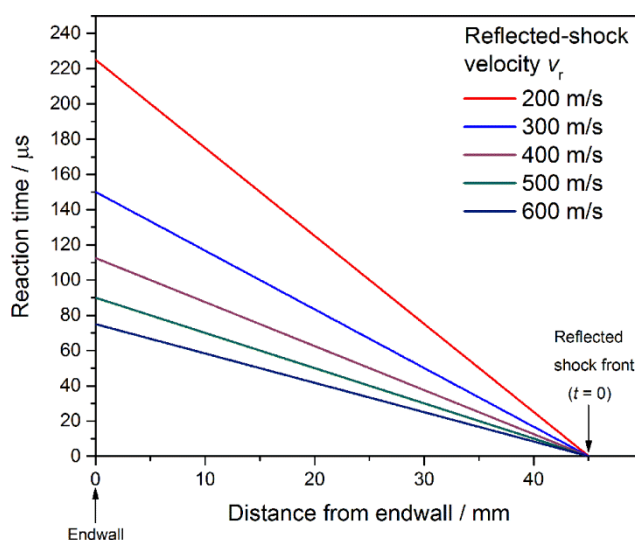


Fig. 62: Reaction time behind the reflected shock wave as a function of distance from the endwall for selected shock-wave velocities v_r . The relationship is shown for a case when while taking the image, the reflected shock front has reached a distance of 45 mm from the endwall. The arrival of the reflected shock defines time zero.

Simultaneous time-resolved absorption experiment

Temporally- and spectrally-resolved absorption measurements were performed simultaneously to the fluorescence measurements (cf. Fig. 60) with the similar arrangement which described in detail in Sec. 4.3.1. Time-resolved absorption spectra provide information about the kinetics of decomposition and product formation and thus allow setting the time range for detection in the RTR-LIF. They also provide the data that is required for correcting the RTR-LIF measurements for laser and signal attenuation at any time (position) and any wavelength. To avoid interference between the fluorescence and the absorption measurement, the laser beam is located slightly above the beam of the D₂ lamp.

At low temperature where no decomposition of anisole is expected, absorption cross-sections $\sigma(\lambda, t) = \sigma(\lambda)$ were described using the Beer–Lambert law (Eq. 4). The baseline I_0 is recorded before filling the driven section with the test gas prior to the experiment, whereas I is measured during the experiment starting shortly before the arrival of the reflected shock wave. The ratiometric measurement of I/I_0 auto-corrects the measurement for potential wavelength-dependent sensitivity of the spectrometer and the camera.

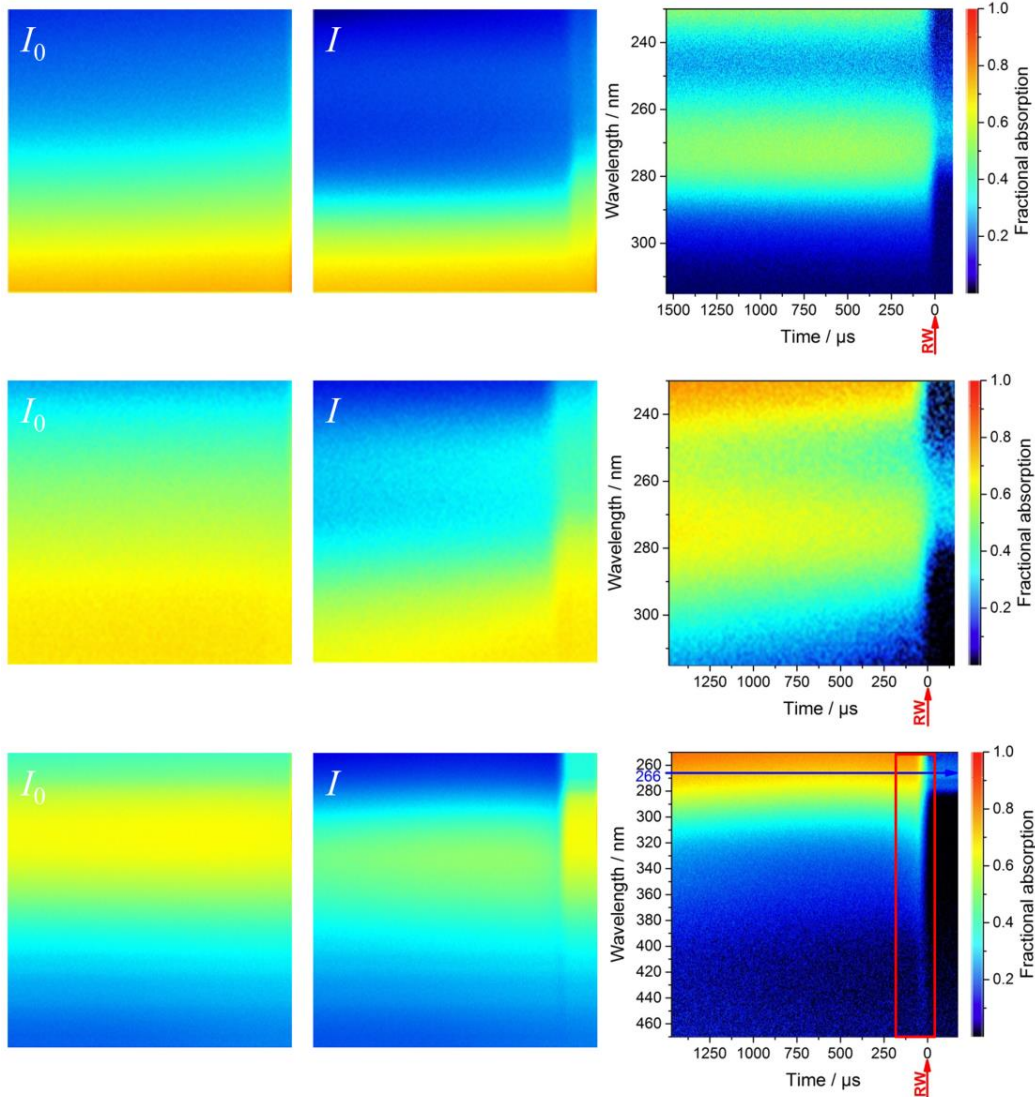


Fig. 63: Absorption–time images for shock-heated anisole in Ar. Left: I_0 measured with the evacuated shock tube, center: transmitted intensity I with spectral and temporal resolution in anisole shortly before and after the arrival of the reflected shock wave. Right: Fractional absorption; the arrival of the reflected shock wave ($t = 0$) at the detection volume is marked by “RW”. Conditions after the reflected shock wave: Top: $T_5 = 860$ K, $p_5 = 1.5$ bar, 0.5 % anisole in Ar. Center: $T_5 = 1100$ K, $p_5 = 2.9$ bar, 0.25 % anisole in Ar. Bottom: $T_5 = 1350$ K, $p_5 = 2.5$ bar, 0.5 % anisole in Ar. In the bottom panel, the detection range for the first two rectangular windows of RTR-LIF is marked as a red box and the blue arrow represents the excitation wavelength at 266 nm. The signal variation along this line provides temporal/spatial variations in laser attenuation in the LIF experiment.

Figure 63 shows example images of $I_0(\lambda)$ and $I(\lambda)$ after background subtraction and fractional absorption $\left(\frac{I_0(\lambda) - I(\lambda, t)}{I_0(\lambda)}\right)$ in the 230–315 nm and 250–470 nm wavelength range. Experiments shown were carried out at $T_5 = 860$ K, $p_5 = 1.5$ bar and 0.5 % anisole in Ar (top), at

$T_5 = 1100$ K, $p_5 = 2.9$ bar and 0.25 % anisole in Ar (center) and at $T_5 = 1350$ K, $p_5 = 2.5$ bar and 0.5 % anisole in Ar (bottom). Note that as a result of the half initial concentration and a double pressure behind the reflected shock wave, the number density in the top and the center row experiments is nearly the same. Due to the sudden increase in number density of the absorbing species behind the reflected shock wave, the passage of the reflected shock waves (RW) at time zero causes a strong change in the signal in all experiments.

At 860 K, where anisole is stable, the absorption spectrum remains constant behind the reflected shock wave (upper panel). At 1100 K and 1350 K, anisole starts to undergo thermal decomposition causing variations in the absorption traces over reaction times behind the reflected shock waves, due to the formation of new absorbing species with absorption characteristics that are different from those of anisole (center and bottom panel).

The blue arrow in the lower panel of Fig. 63 indicates the excitation wavelength at 266 nm. From the signal variation along this line, temporal/spatial variation in laser attenuation is determined for corrections of the LIF measurements. The red box shows the spectrally-resolved transmission properties of the gas in area that is typically detected for the first two rectangular optical ports. These values are used to derive corrections for wavelength-dependent signal attenuation in the LIF experiment. Both effects, laser and signal attenuation, must be used to correct the respective RTR-LIF measurements.

6.3. Problems to be solved: Laser and signal attenuation

In the RTR-LIF measurements, the laser beam and the signal light might be attenuated when passing through the reactive mixture. In the general case of non-optically-thin mixtures, the quantitative evaluation of RTR-LIF signals requires the additional knowledge of spatial (i.e., temporal) variabilities of the optical transmission properties of the gas mixture.

The initial concentration of the tracer was kept low (here, 0.25–0.5% anisole in Ar) to mitigate attenuation effects. However, as reported in Sec. 5.2.1, decomposition products can have a significantly larger absorption cross-section than the original tracer that not only leads to an increased attenuation of the laser light but might also attenuate the LIF signal in a wavelength-dependent manner. The magnitude of laser and signal attenuation depends on the post-shock conditions. While at low temperatures the absorption is constant, at high temperature the fractional absorption increases and changes its spectral shape as a result of the build-up of new species. The analysis is based on the assumption that absorbed signal light does not lead to significant secondary fluorescence. Figure 64 introduces the coordinates used below for the description of the attenuation effects.

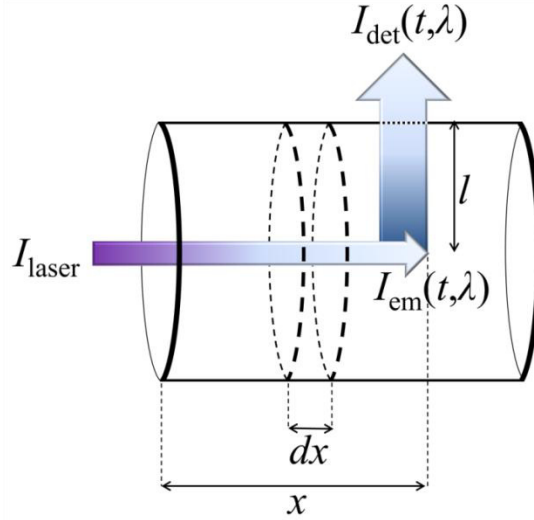


Fig. 64: Schematics of laser and signal attenuation. I_{laser} : Intensity of the incident laser beam; $I_{\text{em}}(t, \lambda)$ and $I_{\text{det}}(t, \lambda)$: emitted LIF intensity at the time (either location) of its generation and detected at the exit optical port, respectively; and x and l are length of absorption of the laser beam and the fluorescence emission, respectively.

Laser attenuation

In cases where laser attenuation on the path through the shock tube is not negligible, corrections for the time- (and thus location-)dependent attenuation at the laser wavelength (here: 266 nm) are required. The local laser beam transmission at time t is determined by Eq. 44 (Fig. 65).

$$T(t) = \frac{I_{\text{laser}}(t)}{I_{\text{laser},0}} = 1 - F(t) = \exp\left(-\int_0^t \alpha_{266 \text{ nm}}(t) dt\right) \quad (44)$$

Where $T(t)$ is the transmission and $F(t)$ is the fractional absorption at time t behind the shock wave. $I_{\text{laser},0}$ is the incident laser light intensity, $I_{\text{laser}}(t)$ is the laser light intensity at time t , dt is the corresponding time interval for the absorption length x , $\alpha(t)$ is the effective local attenuation coefficient. Note that the time and position variables are interchangeable ($dx = v \times dt$). If the gas mixture is stable on the reaction time scale, the rate of attenuation is invariant within the uniform absorption pathway along the tube axis. At high temperatures with decomposition of the molecule (here anisole), variable time- (i.e., location-)dependent transmission must be used instead (cf. Fig. 63).

Figure 65 shows the directly obtained transmission of the light at 266 nm from the absorption measurements for two experimental conditions. At 750 K, anisole is stable on the experimental timescale behind the reflected shock wave and the absorption of the laser light occurs only by molecular anisole leading to an exponential decay in laser intensity along the beam path. In contrast, anisole decomposes at 1350 K and consequently gives rise to the formation of additional species with larger absorption immediately after the arrival of the reflected shock wave. Since the elapsed time behind the shock waves for a similar position varies due to the different shock wave velocities, the time-coordinate is then transformed into a spatial

coordinate in the Fig. 65 – following the procedure given above – for better comparison between experiments at low and high temperatures from the location of the shock front to the end wall. For the data presented in Fig. 65 the maximum laser transmission is at the endwall. At high temperature, the laser beam transmission decreases strongly due to the formation of pyrolysis products that are stronger absorbers than anisole (cf. Sec. 5.2).

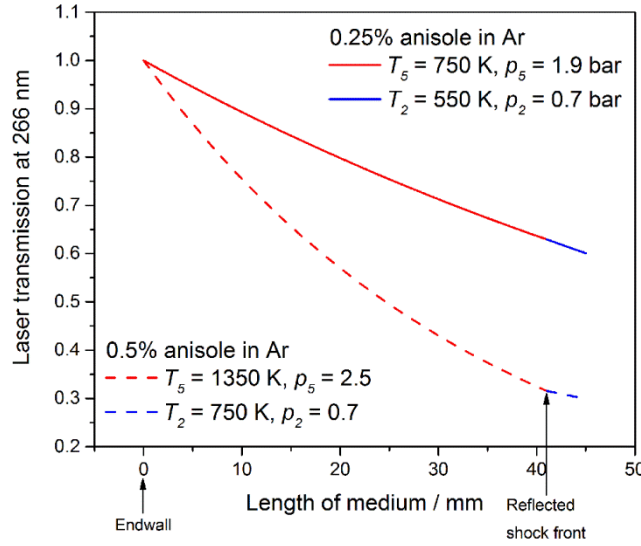


Fig. 65: Evaluation of the local laser (266 nm) intensity along the length of the first optical detection port. The absorption pattern in Fig. 63 was used to determine the light attenuation at 266 nm.

Signal attenuation

Signal attenuation may affect the observed emission intensity and its spectral shape. Without correction, this would result in erroneous values, e.g., if fluorescence quantum yields and fluorescence spectra are evaluated. Therefore, correction factors are required that compensate for the spatially- (i.e. temporally-) and spectrally-dependent signal attenuation. Within the temperature range where the mixture is stable, signal attenuation remains invariant over time and its spectral shape is identical to the absorption spectrum of anisole. At high temperature, however, anisole decomposes; and hence the signal attenuation varies over the spatial scale of the measured signal. The signal attenuation at every position x (i.e., time t) can be corrected using the results of time-resolved absorption measurements for the respective time t . As the absorption generally also varies with wavelength, the correction function can be determined as follows (cf. Fig. 64):

$$I_{\text{em}}(t, \lambda) = \frac{I_{\text{det}}(t, \lambda)}{\exp(-\alpha_{t, \lambda} l)} = \frac{I_{\text{det}}(t, \lambda)}{T(t, \lambda)} \quad (45)$$

$I_{\text{em}}(t, \lambda)$ is the generated fluorescence intensity, $I_{\text{det}}(t, \lambda)$ is the detected fluorescence intensity that reaches to the detector, $\alpha_{t, \lambda}$ is effective attenuation coefficient at time t behind the reflected shock and l is the absorption length between the location of the laser beam and the window and $T(t, \lambda)$ is the transmitted fluorescence light. Figure 66 shows reaction-time-resolved fluo-

rescence spectra of anisole corrected for both laser and signal attenuation. The upper panel of Fig. 66 shows a raw plot of the recorded single-shot fluorescence signal intensity values of anisole in the 250–470 nm region for an experiment at $T_2 = 750$ K and $T_5 = 1350$ K. A combined transmission (middle panel) of the laser beam and the fluorescence signal – which was obtained directly from time-resolved absorption measurements (Sec. 6.2) – provides the correction function for the entire interval behind the incident and the reflected shock.

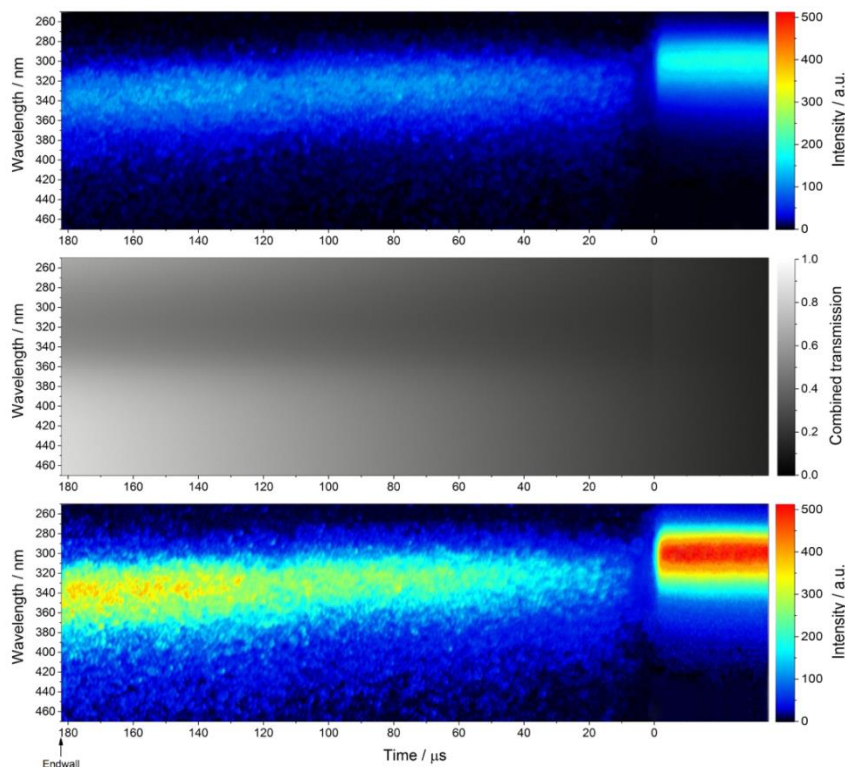


Fig. 66: Correction of an RTR-LIF image. Top: Raw fluorescence spectra of anisole $T_2 = 750$ K, $T_5 = 1350$ K. Center: Combined transmission spectrum obtained from respective measurements of simultaneous time-resolved absorption. Bottom: Corrected fluorescence spectra of anisole.

6.4. Results of RTR-LIF

Figure 67 shows two typical RTR-LIF images for two post-shock conditions without (a) and with (b) anisole decomposition on the time scale of observation. The upper panel of Fig. 67 shows results from an experiment with $T_2 = 550$ K and $T_5 = 750$ K, where anisole is stable. Thus, the fluorescence emission remains almost constant during the high-temperature phase before and behind the arrival of the reflected shock wave. The fluorescence signal intensity is weaker behind the reflected shock wave as a result of the decrease of the fluorescence quantum yield with increasing temperature after the arrival of reflected shock wave ($t = 0$). The timing of the image acquisition can be adjusted giving an exact predetermined delay time as described in the experimental section. To better visualize the spectral variation of the RTR-LIF of anisole with increasing temperature behind incident and reflected shock waves, the spectra were integrated along the spatial coordinate of the acquired image over the entire time and normalized to their respective peak intensities. The fluorescence spectra show a slight

red-shift (about 2.8 nm per 100 K [13]). In contrast, the lower panel of Fig. 67 presents the change of the fluorescence intensity at a high temperature behind the reflected shock wave ($T_5 = 1350$ K). Note that this image was not taken from a single experiment and it has been constructed from two seamlessly concatenated single-shot full-frame images. This was accomplished by taking series of two images from two separate experiments under nominally identical conditions behind the reflected shock with a fixed camera. The extended time profile was achieved by using the window near the endwall and changing the delay time of intensifier gating and probe laser pulses to match the images. An uncertainty of $1 \mu\text{s}$ in the calculated overall time interval from two experiments was estimated in this trace because of the slight variations in the measured reflected shock wave velocities. Images were taken without hardware binning to keep the spatial resolution. The measured wave velocity predicts pre-shock conditions of 750 K and 0.7 bar and post-shock conditions of 1350 K and 2.5 bar. The contribution of fluorescence signal of anisole and/or decomposition products can be separated from the pre and post-shock images. This image was taken $182 \mu\text{s}$ after shock reflection at the endwall.

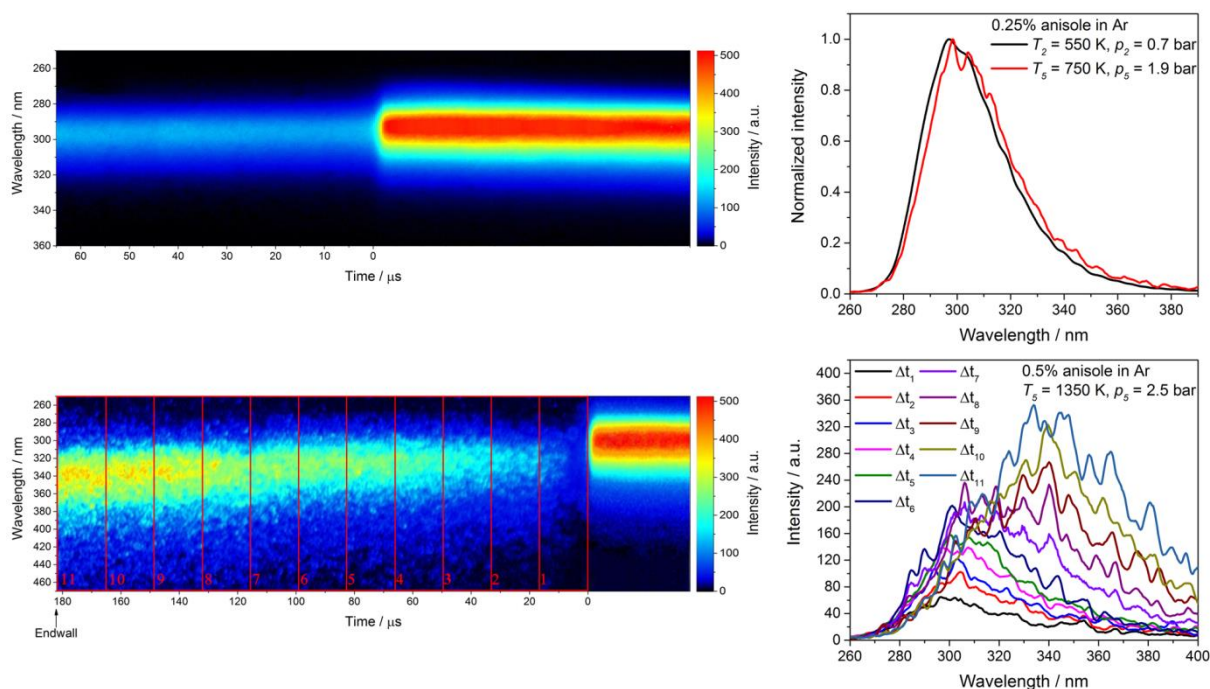


Fig. 67: Reaction-time-resolved LIF spectra of anisole. Upper panel: Low-temperature experiment (without decomposition) and normalized fluorescence emission spectra of anisole integrated over the entire time intervals behind incident and reflected shock waves after excitation at 266 nm. Lower panel: High-temperature measurements (with anisole decomposition) and fluorescence emission spectra of decomposition products measured behind reflected shock wave (integrated for intervals of $\Delta t = 16.5 \mu\text{s}$, red rectangles).

For the conditions behind the incident shock waves, no chemical reactions occur on the time-scale of interest. Therefore, the LIF signal is invariant over the experimental time (far right of the image). Directly behind the reflected shock front, the fluorescence intensity decreases rapidly due to the decrease of the fluorescence quantum yield and decomposition of anisole. Fluorescing products appear almost immediately behind the reflected shock wave as can be

seen from the fluorescence signal. To identify to which extent decomposition products of anisole might contribute to the observed fluorescence signal toward longer reaction times at high temperature, the spectra were integrated for intervals of 16.5 μs . The fluorescence signal increases as a function of reaction time and the spectra shift to the longer wavelength over the reaction time as a result of the build-up of new species. This observation is consistent with the previous study at high temperatures [177] with the conventional arrangement of lasers that – in contrast to the approach used here – required many subsequent shock-tube experiments to reconstruct the time-dependent signal traces. This result can qualitatively be explained by the formation of higher molecular weight species (e.g., naphthalene) with different fluorescence properties than anisole itself. Previous pyrolysis studies [69, 71, 73] and mechanisms [70, 72] of anisole decomposition are consistent with formation of phenoxy, phenol, cresol, cyclopentadiene, benzene, and naphthalene. In the pyrolysis mechanism from Ref. [72], naphthalene was postulated as one of the major pyrolysis products even at very short reaction time. Naphthalene is a strong source of fluorescence signal [39] and a strong absorber.

6.5. Conclusions

A new method for reaction-time-resolved LIF measurements (RTR-LIF) in shock tubes is introduced. Upon excitation of the reactive mixture with a single pulse from a 266-nm laser beam through the transparent endwall, spectrally-resolved LIF images with one-dimensional spatial resolutions are detected by an ICCD camera using a newly-designed test section with multiple optical ports. Reaction times are deduced from the axial location in the shock tube based on the measured shock-wave velocity. The new test section also allows for simultaneous time-resolved UV absorption experiments in conjunction with RTR-LIF measurements. Absorption measurements were performed using a deuterium lamp and a spectrograph coupled to an EMCCD camera with kinetic mode to provide temporally- and spectrally-resolved data. The RTR-LIF measurements are corrected for laser attenuation and fluorescence signal attenuation using the time-resolved absorption measurements.

Anisole was chosen to serve as the fluorescence target to demonstrate RTR-LIF. At low temperatures where test molecules are thermally stable on the timescale of interest, RTR-LIF measurements yield a uniform spectral emission over the entire excitation volume. At high temperatures, however, the profile along the time scale provides information regarding the pyrolysis of anisole and the formation/decomposition of various intermediate species involved in chemical reaction that influence both, absorption and fluorescence properties of the gas mixture. The approach presented here opens up new diagnostics opportunities for time-resolved diagnostics of fast gas-phase reactions that involve fluorescing species.

7. Outlook

The fluorescence signal and fluorescence quantum yield of a tracer depend not only on the temperature and on the excitation wavelength but they are as well a strong function the oxygen partial pressure and to a lesser extent of the total pressure. However, this work focused on the effect of the temperature only. In future work the influence of the other parameters that are relevant for practical applications of LIF diagnostics should also be investigated. One important suggestion for the future work is the implementation of the LIF technique at the high-pressure shock tube to completely study all parameter dependences of LIF of tracers and tracer/fuel mixtures in both inert and oxidizing atmosphere. The high-pressure shock tube available at IVG would be ideal for these measurements. Experiments can be done for different equivalence ratios and at pressures of about 50 bar.

The present work provides validation data for a model-based understanding of the fluorescence properties and the pathways of the initial decomposition reactions for selected tracers in O₂-free environments and reveals the important role of pyrolysis products on the absorption and fluorescence properties. However, the presence of oxygen (quenching) and the interaction of the ignition chemistry of several fuel components can change this situation significantly. It is therefore useful to conduct further studies of fuel/tracer mixtures in the presence of oxygen that are relevant for engine combustion.

One challenge in the experiments in the low-pressure shock tube used in this work is the low volatility of some of the tracers especially those used for Diesel-type fuels. To enable investigation of the tracers with low room-temperature vapor pressure, providing heating sleeves for the entire apparatus, i.e., the shock tube including the mixing vessel and lines would be beneficial. This would allow for heating the entire apparatus before experiments. Thus, for tracers from the classes of higher polycyclic aromatic compounds for example substituted naphthalenes as well higher aliphatic ketones including substituted cyclic ketones, optical properties and gas-phase kinetics could be studied as well.

The photophysical properties at high temperatures are still unknown for many potential tracer species. Spectroscopic information of most formed species at high temperature is scarce and restricted to conditions near room temperature. A realistic modeling of the fractional absorption and the correct quantitative interpretation of LIF signal after the onset of pyrolysis of tracer require the knowledge of the UV absorption cross-sections and fluorescence quantum yield of all respective species at high temperatures.

Strong fluorescence signal from high-temperature decomposition products of tracers (or even from non-fluorescing hydrocarbons) might also provide new diagnostics opportunities as an indicator of the temperature history of a gas volume. Future investigations need to elucidate the potential of the nascent pyrolysis species for diagnostics applications.

8. Conclusions

Tracer-LIF diagnostics based on organic fluorescence tracers is frequently used for imaging measurements of fuel concentration, equivalence ratio, and temperature in combustion processes [5]. Here, a small amount of the tracer is mixed with a non-fluorescing fuel, and its fluorescence intensity after laser excitation is recorded to monitor the distribution of the evaporated fuel from the signal intensity or to obtain information about local temperature and oxygen partial pressure based on relative signal intensities in multi-color measurements [5]. To provide the data required for the quantitative interpretation of the measured signal, absorption cross-sections, fluorescence quantum yields, and fluorescence spectra of various tracer species should be investigated for a wide range of temperature. In modern highly energy-efficient IC engines with high compression ratios or in HCCI engines, however, high in-cylinder temperatures raise concerns about the thermal stability of the tracer throughout the measurement cycle [23]. Under such conditions, the tracer can pyrolyze or oxidize over the observation time scale, which can significantly influence the interpretation of the tracer fluorescence signals. The dependence of photo-physical properties of fluorescence tracers on temperature and pressure in a reaction environment are of great interest for practical tracer-LIF applications.

Shock-tube experiments provide a possibility to observe both signal intensity variation and change of absorption and fluorescence emission spectra on the timescale of a few micro- to milliseconds and at high temperatures. At high temperatures, these studies set a thermal stability limit and show how absorption and fluorescence changes during the decomposition of tracers i.e., the properties of the decomposition products. This observation is essential to suggest detection schemes for selective detection of tracer fluorescence in reactive high-temperature environments where detection aims at imaging with band-pass filters rather than on point measurements. Determining the stability of the pure tracer also allows to develop and to improve the knowledge about the chemical elementary steps leading to the consumption of the tracer at high temperatures [66, 177]. Developing a mechanistic understanding complements the experimental investigations and provides a means for a more quantitative analysis of the measured data. The investigation of the reactions of the pure tracers also builds up a knowledge base for subsequent coupling of the kinetics mechanisms of tracer and fuel.

The high fluorescence quantum yields as well as the large absorption cross-sections in the UV range make single-ring aromatic compounds (e.g., toluene, anisole, XLs and TMBs) attractive as fluorescence tracer for LIF imaging diagnostics.

Toluene is frequently used as fluorescence tracer in high-temperature combustion applications. Using spectrally- and temporally-resolved ultraviolet absorption and LIF measurements, the spectral properties of toluene and its pyrolysis products was studied behind shock waves between 810 and 1755 K. Temperature dependence of absorption spectra were acquired between 220–300 nm. The temporal behavior of the absorption at 266 nm was compared to sim-

ulations based on literature kinetics models of toluene pyrolysis and available high-temperature absorption cross-sections of toluene, benzyl radicals, and C_7H_6 as a product from benzyl decomposition. Experiment and simulation agree well at the beginning of the pyrolysis process, whereas for longer reaction times deviations occur presumably due to the build-up of high-molecular-weight species, which contribute to the observed absorption but have unknown spectral properties. Additionally, LIF emission spectra were recorded following 266 nm excitation at selected reaction times. From measurements up to 1220 K, the relative fluorescence quantum yield of toluene was derived, extending existing data to higher temperatures. Products from toluene pyrolysis were found to be the major contributors to the LIF signal at higher temperatures.

Anisole has previously been identified as a fluorescence tracer for fuel/air mixing studies based on LIF that provides stronger signal than the frequently-used toluene [39]. In this work, ultraviolet absorption and LIF of anisole were measured as a function of time in shock-heated gases at temperatures between 565 and 1620 K and at pressures of 1.3 and 2.9 bar. Absorption spectra were acquired with ~ 50 μs time resolution in the 240–310 nm spectral range. LIF emission spectra of anisole were recorded at different fixed reaction times behind reflected shock waves using 266-nm laser excitation. Relative fluorescence quantum yields were determined that extend previously reported data beyond 980 K. After the onset of pyrolysis of anisole at $T > 1000$ K, effective absorption cross-sections and the corresponding LIF signals after 266-nm excitation were reported. To aid the interpretation of these experiments, the products of anisole pyrolysis were investigated using a shock tube coupled to a high-resolution TOF-MS for time-resolved multispecies measurements. Concentration-time profiles for anisole and products such as benzene, C_2H_4 , and CO were measured and compared to simulations using two kinetics models from literature.

para-xylene (p-XL) and 1,2,4-trimethylbenzene (1,2,4-TMB) are two of the less studied aromatic tracers that are naturally present in commercial fuels. In this work, the temperature dependence of ultraviolet absorption of p-XL and 1,2,4-TMB has been studied in the gas phase from room temperature up to 1605 K. Absorption cross-sections of p-XL and 1,2,4-TMB have been measured and the thermal stability of these species has been determined. Time-resolved UV-absorption measurements of the initial decomposition species of p-XL and 1,2,4-TMB were compared to model results from literature. In addition, the fluorescence properties of p-XL and 1,2,4-TMB before pyrolysis were investigated using 266 nm laser excitation. The fluorescence intensity of both tracers decreases significantly with increasing temperature. Using the data of absorption cross-section and the fluorescence signal for a given excitation wavelength, the fluorescence quantum yields of p-XL and 1,2,4-TMB were determined for a wide temperature range.

Acetylene as a major intermediate in fuel pyrolysis and combustion has so far mostly been ignored as a contributor to UV absorption and fluorescence. Temperature-dependent ultraviolet absorption cross-sections of C_2H_2 have been studied behind reflected shock waves between

565 and 1500 K. Light from a deuterium lamp was transmitted through shock-heated gas mixtures and transmission spectra were recorded. The absorption spectra strongly depend on temperature and show a strong red-shift with temperature. Above 900 K, significant absorption is observed at 266 nm. LIF spectra were recorded in the shock tube using 266-nm laser excitation. In accord with absorption experiments, no LIF signal is observed below 900 K. Above, the fluorescence intensity increases and the fluorescence spectra become broader over the studied temperature range. From fluorescence intensity and absorption cross-sections, relative effective fluorescence quantum yields are determined as a function of temperature.

Shock tubes allow for the study ultra-fast gas-phase reactions on the microsecond time scale. Because the repetition rate of the experiments is low, it is crucial to gain as much information as possible from each individual measurement. While reaction-time-resolved species concentration and temperature measurements with fast absorption methods are established, conventional LIF measurements with pulsed lasers provide data only at a single reaction time. Therefore, fluorescence methods have rarely been used in shock-tube diagnostics. This work delivers a novel experimental concept that allows reaction-time-resolved LIF measurements with one single laser pulse using a test section that is equipped with several optical ports. After the passage of the shock wave, the reactive mixture is excited along the center of the tube with a 266-nm laser beam directed through a window in the endwall of the shock tube. The emitted LIF signal is collected through elongated sidewall windows and focused onto the entrance slit of an imaging spectrometer coupled to an intensified CCD camera. The one-dimensional spatial resolution of the measurement translates into a reaction-time-resolved measurement while species information can be gained from the spectral axis of the detected two-dimensional image. Anisole pyrolysis was selected as benchmark reaction to demonstrate the new apparatus.

This work provides a large amount of new data and improved understanding of optical properties and reaction kinetics of various gas-phase tracers for quantitative laser-induced fluorescence. The measurement strategy was based on temporally- and spectrally-resolved UV absorption and LIF. In combination with kinetics models from literature, an enhanced analysis of thermal stability and the gas-phase kinetics of the respective tracers at high temperature was obtained. Within this work, a novel experimental concept of RTR-LIF measurements in shock tubes was introduced that enables fluorescence measurements at various reaction times with a single laser pulse after the passage of the reflected shock wave. The new data as well as the new experimental concept will have important impact on the quantitative diagnostics with tracer LIF under high-temperature conditions.

9. List of own publications

Peer-reviewed publications

1. S. Zabeti, A. Drakon, S. Faust, T. Dreier, O. Welz, M. Fikri, C. Schulz, “Temporally- and spectrally-resolved UV absorption and laser-induced fluorescence measurements during the pyrolysis of toluene behind reflected shock waves”, *Applied Physics B* 118 (2015) 295–307
2. S. Zabeti, M. Aghsaee, M. Fikri, O. Welz, C. Schulz, “Optical properties and pyrolysis of shock-heated gas-phase anisole”, *Proceedings of the Combustion Institute* 36 (2017) 4525–4532
3. S. Zabeti, M. Fikri, C. Schulz, “Ultraviolet absorption and laser-induced fluorescence of shock-heated acetylene”, *Proceedings of the Combustion Institute* 36 (2017) 4469–4475
4. S. Zabeti, M. Fikri, C. Schulz, “Reaction-time-resolved measurements of laser-induced fluorescence in a shock tube with a single laser pulse”, *Review of Scientific Instruments* 88 (2017) 115105

Conference contributions

1. S. Zabeti, S. Faust, T. Dreier, M. Fikri, C. Schulz, “High-temperature shock tube study of laser-induced fluorescence of toluene and its pyrolysis products”, 8th International Seminar on Flame Structure, September 21–24, 2014, Berlin, Germany, Talk
2. S. Zabeti, M. Aghsaee, M. Fikri, O. Welz, C. Schulz, “A high-temperature shock-tube study on the optical properties and pyrolysis of anisole”, 7th European Combustion Meeting, March 30 – April 2, 2015, Budapest, Hungary, Poster
3. T. Endres, S. Zabeti, T. Dreier, C. Schulz, “Absorption cross section of anisole from room- to combustion-relevant temperatures: Problem of under resolved tracer absorption-spectra”, Gordon Research Conference Laser Diagnostics in Combustion, August 9 – 14, 2015, Waterville Valley, NH, US, Poster
4. S. Zabeti, M. Aghsaee, M. Fikri, O. Welz, C. Schulz, “Optical properties and pyrolysis of shock-heated gas-phase anisole”, 36th International Symposium on Combustion, July 31 – August 5, 2016, Seoul, Korea, Talk
5. S. Zabeti, M. Fikri, C. Schulz, “Ultraviolet absorption and laser-induced fluorescence of shock-heated acetylene”, 36th International Symposium on Combustion, July 31 – August 5, 2016, Seoul, Korea, Talk
6. S. Zabeti, M. Fikri, C. Schulz, “New concept for simultaneous measurement of laser-induced fluorescence in a shock tube at variable reaction times”, 36th International Symposium on Combustion, July 31 – August 5, 2016, Seoul, Korea, Poster

10. References

- [1] IEA, World Energy Outlook 2017, 2017.
- [2] EIA, International Energy Outlook 2016, 2016.
- [3] EIA, International Energy Outlook 2017, U.S. Energy Information Administration, 2017.
- [4] K. Kohse-Höinghaus, J.B. Jeffries (Eds), Applied Combustion Diagnostics, Taylor and Francis, New York, 2002.
- [5] C. Schulz, V. Sick, Tracer-LIF diagnostics: quantitative measurement of fuel concentration, temperature and fuel/air ratio in practical combustion systems, Prog. Energy Combust. Sci., 31 (2005) 75-121.
- [6] T. Fansler, D. French, M. Drake, Fuel Distributions in a Firing Direct-Injection Spark-Ignition Engine Using Laser-Induced Fluorescence Imaging, SAE Technical Paper Series 950110, (1995).
- [7] S.A. Kaiser, M. Schild, C. Schulz, Thermal stratification in an internal combustion engine due to wall heat transfer measured by laser-induced fluorescence, Proc. Combust. Inst., 34 (2013) 2911-2919.
- [8] F. Großmann, P.B. Monkhouse, M. Ridder, V. Sick, J. Wolfrum, Temperature and pressure dependencies of the laser-induced fluorescence of gas-phase acetone and 3-pentanone, Appl. Phys. B, 62 (1996) 249-253.
- [9] J.D. Koch, R.K. Hanson, W. Koban, C. Schulz, Rayleigh-calibrated fluorescence quantum yield measurements of acetone and 3-pentanone, Appl. Opt., 43 (2004) 5901-5910.
- [10] J. Trost, L. Zigan, S.C. Eichmann, T. Seeger, A. Leipertz, Investigation of the chemical stability of the laser-induced fluorescence tracers acetone, diethylketone, and toluene under IC engine conditions using Raman spectroscopy, Appl. Opt., 52 (2013) 6300-6308.
- [11] S. Faust, G. Tea, T. Dreier, C. Schulz, Temperature, pressure, and bath gas composition dependence of fluorescence spectra and fluorescence lifetimes of toluene and naphthalene, Appl. Phys. B, 110 (2013) 81-93.
- [12] W. Koban, J.D. Koch, R.K. Hanson, C. Schulz, Absorption and fluorescence of toluene vapor at elevated temperatures, Phys. Chem. Chem. Phys., 6 (2004) 2940-2945.
- [13] S. Faust, T. Dreier, C. Schulz, Photo-physical properties of anisole: temperature, pressure, and bath gas composition dependence of fluorescence spectra and lifetimes, Appl. Phys. B, 112 (2013) 203-213.

- [14] K.H. Tran, C. Morin, M. Kühni, P. Guibert, Fluorescence spectroscopy of anisole at elevated temperatures and pressures, *Appl. Phys. B*, 115 (2014) 461-470.
- [15] M.C. Thurber, R.K. Hanson, Pressure and composition dependences of acetone laser-induced fluorescence with excitation at 248, 266, and 308 nm, *Appl. Phys. B*, 69 (1999) 229-240.
- [16] S. Faust, T. Dreier, C. Schulz Temperature and bath gas composition dependence of effective fluorescence lifetimes of toluene excited at 266 nm, *J. Chem. Phys.*, 383 (2011) 6-11.
- [17] W. Koban, J.D. Koch, R.K. Hanson, C. Schulz Toluene LIF at elevated temperatures: Implications for fuel/air ratio measurements, *Appl. Phys. B*, 80 (2005) 147-150.
- [18] J.D. Koch, R.K. Hanson, Temperature and excitation wavelength dependencies of 3-pentanone absorption and fluorescence for PLIF applications, *Appl. Phys. B*, 76 (2003) 319-324.
- [19] V. Sick, C.K. Westbrook, Diagnostic implications of the reactivity of fluorescence tracers, *Proc. Combust. Inst.*, 32 (2009) 913–920.
- [20] P. Tröndle, R. Schießl, U. Maas, Studies on the interference of nascent acetone to tracer LIF in IC-engines, *Proc. of the Fifth European Combustion Meeting Cardiff*, 2011.
- [21] M. Richter, J. Engström, A. Franke, M. Aldén, A. Hultqvist, B. Johansson, The Influence of Charge Inhomogeneity on the HCCI Combustion Process, *SAE Technical Paper Series 2000-01-2868*, (2000).
- [22] C. Schulz, J. Gronki, S. Andersson, Multi-species laser-based imaging measurements in a Diesel spray, *SAE Technical Paper Series 2004-01-1917*, (2004).
- [23] N. Graf, J. Gronki, C. Schulz, T. Baritaud, J. Chernel, P. Duret, J. Lavy, In-Cylinder Combustion Visualization in an Auto-Igniting Gasoline Engine using Fuel Tracer- and Formaldehyde-LIF Imaging, *SAE Technical Paper Series 2001-01-1924*, (2001).
- [24] M. Fikri, L.R. Cancino, M. Hartmann, C. Schulz, High-pressure shock-tube investigation of the impact of 3-pentanone on the ignition properties of primary reference fuels, *Proc. Combust. Inst.*, 34 (2013) 393–400.
- [25] M. Hartmann, I. Gushterova, M. Fikri, C. Schulz, R. Schießl, U. Maas, Auto-ignition of toluene-doped n-heptane and iso-octane/air mixtures: High-pressure shock-tube experiments and kinetics modeling, *Combust. Flame*, 158 (2011) 172-178.
- [26] B.K. Sharma, *Spectroscopy*, 20th ed. ed., Krishna Prakashan Media (P) Ltd., Meerut, India, 2007.
- [27] B. Valeur, *Molecular fluorescence : principles and applications*, Wiley-VCH, Weinheim ; New York, 2002.

- [28] S. Faust, Characterisation of organic fuel tracers for laser-based quantitative diagnostics of fuel concentration, temperature, and equivalence ratio in practical combustion processes, PhD thesis, University of Duisburg-Essen, Duisburg, 2013.
- [29] P.W. Atkins, C.A. Trapp, J. De Paula, Physical chemistry, Oxford Univ. Press, Oxford, 2006.
- [30] A. Cessou, U. Meier, D. Stepowski, Applications of planar laser induced fluorescence in turbulent reacting flows, *Meas. Sci. Technol.*, 11 (2000) 887-901.
- [31] A. Hoffmann, F. Zimmermann, H. Scharr, S. Krömker, C. Schulz, Instantaneous three-dimensional visualization of concentration distributions in turbulent flows with crossed-plane laser-induced fluorescence imaging, *Appl. Phys. B*, 80 (2005) 125-131.
- [32] J. Yoo, D. Mitchell, D.F. Davidson, R.K. Hanson, Planar laser-induced fluorescence imaging in shock tube flows, *Exp. Fluids*, 49 (2010) 751-759.
- [33] A.C. Eckbreth, Laser diagnostics for combustion temperature and species. - 2. ed. [compl. rev. and updated], Gordon & Breach, Amsterdam, 1996.
- [34] I.S. Zaslonko, Energy exchange and reactions of highly excited polyatomic molecules, *Russian Chemical Reviews*, 66 (1997) 483-507.
- [35] P. Sulzer, K. Wieland, Intensitätsverteilung eines kontinuierlichen Absorptionsspektrums in Abhängigkeit von Temperatur und Wellenzahl, *Helv. Phys. Acta.*, 25 (1952) 653-676
- [36] L. Brower, J. Troe, Shock wave study of the UV spectrum of CF₃I, *Chem. Phys. Lett.*, 82 (1981) 1-4.
- [37] D.C. Astholz, L. Brouwer, J. Troe, High Temperature Ultraviolet Absorption Spectra of Polyatomic Molecules in Shock Waves, *Ber. Bunsenges. Phys. Chem.*, 85 (1981) 559-564.
- [38] H. Hippler, J. Troe, H.J. Wendelken, UV absorption spectra of vibrationally highly excited toluene molecules, *J. Chem. Phys.*, 78 (1983) 5351-5357.
- [39] S. Faust, M. Goschütz, S.A. Kaiser, T. Dreier, C. Schulz, A comparison of selected organic tracers for quantitative scalar imaging in the gas phase via laser-induced fluorescence, *Appl. Phys. B*, 117 (2014) 183-194.
- [40] B. Rossow, Photophysical processes of organic fluorescent molecules and kerosene – applications to combustion engines, PhD thesis, Institut des Sciences Moléculaires d'Orsay, Université Paris-Sud, Paris, 2011.
- [41] T. Benzler, S. Faust, T. Dreier, C. Schulz, Low-pressure effective fluorescence lifetimes and photo-physical rate constants of one- and two-ring aromatics, *Appl. Phys. B*, 121 (2015) 549-558.

- [42] T. Benzler, T. Endres, T. Dreier, C. Schulz, Temperature, pressure, and oxygen quenching behavior of fluorescence spectra and lifetimes of gas-phase o-xylene and 1,2,4-trimethylbenzene, *Appl. Phys. B*, 124 (2018) 70.
- [43] P. Vieille, Sur les discontinuités produites par la détente brusque de gaz comprimés, *Compt. rend.*, 129 (1899) 1228–1230.
- [44] A.G. Gaydon, I.R. Hurlle, *The Shock Tube in High-Temperature Chemical Physics*, Chapman and Hall, London, 1963.
- [45] K.-Y. Lam, W. Ren, Z. Hong, D.F. Davidson, R.K. Hanson, Shock tube measurements of 3-pentanone pyrolysis and oxidation, *Combust. Flame*, 159 (2012) 3251-3263.
- [46] K.-Y. Lam, W. Ren, S.H. Pyun, A. Farooq, D.F. Davidson, R.K. Hanson, Multi-species time-history measurements during high-temperature acetone and 2-butanone pyrolysis, *Proc. Combust. Inst.*, 34 (2013) 607-615.
- [47] R.C. Tolman, *Statistical mechanics with applications to physics and chemistry*, The Chemical catalog company, Inc., New York, 1927.
- [48] J. Trost, L. Zigan, A. Leipertz, D. Sahoo, P.C. Miles, Fuel concentration imaging inside an optically accessible diesel engine using 1-methylnaphthalene planar laser-induced fluorescence, *Int. J. Engine Res.*, 15 (2014) 741-750.
- [49] S. Einecke, C. Schulz, V. Sick, Measurement of temperature, fuel concentration and equivalence ratio fields using tracer LIF in IC engine combustion, *Appl. Phys. B*, 71 (2000) 717-723.
- [50] C. Gessenhardt, C. Schulz, S.A. Kaiser, Endoscopic temperature imaging in a four-cylinder IC engine via two-color toluene fluorescence, *Proc. Combust. Inst.*, 35 (2015) 3697-3705.
- [51] B. Hiller, R.K. Hanson, Properties of the iodine molecule relevant to laser-induced fluorescence experiments in gas flows, *Exp. Fluids*, 10 (1990) 1-11.
- [52] D.G. Fletcher, J.C. McDaniel, Temperature measurement in a compressible flow field using laser-induced iodine fluorescence, *Opt Lett.*, 12 (1987).
- [53] T.N. Rao, S.S. Collier, J.G. Calvert, Quenching reactions of the first excited singlet and triplet states of sulfur dioxide with oxygen and carbon dioxide, *J. Am. Chem. Soc.*, 91 (1969) 1616-1621.
- [54] V. Sick, Exhaust-gas imaging via planar laser-induced fluorescence of sulfur dioxide, *Appl. Phys. B*, 74 (2002) 461-463.
- [55] W.G. Bessler, M. Hofmann, F. Zimmermann, G. Suck, J. Jakobs, S. Nicklitzsch, T. Lee, J. Wolfrum, C. Schulz, Quantitative in-cylinder NO-LIF imaging in a realistic gasoline engine with spray-guided direct injection, *Proc. Combust. Inst.*, 30 (2005) 2667-2674.

- [56] Y.R. Hicks, R.J. Locke, R.C. Anderson, Laser-Based Flowfield Imaging in a Lean Premixed Prevaporized Sector Combustor, NASA/TM—2005-213402, (2005).
- [57] P. Guibert, V. Modica, C. Morin, Influence of pressure, temperature and gas phase composition on biacetyl laser-induced fluorescence, *Exp. Fluids*, 40 (2005) 245-256.
- [58] B. Peterson, E. Baum, B. Böhm, V. Sick, A. Dreizler, High-speed PIV and LIF imaging of temperature stratification in an internal combustion engine, *Proc. Combust. Inst.*, 34 (2013) 3653-3660.
- [59] J. Snyder, N. Dronniou, J. Dec, R. Hanson, PLIF Measurements of Thermal Stratification in an HCCI Engine under Fired Operation, SAE Technical Paper Series 2011-01-1291, (2011).
- [60] J.D. Koch, J. Gronki, R.K. Hanson, Measurements of near-UV absorption spectra of acetone and 3-pentanone at high temperatures, *J. Quant. Spectrosc. Radiat. Transfer*, 109 (2008) 2037-2044.
- [61] H.-P.S. Shen, M.A. Oehlschlaeger, The autoignition of C₈H₁₀ aromatics at moderate temperatures and elevated pressures, *Combust. Flame*, 156 (2009) 1053-1062.
- [62] W. Koban, J.D. Koch, R.K. Hanson, C. Schulz, Oxygen quenching of toluene fluorescence at elevated temperatures, *Appl. Phys. B*, 80 (2005) 777-784.
- [63] A. Matsugi, A. Miyoshi, Modeling of two- and three-ring aromatics formation in the pyrolysis of toluene, *Proc. Combust. Inst.*, 34 (2013) 269–277.
- [64] M. Derudi, D. Polino, C. Cavallotti, Toluene and benzyl decomposition mechanisms: elementary reactions and kinetic simulations, *Phys. Chem. Chem. Phys.*, 13 (2011) 21308-21318.
- [65] S.J. Klippenstein, L.B. Harding, Y. Georgievskii, On the formation and decomposition of C₇H₈, *Proc. Combust. Inst.*, 31 (2007) 221-229.
- [66] M.A. Oehlschlaeger, D.F. Davidson, R.K. Hanson, Thermal decomposition of toluene: Overall rate and branching ratio, *Proc. Combust. Inst.*, 31 (2007) 211–219.
- [67] T. Hirasawa, T. Kaneba, Y. Kamata, K. Muraoka, Y. Nakamura, Temperature dependence of intensities of laser-induced fluorescences of ethylbenzene and naphthalene seeded in gas flow at atmospheric pressure, *J. Vis.*, 10 (2007) 197-206.
- [68] N. Pasquier, B. Lecordier, M. Trinité, A. Cessou, An experimental investigation of flame propagation through a turbulent stratified mixture, *Proc. Combust. Inst.*, 31 (2007) 1567-1574.
- [69] A.V. Friderichsen, E.-J. Shin, R.J. Evans, M.R. Nimlos, D.C. Dayton, G.B. Ellison, The pyrolysis of anisole (C₆H₅OCH₃) using a hyperthermal nozzle, *Fuel*, 80 (2001) 1747-1755.

- [70] E.B. Hemings, G. Bozzano, M. Dente, E. Ranzi, Detailed kinetics of the pyrolysis and oxidation of anisole, *Chem. Eng. Trans.*, 24 (2011) 61-66.
- [71] C.Y. Lin, M.C. Lin, Thermal decomposition of methyl phenyl ether in shock waves - the kinetics of phenoxy radical reactions, *J. Phys. Chem.*, 90 (1986) 425-431.
- [72] M. Nowakowska, O. Herbinet, A. Dufour, P.-A. Glaude, Detailed kinetic study of anisole pyrolysis and oxidation to understand tar formation during biomass combustion and gasification, *Combust. Flame*, 161 (2014) 1474-1488.
- [73] A.M. Scheer, C. Mukarakate, D.J. Robichaud, G.B. Ellison, M.R. Nimlos, Radical Chemistry in the Thermal Decomposition of Anisole and Deuterated Anisoles: An Investigation of Aromatic Growth, *J. Phys. Chem. A*, 114 (2010) 9043-9056.
- [74] Q. Wang, Y. Zhang, L. Jiang, D. Zhao, P. Guibert, S. Yang, Fluorescence and absorption characteristics of p-xylene: applicability for temperature measurements, *Appl. Phys. B*, 123 (2017).
- [75] F. Battin-Leclerc, R. Bounaceur, N. Belmekki, P.A. Glaude, Experimental and modeling study of the oxidation of xylenes, *Int. J. Chem. Kinet.*, 38 (2006) 284-302.
- [76] G. Bikas, Kinetic mechanisms for Hydrocarbon Ignition, PhD thesis, Institut für Technische Mechanik, RWTH Aachen University, Aachen, 2001.
- [77] S. Honnet, K. Seshadri, U. Niemann, N. Peters, A surrogate fuel for kerosene, *Proc. Combust. Inst.*, 32 (2009) 485-492.
- [78] A. Roubaud, O. Lemaire, R. Minetti, L.R. Sochet, High pressure auto-ignition and oxidation mechanisms of o-xylene, o-ethyltoluene, and n-butylbenzene between 600 and 900 K, *Combust. Flame*, 123 (2000) 561-571.
- [79] A. Roubaud, R. Minetti, L.R. Sochet, Oxidation and combustion of low alkylbenzenes at high pressure: comparative reactivity and auto-ignition, *Combust. Flame*, 121 (2000) 535-541.
- [80] S. Gail, P. Dagaut, OXIDATION OF m-XYLENE IN A JSR: EXPERIMENTAL STUDY AND DETAILED CHEMICAL KINETIC MODELING, *Combust. Sci. Technol.*, 179 (2007) 813-844.
- [81] S. Gail, P. Dagaut, Experimental kinetic study of the oxidation of -xylene in a JSR and comprehensive detailed chemical kinetic modeling, *Combust. Flame*, 141 (2005) 281-297.
- [82] S. Gail, P. Dagaut, G. Black, J.M. Simmie, Kinetics of 1,2-Dimethylbenzene Oxidation and Ignition: Experimental and Detailed Chemical Kinetic Modeling, *Combust. Sci. Technol.*, 180 (2008) 1748-1771.
- [83] J.L. Emdee, K. Brezinsky, I. Glassman, High-temperature oxidation mechanisms of m- and p-xylene, *J. Phys. Chem.*, 95 (1991) 1626-1635.

- [84] J.A. Barnard, B.M. Sankey, The slow combustion of the isomeric xylenes I—Meta- and para-xylene, *Combust. Flame*, 12 (1968) 345-352.
- [85] J.A. Barnard, B.M. Sankey, The slow combustion of the isomeric xylenes II—Ortho-xylene, *Combust. Flame*, 12 (1968) 353-359.
- [86] F. Hildenbrand, C. Schulz, E. Wagner, V. Sick, Investigation of spatially resolved light absorption in a spark-ignition engine fueled with propane/air, *Appl. Opt.*, 38 (1999) 1452-1458.
- [87] F. Hildenbrand, C. Schulz, Measurements and simulation of in-cylinder UV-absorption in spark ignition and Diesel engines, *Appl. Phys. B*, 73 (2001) 173-180.
- [88] F. Hildenbrand, C. Schulz, J. Wolfrum, F. Keller, E. Wagner, Laser diagnostic analysis of soot formation in a direct injection diesel engine with pump-line-nozzle and common rail injection systems, *Proc. Combust. Inst.*, 28 (2000) 1137-1143.
- [89] C. Schulz, J.D. Koch, D.F. Davidson, J.B. Jeffries, R.K. Hanson, Ultraviolet absorption spectra of shock-heated carbon dioxide and water between 900 and 3050 K, *Chem. Phys. Lett.*, 355 (2002) 82-88.
- [90] J.B. Jeffries, C. Schulz, D.W. Mattison, M.A. Oehlschlaeger, W.G. Bessler, T. Lee, D.F. Davidson, R.K. Hanson, UV absorption of CO₂ for temperature diagnostics of hydrocarbon combustion applications, *Proc. Combust. Inst.*, 30 (2005) 1591-1599.
- [91] S. Zabeti, A. Drakon, S. Faust, T. Dreier, O. Welz, M. Fikri, C. Schulz, Temporally and spectrally resolved UV absorption and laser-induced fluorescence measurements during the pyrolysis of toluene behind reflected shock waves, *Appl. Phys. B*, 118 (2015) 295-307.
- [92] D.J. Hucknall, *Chemistry of Hydrocarbon Combustion*, Chapman and Hall New York 1985.
- [93] M. Frenklach, Reaction mechanism of soot formation in flames, *Phys. Chem. Chem. Phys.*, 4 (2002) 2028-2037.
- [94] N.E. Sánchez, A. Callejas, A. Millera, R. Bilbao, M.U. Alzueta, Formation of PAH and soot during acetylene pyrolysis at different gas residence times and reaction temperatures, *Energy*, 43 (2012) 30-36.
- [95] Y. Bénilan, N. Smith, A. Jolly, F. Raulin, The long wavelength range temperature variations of the mid-UV acetylene absorption coefficient, *Planet. Space Sci.*, 48 (2000) 463-471.
- [96] J.K.G. Watson, M. Herman, J.C. Van Craen, R. Colin, The $\tilde{A}-\tilde{X}$ band system of acetylene, *J. Mol. Spectrosc.*, 95 (1982) 101-132.
- [97] L.E. Brus, Acetylene fluorescence, *J. Mol. Spectrosc.*, 75 (1979) 245-250.

- [98] K.K. Innes, Analysis of the Near Ultraviolet Absorption Spectrum of Acetylene, *J. Chem. Phys.*, 22 (1954) 863-876.
- [99] G.A. Raiche, D.R. Crosley, R.A. Copeland, Laser-induced fluorescence and dissociation of acetylene in flames, *AIP Conf. Proc.*, 191 (1989) 758-760.
- [100] J.C. Van Craen, M. Herman, R. Colin, J.K.G. Watson, The $\tilde{A}-\tilde{X}$ band system of acetylene: Analysis of medium-wavelength bands, and vibration-rotation constants for the levels $nv'3$ ($n = 4-6$), $v'2 + nv'3$ ($n = 3-5$), and $v'1 + nv'3$ ($n = 2, 3$), *J. Mol. Spectrosc.*, 111 (1985) 185-197.
- [101] C.K. Ingold, G.W. King, 552. Excited states of acetylene. Part IV. Description and analysis of the near-ultra-violet absorption spectra of acetylene and dideuteroacetylene: nature of the excited state, *J. Chem. Soc.*, (1953) 2725-2744.
- [102] S. Hamai, F. Hirayama, Fluorescence of acetylenic hydrocarbons, *J. Chem. Phys.*, 71 (1979) 2934-2939.
- [103] J.C. Stephenson, J.A. Blazy, D.S. King, Spectroscopy and collisional quenching rates for $A^- C_2H_2$ ($v'3 = 0, 1, 2$), *J. Chem. Phys.*, 85 (1984) 31-38.
- [104] B.A. Williams, J.W. Fleming, Laser-induced fluorescence detection of acetylene in low-pressure propane and methane flames, *Appl. Phys. B*, 75 (2002) 883-890.
- [105] D.L. Osborn, J.H. Frank, Laser-induced fragmentation fluorescence detection of the vinyl radical and acetylene, *Chem. Phys. Lett.*, 349 (2001) 43-50.
- [106] P.C. Miles, B. Li, Z. Li, M. Aldén, Atmospheric Pressure Acetylene Detection by UV Photo-Fragmentation and Induced C2 Emission, *Appl. Spectrosc.*, 67 (2013) 66-72.
- [107] S. Wagner, B.T. Fisher, J.W. Fleming, V. Ebert, TDLAS-based in situ measurement of absolute acetylene concentrations in laminar 2D diffusion flames, *Proc. Combust. Inst.*, 32 (2009) 839-846.
- [108] Z.R. Quine, K.L. McNesby, Acetylene measurement in flames by chirp-based quantum cascade laser spectrometry, *Appl. Opt.*, 48 (2009) 3075-3083.
- [109] S. Wagner, M. Klein, T. Kathrotia, U. Riedel, T. Kissel, A. Dreizler, V. Ebert, In situ TDLAS measurement of absolute acetylene concentration profiles in a non-premixed laminar counter-flow flame, *Appl. Phys. B*, 107 (2012) 585-589.
- [110] I. Stranic, R.K. Hanson, Laser absorption diagnostic for measuring acetylene concentrations in shock tubes, *J. Quant. Spectrosc. Radiat. Transf.*, 142 (2014) 58-65.
- [111] K.C. Utsav, E.F. Nasir, A. Farooq, A mid-infrared absorption diagnostic for acetylene detection, *Appl. Phys. B*, 120 (2015) 223-232.
- [112] J. Vattulainen, L. Wallenius, J. Stenberg, R. Hernberg, V. Linna, Experimental Determination of SO₂, C₂H₂, and O₂ UV Absorption Cross Sections at Elevated Temperatures and Pressures, *Appl. Spectrosc.*, 51 (1997) 1311-1315.

-
- [113] G. Ben-Dor, O. Igra, T.E. Elperin, Handbook of Shock Waves, Academic Press, San Diego, 2001.
- [114] S. Zabeti, M. Fikri, C. Schulz, Reaction-time-resolved measurements of laser-induced fluorescence in a shock tube with a single laser pulse, Rev. Sci. Instrum., 88 (2017) 115105.
- [115] W. Demtröder, Laserspektroskopie: Grundlagen und Techniken, Springer, Berlin, Heidelberg, New York, 2007.
- [116] Thorlabs, Optics Selection Guide, Thorlabs, Inc., Newton, New Jersey, 2018, pp. 797-808.
- [117] E. de Hoffmann, V. Stroobant, Mass Spectrometry: Principles and Applications, John Wiley and Sons, Chichester, 2007.
- [118] LaVision, Product-Manual for High Speed IRO, LaVision, Inc., Goettingen, Germany, 2008.
- [119] LaVision, Product-Manual for DynaStar iXon, LaVision, Inc., Goettingen, Germany, 2008.
- [120] J.E.A. John, T.G. Keith, Gas Dynamics, Prentice Hall, Englewood Cliffs, NJ, 2006.
- [121] M. Aghsaee, Gas-phase kinetic study of soot precursors with variable hydrogen contents using a shock tube with high-repetition-rate time-of-flight mass spectrometry, PhD thesis, University of Duisburg-Essen, Duisburg, 2016.
- [122] E.d. Hoffmann, V. Stroobant, Mass spectrometry : principles and applications, 3rd ed., J. Wiley, Chichester, England ; Hoboken, NJ, 2007.
- [123] E. Stashenko, J. Ren, Gas Chromatography-Mass Spectrometry, Advances in Gas Chromatography 2014.
- [124] G.J. Williams, R.G. Wilkins, An investigation of the chemical structure of perchloric acid flames, Part I—The molecular beam sampling apparatus, Combust. Flame, 21 (1973) 325-337.
- [125] G.E. McMichael, J.B. French, Electron-Beam Studies of Skimmer Interaction in a Free Jet, Phys. Fluids, 9 (1966) 1419-1420.
- [126] D.J. Hucknall, A. Morris, Vacuum Technology Calculations in Chemistry, The Royal Society of Chemistry, Cambridge, UK, 2003.
- [127] W. Yuan, Y. Li, P. Dagaut, J. Yang, F. Qi, Investigation on the pyrolysis and oxidation of toluene over a wide range conditions. I. Flow reactor pyrolysis and jet stirred reactor oxidation, Combust. Flame, 162 (2014) 3-21.

- [128] W. Yuan, Y. Li, P. Dagaut, J. Yang, F. Qi, Investigation on the pyrolysis and oxidation of toluene over a wide range conditions. II. A comprehensive kinetic modeling study, *Combust. Flame*, 162 (2014) 22-40.
- [129] R. Sivaramakrishnan, R.S. Tranter, K. Brezinsky, High Pressure Pyrolysis of Toluene. 1. Experiments and Modeling of Toluene Decomposition, *J. Phys. Chem. A*, 110 (2006) 9388–9399.
- [130] C.S. Burton, W.A. Noyes, Electronic Energy Relaxation in Toluene Vapor, *J. Chem. Phys.*, 49 (1968) 1705-1714.
- [131] M. Fikri, M. Hartmann, C. Schulz, Temporally- and spectrally-resolved UV absorption measurements of toluene during pyrolysis in shock-heated gases, *European Combustion Meeting*, Cardiff, Great Britain, (2011).
- [132] N. Ikeda, N. Nakashima, K. Yoshihara, Formation and relaxation of hot benzyl radicals in the gas phase, *J. Phys. Chem.*, 88 (1984) 5803–5806.
- [133] W. Müller-Markgraf, J. Troe, Thermal decomposition of benzyl iodide and of benzyl radicals in shock waves, *J. Phys. Chem.*, 92 (1988) 4899–4905.
- [134] N.S. Smith, Y. Bénilan, P. Bruston, The temperature dependent absorption cross sections of C₄H₂ at mid ultraviolet wavelengths, *Planet. Space Sci.*, 46 (1998) 1215-1220.
- [135] Y. Bénilan, P. Bruston, F. Raulin, R. Courtin, J.C. Guillemin, Absolute absorption coefficient of C₆H₂ in the mid-UV range at low temperature; implications for the interpretation of Titan atmospheric spectra, *Planet. Space Sci.*, 43 (1995) 83-89.
- [136] B. Shukla, A. Susa, A. Miyoshi, M. Koshi, In Situ Direct Sampling Mass Spectrometric Study on Formation of Polycyclic Aromatic Hydrocarbons in Toluene Pyrolysis, *J. Phys. Chem. A*, 111 (2007) 8308-8324.
- [137] T.C. Zhang, L.D. Zhang, X. Hong, K.W. Zhang, F. Qi, C.K. Law, T.H. Ye, P.H. Zhao, Y.L. Chen, An experimental and theoretical study of toluene pyrolysis with tunable synchrotron VUV photoionization and molecular-beam mass spectrometry, *Combust. Flame*, 156 (2009) 2071-2083.
- [138] R.K. Abhinavam Kailasanathan, J. Thapa, F. Goulay, Kinetic Study of the OH Radical Reaction with Phenylacetylene, *J. Phys. Chem. A*, 118 (2014) 7732–7741.
- [139] T.J. Wallington, H. Egsgaard, O.J. Nielsen, J. Platz, J. Sehested, T. Stein, UV–visible spectrum of the phenyl radical and kinetics of its reaction with NO in the gas phase, *Chem. Phys. Lett.*, 290 (1998) 363–370.
- [140] A. Le Person, G. Eyglunent, V. Daële, A. Mellouki, Y. Mu, The near UV absorption cross-sections and the rate coefficients for the ozonolysis of a series of styrene-like compounds, *J. Photochem Photobiol. A: Chem.*, 195 (2008) 54–63.

- [141] E.O. Brigham, *The Fast Fourier Transform and Its Applications*, Prentice-Hall, Inc., Englewood Cliffs, NJ., 1988.
- [142] M. Sirignano, A. Collina, M. Commodo, P. Minutolo, A. D'Anna, Detection of aromatic hydrocarbons and incipient particles in an opposed-flow flame of ethylene by spectral and time-resolved laser induced emission spectroscopy, *Combust. Flame*, 159 (2012) 1663–1669.
- [143] D. Robaugh, W. Tsang, Thermal decomposition of phenyl iodide and o-iodotoluene, *J. Phys. Chem.*, 90 (1986) 5363 - 5367.
- [144] S.S. Kumaran, M.-C. Su, J.V. Michael, Thermal decomposition of iodobenzene using I-atom absorption, *Chem. Phys. Lett.*, 269 (1997) 99 –106.
- [145] J.C.G. Martín, J. Blahins, U. Gross, T. Ingham, A. Goddard, A.S. Mahajan, A. Ubelis, A. Saiz-Lopez, In situ detection of atomic and molecular iodine using Resonance and Off-Resonance Fluorescence by Lamp Excitation: ROFLEX, *Atmos. Meas. Tech.*, 4 (2011) 29-45.
- [146] L. Zhang, J. Cai, T. Zhang, F. Qi, Kinetic modeling study of toluene pyrolysis at low pressure, *Combust. Flame*, 157 (2010) 1686 –1697.
- [147] D. Ambrose, J.H. Ellender, C.H.S. Sprake, R. Townsend, Thermodynamic properties of organic oxygen compounds XLIII. Vapour pressures of some ethers, *J. Chem. Thermodyn.*, 8 (1976) 165-178.
- [148] S.E. Stein, Mass Spectra by NIST mass Spec data Center, in: *NIST Chemistry WebBook*, NIST Standard Reference Database Number 69, P.J. Linstrom, W.G. Mallard (Eds.), National Institute of Standards and Technology, Gaithersburg, MD, 2015.
- [149] E. Ranzi, A. Frassoldati, R. Grana, A. Cuoci, T. Faravelli, A.P. Kelley, C.K. Law, Hierarchical and comparative kinetic modeling of laminar flame speeds of hydrocarbon and oxygenated fuels, *Prog. Energy Combust. Sci.*, 38 (2012) 468-501.
- [150] M. Pecullan, K. Brezinsky, I. Glassman, Pyrolysis and Oxidation of Anisole near 1000 K, *J. Phys. Chem. A*, 101 (1997) 3305-3316.
- [151] J. Platz, O.J. Nielsen, T.J. Wallington, J.C. Ball, M.D. Hurley, A.M. Straccia, W.F. Schneider, J. Sehested, Atmospheric Chemistry of the Phenoxy Radical, C₆H₅O(•): UV Spectrum and Kinetics of Its Reaction with NO, NO₂, and O₂, *J. Phys. Chem. A*, 102 (1998) 7964-7974.
- [152] H. Grosch, Z. Sárossy, H. Egsgaard, A. Fateev, UV absorption cross-sections of phenol and naphthalene at temperatures up to 500 °C, *J. Quant. Spectrosc. Radiat. Transfer*, 156 (2015) 17-23.

- [153] T. Etzkorn, B. Klotz, S. Sørensen, I.V. Patroescu, I. Barnes, K.H. Becker, U. Platt, Gas-phase absorption cross sections of 24 monocyclic aromatic hydrocarbons in the UV and IR spectral ranges, *Atmos. Environ.*, 33 (1999) 525-540.
- [154] H.-H. Perkampus, *UV-VIS Atlas of Organic Compounds. 1. Spectra A1/1 - C9/13*, 2nd ed., Wiley-VCH, Weinheim [u.a.], 1992.
- [155] D.L. Pavia, G.M. Lampman, G.S. Kriz, J.R. Vyvyan, *Introduction to spectroscopy*, 4th ed. ed., Brooks/Cole, Belmont, CA, 2009.
- [156] N. Nijegorodov, R. Mabbs, D.P. Winkoun, Influence of weak and strong donor groups on the fluorescence parameters and the intersystem crossing rate constant, *Spectrochimica Acta Part A: Molecular and Biomolecular Spectroscopy*, 59 (2003) 595-606.
- [157] A. Bolovinos, J. Philis, E. Pantos, P. Tsekeris, G. Andritsopoulos, The Methylbenzenes Vis-a-Vis Benzene - Comparison of Their Spectra in the Valence-Shell Transitions Region, *J. Mol. Spectrosc.*, 94 (1982) 55-68.
- [158] S. Lange, K. Luther, T. Rech, A.M. Schmoltner, J. Troe, C-C and C-H Bond Splits of Laser-Excited Aromatic-Molecules .4. Specific Rate Constants and Branching Ratios for the Dissociation of the Xylenes, *J. Phys. Chem.*, 98 (1994) 6509-6513.
- [159] S.K. Pollack, B.C. Raine, W.J. Hehre, Determination of the heats of formation of the isomeric xylylenes by ion cyclotron double-resonance spectroscopy, *J. Am. Chem. Soc.*, 103 (1981) 6308-6313.
- [160] G. da Silva, E.E. Moore, J.W. Bozzelli, Decomposition of Methylbenzyl Radicals in the Pyrolysis and Oxidation of Xylenes, *J. Phys. Chem. A*, 113 (2009) 10264-10278.
- [161] U. Brand, H. Hippler, L. Lindemann, J. Troe, C-C and C-H Bond Splits of Laser-Excited Aromatic-Molecules .1. Specific and Thermally Averaged Rate Constants, *J. Phys. Chem.*, 94 (1990) 6305-6316.
- [162] C. Lee, Pressure and temperature dependence of recombination reactions of benzyl-type radicals, PhD thesis, Institute of Physical Chemistry, University of Göttingen, Göttingen, 2008.
- [163] H. Hippler, S. Seisel, J. Troe, Pyrolysis of p-xylene and of 4-methylbenzyl radicals, *Proc. Combust. Inst.*, 25 (1994) 875-882.
- [164] R.X. Fernandes, A. Gebert, H. Hippler, The pyrolysis of 2-, 3-, and 4-methylbenzyl radicals behind shock waves, *Proc. Combust. Inst.*, 29 (2002) 1337-1343.
- [165] C.H. Wu, H.J. Singh, R.D. Kern, Pyrolysis of acetylene behind reflected shock waves, *Int. J. Chem. Kinet.*, 19 (1987) 975-996.

- [166] M. Aghsaee, S.H. Durrstein, J. Herzler, H. Bohm, M. Fikri, C. Schulz, Influence of molecular hydrogen on acetylene pyrolysis: Experiment and modeling, *Combust. Flame*, 161 (2014) 2263-2269.
- [167] K. Norinaga, O. Deutschmann, N. Saegusa, J.-i. Hayashi, Analysis of pyrolysis products from light hydrocarbons and kinetic modeling for growth of polycyclic aromatic hydrocarbons with detailed chemistry, *J. Anal. Appl. Pyrolysis*, 86 (2009) 148-160.
- [168] A. Fahr, A.K. Nayak, Temperature dependent ultraviolet absorption cross sections of 1,3-butadiene and butadiyne, *J. Chem. Phys.*, 189 (1994) 725-731.
- [169] A. Fahr, Ultraviolet absorption spectrum and cross-sections of ethynyl (C₂H) radicals, *J. Mol. Spectrosc.*, 217 (2003) 249-254.
- [170] K.A. Bhaskaran, P. Roth, The shock tube as wave reactor for kinetic studies and material systems, *Prog. Energy Combust. Sci.*, 28 (2002) 151–192.
- [171] R.S. Tranter, B.R. Giri, A diaphragmless shock tube for high temperature kinetic studies, *Rev. Sci. Instrum.*, 79 (2008) 094103.
- [172] K. Fieweger, R. Blumenthal, G. Adomeit, Shock-tube investigations on the self-ignition of hydrocarbon-air mixtures at high pressures, *Proc. Combust. Inst.*, 25 (1994) 1579-1585.
- [173] M. Bozkurt, M. Fikri, C. Schulz, Investigation of the kinetics of OH* and CH* chemiluminescence in hydrocarbon oxidation behind reflected shock waves, *Appl. Phys. B*, 107 (2012) 515-527.
- [174] P. Fjodorow, M. Fikri, C. Schulz, O. Hellmig, V.M. Baev, Time-resolved detection of temperature, concentration, and pressure in a shock tube by intracavity absorption spectroscopy, *Appl. Phys. B*, 122 (2016) 159.
- [175] N. Jiang, W.R. Lempert, Ultrahigh-frame-rate nitric oxide planar laser-induced fluorescence imaging, *Opt. Lett.*, 33 (2008) 2236-2238.
- [176] J.B. Michael, P. Venkateswaran, J.D. Miller, M.N. Slipchenko, J.R. Gord, S. Roy, T.R. Meyer, 100 kHz thousand-frame burst-mode planar imaging in turbulent flames, *Opt. Lett.*, 39 (2014) 739-742.
- [177] S. Zabeti, M. Aghsaee, M. Fikri, O. Welz, C. Schulz, Optical properties and pyrolysis of shock-heated gas-phase anisole, *Proc. Combust. Inst.*, 36 (2017) 4525-4532.

